Optical properties of rare earth thin films

J. C. Krizek

OPTICAL PROPERTIES OF RARE EARTH THIN FILMS.

J. G. KRIZEK, Dipl.Phys., (Prague)

Presented in candidature for the degree of

DOCTOR OF PHILOSOPHY

October, 1973.

ABSTRACT

Measurements have been made of the complex refractive index of thin films of several of the rare earth elements in the photon energy range from 0.33 - 3.0eV, using a conventional ellipsometric method. The observations were carried out at various temperatures between 4.2 and 300°K, corresponding to the different magnetically ordered phases of the elements neodymium, gadolinium, terbium, dysprosium, holmium, erbium and ytterbium.

In the elements which show helical ordering, no evidence was found for absorption at the gaps corresponding to the superzone boundaries. Instead the results suggest that magnetic ordering of any type is seen in a general way through direct transitions between the exchange split levels of the band structure. The exchange energies estimated this way are in reasonable agreement with theoretical values. Suggested locations are given for the regions in k space corresponding to these "magnetic transitions". The Drude contribution to the optical conductivity has been obtained and the variation of $\sigma(w)_{w=0}$ for the different elements is in good agreement with static conductivity measurements although the magnitude of the optical constant is in general larger by about 15%. This is presumably due to the effects of the joint anisotropy of the electron relaxation times and velocities at the Fermi surface.

A C K N O W L E D G E M E N T S

I wish to express my gratitude to my supervisor, Dr. K.N.R. Taylor, for his guidance and encouragement. My appreciation goes to the entire Physics Department of Durham University, particularly to Professor G.D. Rochester, F.R.S., the Head of the Department, to the staffs of the workshops for their cooperation, and to my colleagues in the solid state group. Thanks are also due to Dr. W.D. Corner and Dr. A. Fort for their patience in checking the manuscript. I am indebted to Dr. J.N. Hodgson of the University of Keel for valuable discussions and his kindness in allowing me to see his data prior to publication. Finally, I would like to thank Mrs. J. Munro most sincerely for typing the script.

CONTENTS

CHAPTER I

INTRODUCTION

Even though the knowledge of the electronic structure is found to be particularly important for the understanding of most of the physical properties of the metals, relatively little experimental evidence which leads to the determination of the electronic structure of Rare Earth metals has been reported so far. The extreme reactiveness of these metals presents a great obstacle in producing single crystals of sufficient quality to be able to use de Haas van Alfvén effect, ultrasonic attenuation or similar powerful methods of Fermi surface determination. One of the methods of indirect determination of the band structure involves the investigation of the optical constants. Even though the complexity of the energy band structure of conduction electrons requires studies of single crystals some valuable information about the band structure can be achieved from the systematic investigation of the optical properties of the thin polycrystalline films. In spite of the success which optical studies have had in providing details of the electronic structure of metals, relatively few investigations have been made of the elements of the rare earth series and there has been little success in correlating optical constants with the details of the electronic band structure. Recent relativistic RAPW calculations have provided sufficient band detail to make closer examination of the optical constants justifiable.

This encouraged the present extensive study of the effects of the magnetic ordering on the optical constants of the rare earths with the aim of achieving a correlation with the calculated band structures.

CHAPTER II.

PHYSICAL PROPERTIES OF RARE EARTHS

A brief summary of the physical properties of rare earths is relevant in a report on the investigation of their band structure and optical properties. For a more detailed review the reader is referred to a monograph by Taylor and Darby (1972). Special attention is given to the effects of various magnetization processes on the band structure of rare earth metals (R.E.).

2.1 Electronic configuration

The members of the group IIIa of the periodic table (atomic Nos. 57 to 71) are collectively known as the 'rare earths'. The lanthanides, as they are alternatively called, have very similar chemical properties (see for instance Taylor and Darby). This is due to the essentially unchanged outer electron configurations through the series. A general representation of the electron configuration of the R.E. neutral atom is

$$((Xe)\ 4d^{10}4f^{n}5s^{2}5p^{6}5d^{(1)}6s)$$

where n increases from 0 to 14 from La (Z = 57) to Lu (Z = 71) and (Xe) denotes the Xenon core. Electrons $5d^{(1)}$ and 6s are regarded as outer electrons. These are removed to become conduction electrons in the metallic state leaving a trivalent ion core (with exception of Eu and Yb which are divalent as discussed below). The properties of the trivalent rare earths are related to those of transition metals because their outer electrons contain 5d-electrons. In Eu the configuration with half filled shell and two $6s^2$ electrons slightly below the 5d shell results in this element being divalent. The similar situation occurs in Yb, which has the 4f shell filled. Eu and Yb are exceptional among the rare earths also for their crystal structure. These properties place them among the alkaline earth

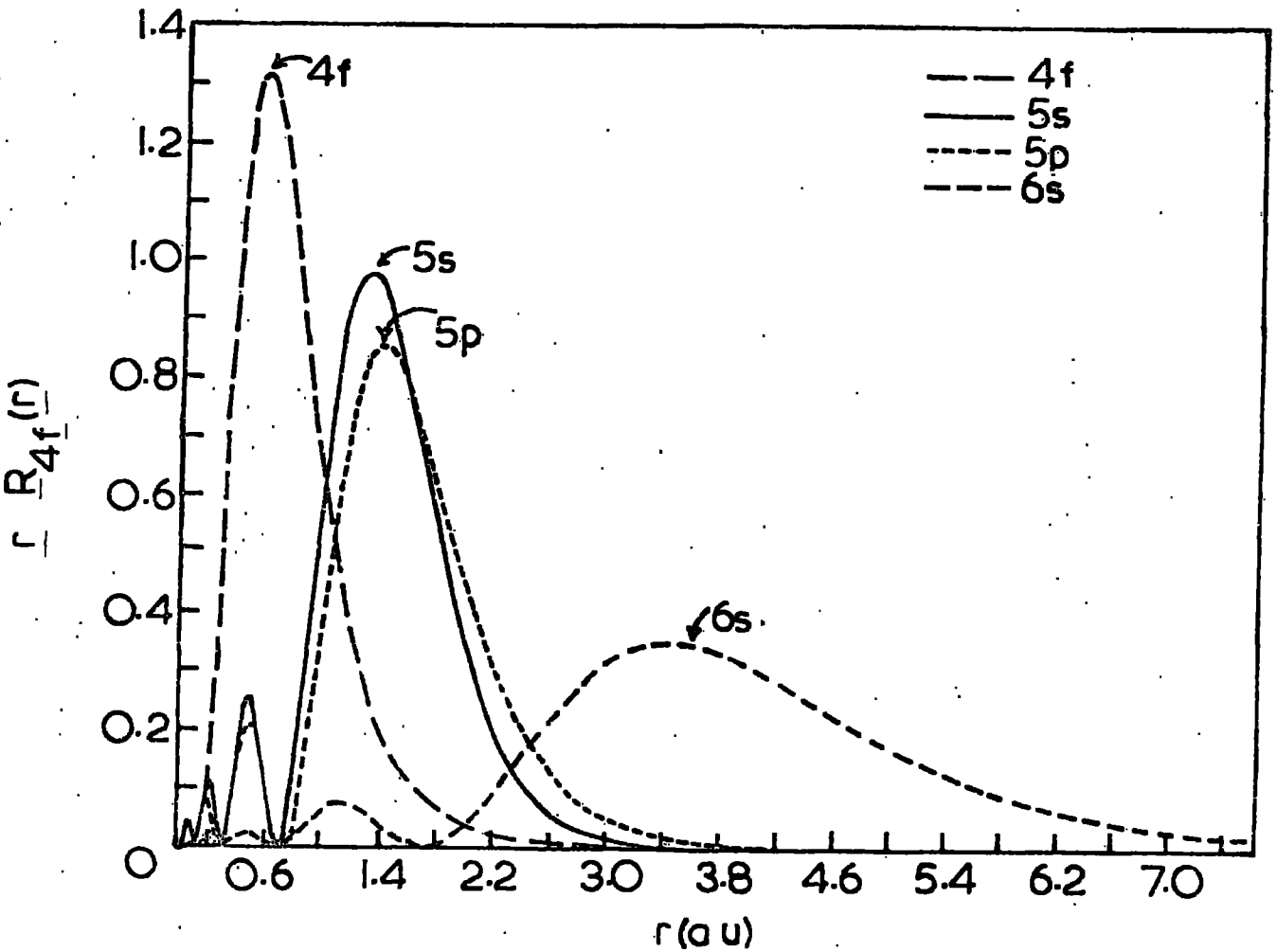

Fig.II.1 Hartree-Fock radial densities for the 4f,5s,5p and 6s electrons of Gd^{3+} (Freeman & Watson 1962)

metals. The 4f shell lies deep in the atom shielded by the 5s and 5p shells and is generally assumed to be tightly bound and localized as discussed below. Radial densities of the outer electrons may be seen in the Fig. II.1 illustrating that the 4f shell is well localised in the core.

2.2 Crystal structure of Rare Earths presently under investigation

In the temperature range presently under investigation (i.e. 10° - 300°K) Gd, Tb, Dy, Ho, Er crystallize in the hexagonal close packed structure while Nd is double hexagonal and Yb is face centred cubic.* There are therefore no structural transitions in the above range and this fact is used in the discussion of optical results (Section 6.1).

2.3 Magnetic ordering in Rare Earth metals

2.3.1 4f electrons

Uncompensated spin of the 4f electrons gives rise to a complex magnetic behaviour of rare earth metals. As is discussed below, this behaviour is related to the band structure of the conduction electrons and so influences many of the physical properties including optical properties. The magnetic properties are therefore discussed in some detail in this Chapter. It is generally believed that the 4f electrons in the rare earth metals except Yb, Eu and Ce are tightly bound in the ionic core. This is supported by the results of the measurements of $\langle r^{-3} \rangle$, where $\langle r \rangle$ is the average electron radius, from hyperfine fields and high temperature magnetic susceptibilities, both of which are similar to those of the ions.*

2.3.2. Magnetic structures

The magnetic structures of the 4f electrons below ordering temperatures have been investigated by the neutron diffraction technique (Koehler et al 1962, 1961, 1963). The complex nature of the magnetic structures is shown in the Fig. II.2. As may be seen from Fig. II.2 Gd is truly ferromagnetic over the whole temperature range but nevertheless

* Taylor & Darby (1972)

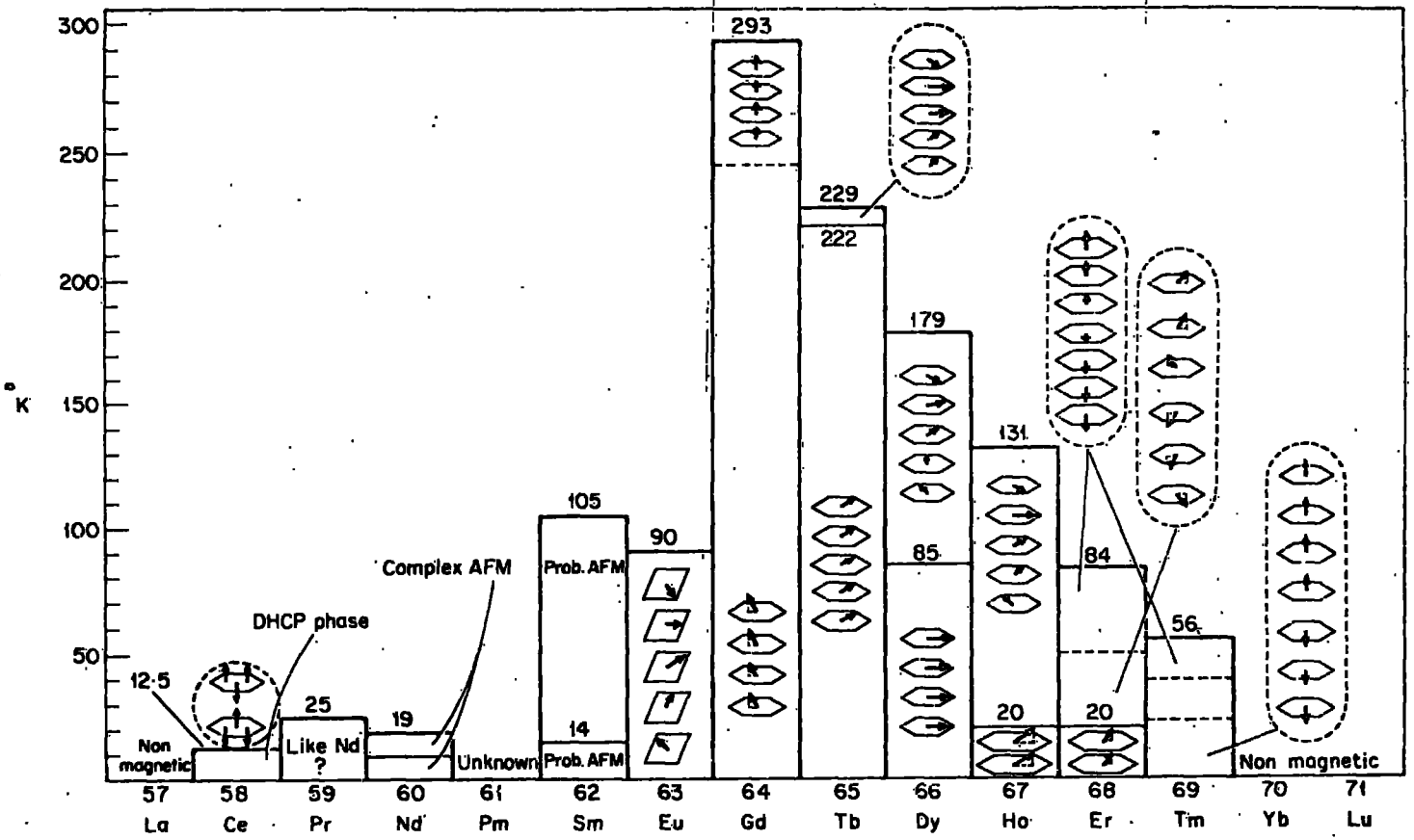

Fig.II.2 The observed magnetic structures of the Rare Earth metals in zero applied field (from Taylor & Darby (1972))

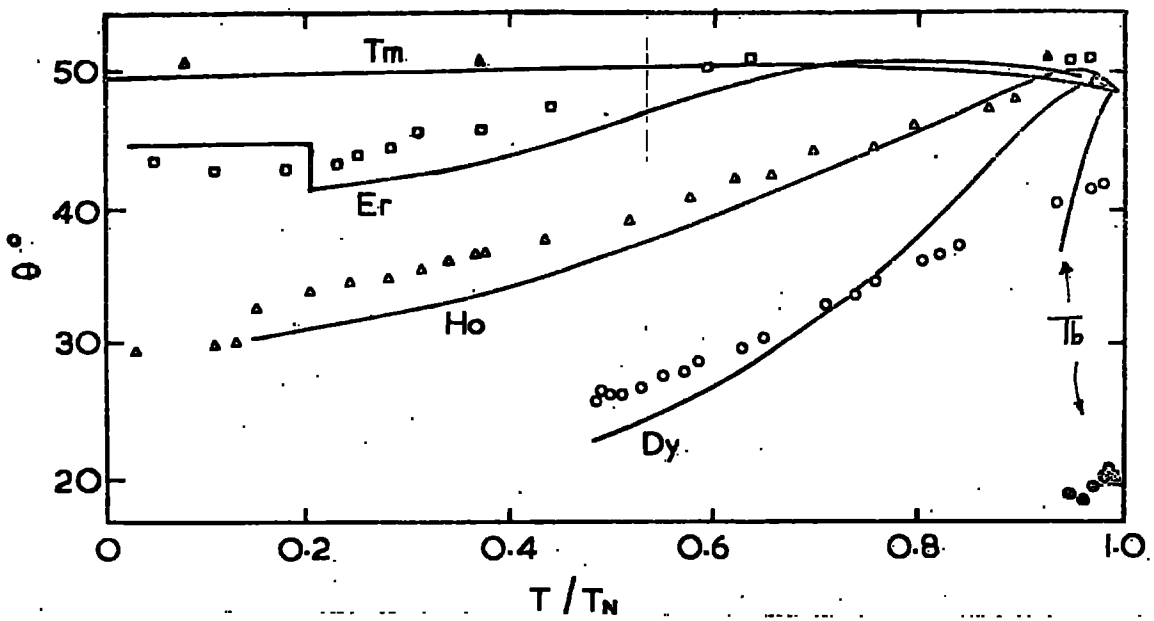

Fig.II.3 The interlayer turn angle $\theta = |Q| \cdot c$ (c is the lattice spacing along c-axis) as a function of reduced temperature T/T_N (from Elliot and Wedgewood (1964)). Experimantal points are shown by the various symbols (Koehler et.al. (1963)).

provides a variety of spin orientations. Tb, Dy and Ho show a helical spin arrangement in their antiferromagnetic region. The helical spin arrangement is given by an expression for the averages of the spin components.

$$\underline{\text{Helical}} \qquad \langle S_i^x \rangle = \langle S_\perp \rangle \cos(\vec{Q}\vec{R}_i + \varphi)$$

$$(\text{Tb,Dy,Ho}) \qquad \langle S_i^y \rangle = \langle S_\perp \rangle \sin(\vec{Q}\vec{R}_i + \varphi)$$

$$S_i^z = 0 \qquad \text{II.1}$$

$\langle S_\perp \rangle$ is an average ionic spin component in the basal plane, $\vec{R}_i$ is the radius vector of the i-th atom. The quantity $\vec{Q}$ defines the turn angle of the helix. As may be seen from Fig. II.3 the turn angle varies slightly with temperature; φ is called the phase of the helix. Er and Tm show another type of spin structure in the antiferromagnetic phase. It is given by the following expression for the spin components.

$$\underline{\text{Tm-type}} \qquad \langle S_i^y \rangle = \langle S_i^x \rangle = 0$$

$$(\text{Tm,Er}) \qquad \langle S_i^z \rangle = \langle S_\parallel \rangle \cos(\vec{Q}\vec{R}_i + \varphi) \qquad \text{II.2}$$

$\langle S_\parallel \rangle$ is an average ionic spin component in the hexagonal axis

In some cases the spin structures of the rare earths are combinations of the above two types. Magnetic field applied to a helical spin structure transforms it to a "fan structure" in which the magnetization vectors along the z-axis are oscillating functions of the distance and "oscillate" about the field direction. Further increase in the field strength above a critical value (H_c) produces a full collapse of a "fan structure" to the parallel spin alignment. The critical field is a function of temperature, generally rising from a low value just above the Curie temperature to a maximum of some 30 kOe just below the Néel temperature. As an example the critical field for Dy at temperature 90°K, i.e. 10°K above the Curie point (T_c), is approximately 1000 Oe. The antiferromagnetic ordering at temperatures slightly above the Curie point may therefore be readily trans-

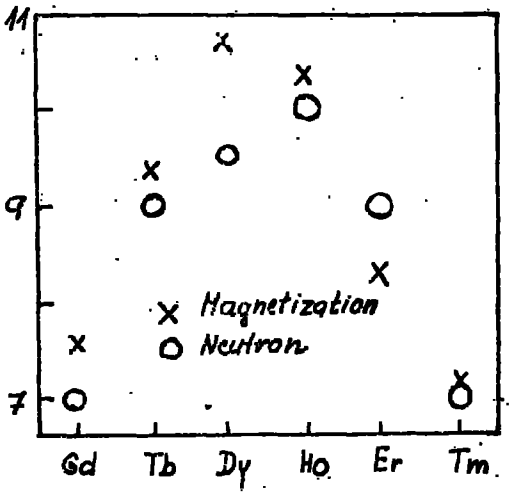

Fig.II.4 Comparison of the saturation moments of the heavy Rare Earth metals obtained from magnetisation and neutron diffraction data (from Taylor & Darby (1972)).

formed into ferromagnetic ordering. This fact is later on used for studies of optical properties in ferro- and antiferromagnetic phases and the study of the Kerr effect.

2.3.3. Magnetic ordering and conduction electron states

Magnetization curves combined with the neutron diffraction data may give useful information about the influence of magnetic ordering on the conduction electron states. The conduction electron polarization results in an additional contribution to the observed magnetization which is not measured during the neutron diffraction (Koehler et al 1962). From these types of experimental results shown in Fig. II.4 we can estimate the conduction electron polarization which is a measure of the reoccupation of conduction electron states due to magnetic ordering. As is shown below the mechanisms giving rise to this experimental fact are probably the most important for the discussion of the optical effect of magnetic ordering.

a) R-K-K-Y theory

In the Section 2.3.1 the localized nature of the 4f electrons was pointed out. It follows that there is a negligible overlap between 4f electrons on neighbouring ions and therefore no direct exchange interaction. However, rare earth metals show a great variety of magnetic ordering and magnetic order is possible up to 300°K. Rare Earth salts, on the other hand, are paramagnetic in the same temperature range although the lattice spacings between R.E. ions in salts are comparable with those in the metals (for a review see Taylor and Darby 1972).

In the theory, developed by Rudermann and Kittel (1954), Kasuya (1956) and Yosida (1957) and therefore frequently referred to as the R-K-K-Y theory, the magnetic ordering in R.E. metals occurs by means of an indirect exchange between the 4f-electrons of different atoms via conduction electrons, i.e. the indirect interaction between the localized spins is given by the

s-f exchange interaction given by the Hamiltonian (see the above references)

$$H_{s-f} = \frac{1}{N}\sum_{j} A(\vec{r} - \vec{R}_j)\, \vec{s} \cdot \vec{S}_j \qquad \text{II.3}$$

where S_j is the spin due to the localized 4f electrons on the site j given by the lattice vector $\vec{R}_j$; $\vec{s}$, $\vec{r}$ are the conduction electron spin and radius vector respectively, $A(\vec{r} - \vec{R}_j)$ is the exchange integral of the s-f exchange. The sum is over all lattice sites in the principal volume of the crystal. The Hamiltonian leads to an indirect interaction between localized spins:

$$H = -\sum_{i,j} I(\vec{R}_j - \vec{R}_i)\, \vec{S}_j\, \vec{S}_i \qquad \text{II.4}$$

$I(\vec{R}_i - \vec{R}_j)$ is the exchange integral of the indirect exchange between the localized ions. The Fourier transforms of the above exchange integrals A and I have the following relation:

$$I(\vec{q}) = 4/N \left|A(\vec{q})\right|^2 \chi(\vec{q}) \qquad \text{II.5}$$

where N is a number of atoms (in the sum II.3) in the principal volume of the crystal and $\chi(\vec{q})$ is the generalized susceptibility. Taylor and Darby (1972 Section 4.1) defined $\chi(\vec{q})$ by the expression

$$\chi(\vec{q}) = 1/N \sum_{\vec{k},n,n} \frac{f(\mathcal{E}_n(\vec{k})) - f(\mathcal{E}_n(\vec{k}+\vec{q}))}{\mathcal{E}_n(\vec{k}) - \mathcal{E}_n(\vec{k}+\vec{q})} \qquad \text{II.6}$$

where $f(\mathcal{E}_n(\vec{k}))$ is a Fermi-Dirac distribution function corresponding to the energy eigenvalue $\mathcal{E}_n(\vec{k})$ of the conduction electrons, n is the band index, $\vec{k}$ is the electron wavevector, N is the number of atoms per unit volume. The sum is over all conduction electron states $|n,\vec{k}\rangle$, $|n, \vec{k}+\vec{q}\rangle$. In the antiferromagnetic phase the wavevector $\vec{Q}$ of the periodic magnetically ordered structure, i.e. the "turn angle" wavevector defined by either of the equations II,1 or II.2, corresponds to the maximum of the Fourier

transform $I(\vec{q})$ of the exchange integral $I(R_j - R_i)$ (Coqblin 1971). According to the equation II.5 this maximum corresponds to those $\vec{q}$ for which $\mathcal{E}_n(\vec{k}) = \mathcal{E}_n(\vec{k}+\vec{q})$, i.e. if $\vec{q}$ connects two points of the Fermi surface (as discussed by Evenson and Liu 1968). It was found by Loucks (1968) that relativistic Fermi surfaces (see Section 2.4 below) of Rare Earth metals have large flat portions of the Fermi surface with "webbing features" for which the above condition may be satisfied. Also the corresponding value of $\vec{q}$ is comparable with $\vec{Q}$ measured experimentally. It is therefore apparent that conduction electrons play an important role in the stabilization of the antiferromagnetic ordering and gives an indirect support to the relativistic band structure calculations (discussed in Section 2.4) which are used for the interpretation of the present results in Chapter VI.

b) Splitting of conduction electron levels due to ferromagnetic ordering in Rare Earths

In the case of the motion of a Bloch electron in a ferromagnetic metal the Bloch equation (A(4) in Appendix A) would contain an additional perturbation term

$$\frac{1}{N}\sum_j A(\vec{r}-\vec{R}_j)\ \vec{s}\cdot\vec{S}_j$$

for magnetic exchange which is given by equation II.3. Suppose that ferromagnetic ordering occurs along the z-axis then the Bloch equation is given by

$$\left[-\frac{\hbar^2\nabla^2}{2m} + V(\vec{r}) - \frac{\hbar^2}{4m^2c^2}\left(\vec{\nabla}V(\vec{r})\vec{\nabla} - (\vec{\nabla}V(\vec{r})\times\vec{p})\vec{\sigma}\right) - \frac{1}{N}\sum_j A(\vec{r}-\vec{R}_j)\,\sigma_z\cdot S^z\right]\psi^s_{n\vec{k}}$$
$$= \mathcal{E}_n(\vec{k},s)\,\psi^s_{n\vec{k}} \qquad \text{II.7}$$

where s is the spin index ($s = \pm\frac{1}{2}$), $\vec{\sigma} = (\sigma_x, \sigma_y, \sigma_z)$, σ are Pauli matrices. The sum over j in the last term is over N lattice sites of the principal volume of the crystal. The exchange term in II.7 is assumed to

be isotropic (Taylor and Darby, 1972) and has a translation symmetry of the lattice. Therefore the translational symmetry of the wave function $\psi^{s}_{n\vec{k}}$ as a solution of equation II.7 is identical to that of those given by equation A4 for a non-magnetic metal. However, the rotational symmetry of the s-f exchange is different from the symmetry of the lattice.

Consequently, levels $\mathcal{E}_n(\vec{k})$ will be spin split by H_{s-f} interaction into two levels $\mathcal{E}_n(\vec{k}, s = +\frac{1}{2})$ and $\mathcal{E}_n(\vec{k}, s = -\frac{1}{2})$ as may be seen from the first order perturbation theory. The energy gap will be [Watson et al. (1968)]

$$\Delta_{ferro} = S^z A(\vec{k},\vec{k}) \qquad \text{II.8}$$

where S^z is the ionic spin moment and $A(\vec{k},\vec{k})$ are diagonal matrix elements of the H_{s-f} exchange interaction corresponding to wavevector $\vec{k}$. Matrix elements $A(\vec{k},\vec{k})$ are usually supposed to be functions of the difference $\vec{k}-\vec{k}'$ from which we get ($A(\vec{k},\vec{k})$ = constant = $A(0)$) rigid exchange splitting of conduction bands over the whole Brillouin zone. In addition Δ_{ferro} was derived from the perturbation theory at zero temperature, $T = 0^{o}K$. For finite temperature the above equation will contain a temperature dependent factor $M(T)$ which is proportional to the saturation magnetization of the ferromagnetic metal (Watson et al 1968)

$$\Delta_{ferro} = S^z M(T) A(0) \qquad \text{II.9}$$

Ferromagnetic exchange splitting of conduction bands in rare earth metals is therefore directly proportional to the magnetization. Exchange integral $A(0)$ appears to be approximately constant through the sequence of heavy rare earths and their band structures appear to be very similar, (as follows from the energy band calculations made by Watson et. al. (1968), Keaton and Loucks (1968)).

c) Antiferromagnetic phase - superzone boundaries

Band gaps arise instead of the rigid splitting if the local spin moments order in either of the spirals of the antiferromagnetic order in heavy rare earths shown in Fig.II.2. Inserting either of the spiral structures into the equation II.3 yields off-diagonal s-f exchange perturbation elements between the Bloch states for the electron wavevectors $\vec{k} - \vec{k}' = \pm \vec{Q} + \vec{\tau}$ being the reciprocal lattice vector and $\vec{Q}$ being given by equation II.1 or II.2. These matrix elements arise between the states of like spin for the Tm spiral and between states $|n,\vec{k}\rangle$ of spin down and $|\vec{k} + \vec{Q} + \vec{\tau}\rangle$ of spin up for the helical Ho type of structure. Band gaps occur when $\vec{Q} + \vec{\tau}$ connects a degenerate pair of the band states. These gaps are, (Miwa 1963):

$$\Delta_{Tm} = MS\, A(\vec{Q} + \vec{\tau}) \quad |F(\vec{\tau})| \qquad \text{II.10}$$

$$\Delta_{Ho} = 2M'S\, A(\vec{Q} + \vec{\tau}) \quad |F(\vec{\tau})| \qquad \text{II.11}$$

where $F(\vec{\tau})$ is the structure factor $F(\vec{\tau}) = 1/n \cdot \sum_{j=1}^{n} \exp(i\vec{R}_j \cdot \vec{\tau})$ summed over the atomic sites in a unit cell. Elliot et al (1963, 1964) have shown that these gaps are important in determining many physical properties, particularly the turn angle and electrical resistivity. Watson et. al, have estimated the sizes of these band gaps using results of non-relativistic APW band calculations. (Watson et al 1968). Results have been obtained by perturbation of the nonmagnetic bands with a spiral of the Tm structure and assuming the $A(Q) \approx A(0)$ for the ferromagnetic Gd. Results are shown in the following Table II.1.

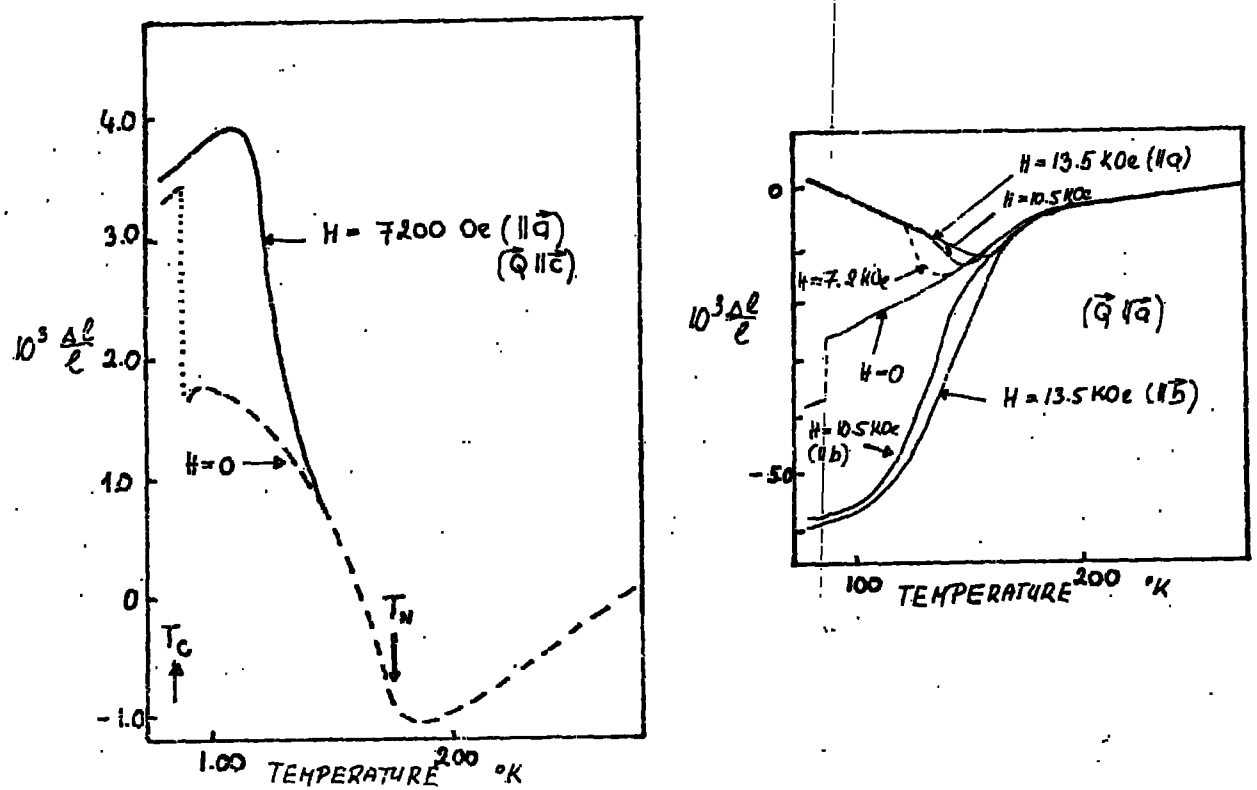

Fig.II.5. Magnetostrictive strains in dysprosium along a- and c-axes for the applied fields shown(Clark et.al. (1965)). $\vec{Q}$-direction of the strain gauge

TABLE II.1.

Estimates of the values of Δ for the heavy rare earth metals (Δ is exchange splitting due to magnetic ordering)

Element	Δ_{ferro} (eV)	$\Delta_{antiferro}$ (eV)	Spin number
Gd	0.61	-	7/2
Tb	0.52	-	3
Dy	0.44	0.44	5/2
Ho	0.35	0.35	2
Er	0.26	-	3/2
Tm	0.17	-	1

From the above it is clear that both types of magnetic ordering are likely to contribute to the optical effects of magnetic ordering producing anomalies at approximately the same photon energy, but not necessarily in the same shape. That means that if there occurs an effect of superzone boundaries in the antiferromagnetic phase it should be generally recognisable from that of the exchange band splitting at the transition temperature between the helical and the ferromagnetic ordering.

2.3.4 Effect of magnetostriction

Magnetoelastic coupling is another factor which may influence the band structure of conduction electrons.

Magnetostriction has been found to be substantial in the rare earth metals particularly in the heavy ones (Clark et al 1965). As an illustration we quote Fig. II 5 where the magnetostriction of Dy is presented. It may be seen that the magnetostrictive strains in the ferromagnetic phase of Dy correspond to changes in the lattice constants by as much as 0.4% and are increasing as the temperature decreases. The corresponding values for other Rare Earth metals are similarly high. The large values

of magnetostriction below the Curie point suggest that the magnetoelastic energy is very large and plays an important role in the stabilization of the ferromagnetic order in the rare earth metals. The above was suggested by Cooper (1969) and supported by the spin wave spectra obtained by Møller et al (1968).

From Fig.II. 5 it may also be seen that during the transition from the antiferromagnetic to the ferromagnetic phase of Dy the lattice constant c increases by approximately 0.1% and the constants b, a decrease by 0.2%; the corresponding increase in c/a ratio is therefore 0.3%. These changes in the lattice spacing may induce changes in the one electron effective potential of conduction electrons which in turn produces shifts in the energy levels in the conduction band. This may lead to the reoccupation of some levels near to the Fermi energy (E_F). It is not likely that a new splitting of the levels due to magnetostriction will occur since there is a very little difference between b and a-axis magnetostriction and the hexagonal structure of the lattice is therefore conserved during the process of magnetization. The reoccupation of the energy levels near to E_F may be investigated by optical studies.

According to the above analysis the most remarkable changes in optical constants are expected to occur on cooling below the transition temperature between the antiferro and ferromagnetic phase where the lattice constant ratio c/a suddenly changes by 0.3%. However, as may be seen in Section 3.3.5 a) and results in Chapter V Section 5.4 the optical effect of magnetic ordering does not appear to depend on the specific type of the magnetic order. This may therefore suggest that the reoccupation of the levels due to the magnetostriction is not large enough to cause directly an optical effect. However, it is not possible to make any conclusions in this matter until the band structure of rare earths for various lattice constants is

calculated and further experimental evidence, especially from single crystals, is available.

2.3.5 Concluding remarks on magnetic ordering

From analysis in Sections 2.3.3 b) and c) it is evident that the band structure of a rare earth metal in an ordered phase can be deduced from the band structure of the paramagnetic R.E. metal using the ordinary perturbation theory in which the perturbation Hamiltonian is given by the equation II.3. The following section will therefore be devoted to the results of the recent investigations of the band structures of R.E. metals in the paramagnetic phase.

2.4. Band structure of conduction electrons of trivalent R.E. metals

As discussed above in Section 2.1 the conduction electrons of trivalent R.E. metals are formed from $5d^1$ and $6s^2$ atomic shells. Because of strong mixing of s- and d- states that form a conduction band the calculated band structure of R.E. metals differs markedly from that of the free electron model. Instead it closely resembles those of the transition metals (Dimmock, Freeman 1964) the bands of which correspond to almost "tightly bound" electrons. In the calculation of the Bloch functions which represent conduction electron states care must be taken to choose an adequate method, i.e. the expansion over a set of functions which give the most rapid convergence. From the above it is clear that plane wave expansion is not the most adequate alternative.

It is generally believed that band structures of R.E. metals are best calculated by means of the augmented plane waves (APW) (see Loucks 1965). In this model electrons are assumed to be tightly bound to the atomic core within the sphere with its centre in the atomic nucleus and the radius comparable to the atomic radius or the interatomic distance. Outside the sphere electrons are assumed to be free. Inside the so called Slater

sphere the electron wave functions are expressed in terms of an expansion of the atomic orbitals; outside the sphere the functions are plane waves. This model expresses the mixed s- and d- character of the conduction electron states. In general there are two approaches in which augmented plane waves are presented. One is based on the non-relativistic approach, i.e. both atomic orbitals and plane waves in the above expansion are solutions of the Schrodinger equation. In order to include relativistic effects, namely the spin orbit interaction, the functions in the expansion are solutions of the Dirac equation. The method is then called Relativistic Augmented Plane Waves (RAPW) method. The model potential inside the Slater sphere, the muffin-tin potential, is a sum of the potential of the nucleus, the Coulomb repulsive potential from both the electrons within the sphere and neighbouring atoms and the exchange potential energy from electrons within the sphere and neighbouring spheres. This complicated structure is discussed in detail by Loucks (1965) (also computing programmes are included). In most cases the calculated bands strongly depend on the chosen model potential. The band structure calculation is not therefore self consistent and needs comparison with experimental data. Most of the experimental data comes from optical investigations, measurements of density of states and Fermi surface studies.

The non-relativistic APW band structure calculations have been made for Gd (Dimmock and Freeman 1964), Y(Loucks 1966), Tm (Watson et al 1968) and Ho (Williams et al 1966). The results show very similar features for all the heavy elements. For most of the Rare Earths the spin-orbit interaction is important and therefore reliable band structures can be obtained only be means of relativistic (RAPW) band structure calculations. These were reported by Keeton and Loucks (1968, 1966) for Gd, Dy, Er and Lu. A calculation for Tb has been reported by Jackson (1969).

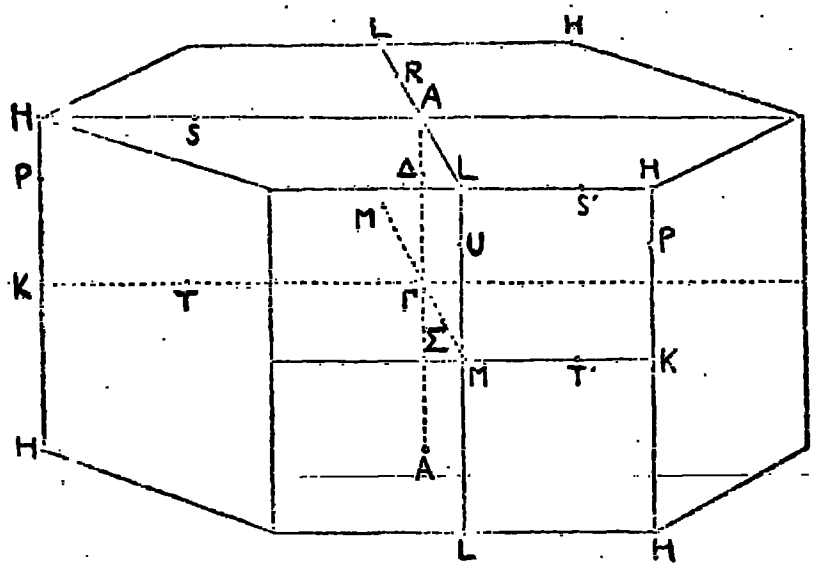

Fig.II.6 Brillouin zone of hexagonal close packed metals (from Herring(1942)).showing symmetry points and axes.

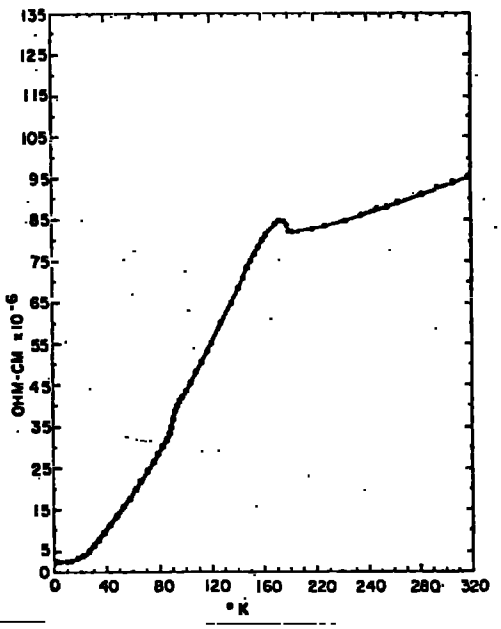

Fig.II.7. Electrical resistivity of polycrystalline dysprosium vs. temperature (Colvin et.al. (1960)).

The muffin-tin potential inside the Slater sphere was constructed from the charge densities which were themselves obtained by the relativistic self-consistent-field calculations. Exchange was included using the Slater's $\frac{1}{3}$ approximation (Loucks 1965). This is believed to be quite a reasonable approach to the calculation of electronic structures of metals. The two cases of the atomic configurations, for instance the configurations $\begin{bmatrix} 4f^9\ 5d^1\ 6s^2 \\ 4f^{10}\ \ \ 6s^2 \end{bmatrix}$, were examined in order to investigate how sensitive the results were to the potential. The results show quite a strong dependence of the energy band detail on the chosen potential. However, the overall features of the energy band structure remain independent of the chosen potential. Fig. II.8 shows results of non-relativistic APW calculations for Cd. Fig. II.9 shows relativistic (RAPW) energy bands of Tb calculated by Jackson (1969). The corresponding Brillouin zone is shown in the Fig. II.6. The reader who is not familiar with the symmetry notations of the irreducible representations at the symmetry points is referred to the Appendix A and a number of textbooks such as Callaway (1964), Kittel (1963), Cornwell (1969) and others.

As may be seen from the comparison the main difference of RAPW bands from those of APW is at the symmetry point L where a large nesting occurs above the Fermi level E_F for RAPW calculations and the band is therefore empty while the corresponding APW band occurs far below E_F and is therefore occupied. Also some of the levels at the symmetry points K and H are split due to the relativistic effects. However, the overall features of the two band structures are quite similar. Also calculated band structures for the different heavy rare earth metals have been found very similar and therefore the above band structures may be regarded as common to all heavy rare earth metals presently under investigation (i.e. Gd, Tb, Dy, Ho, Er) (Keeton & Loucks (1968), Watson et.al. (1968)).

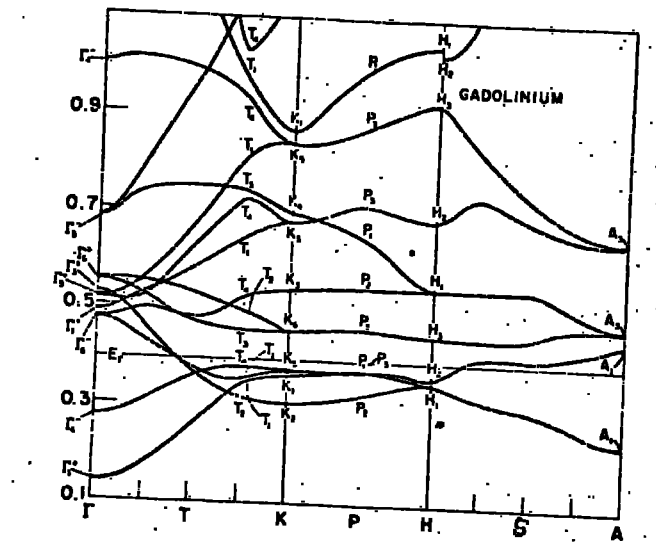

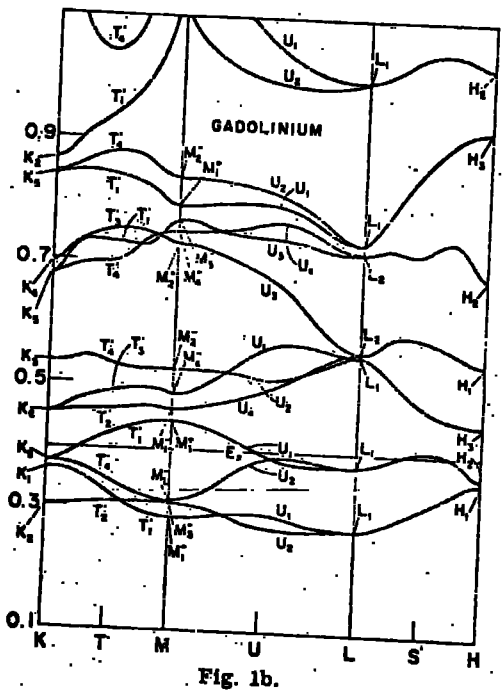

Fig. 1b.

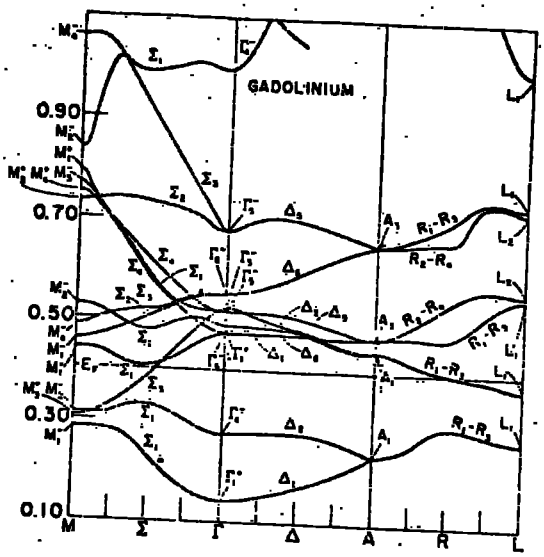

Fig.II.8. Non-relativistic energy bands of Gd (from Dimmock et al. (1965)). Ordinates are energies in Rydbergs.

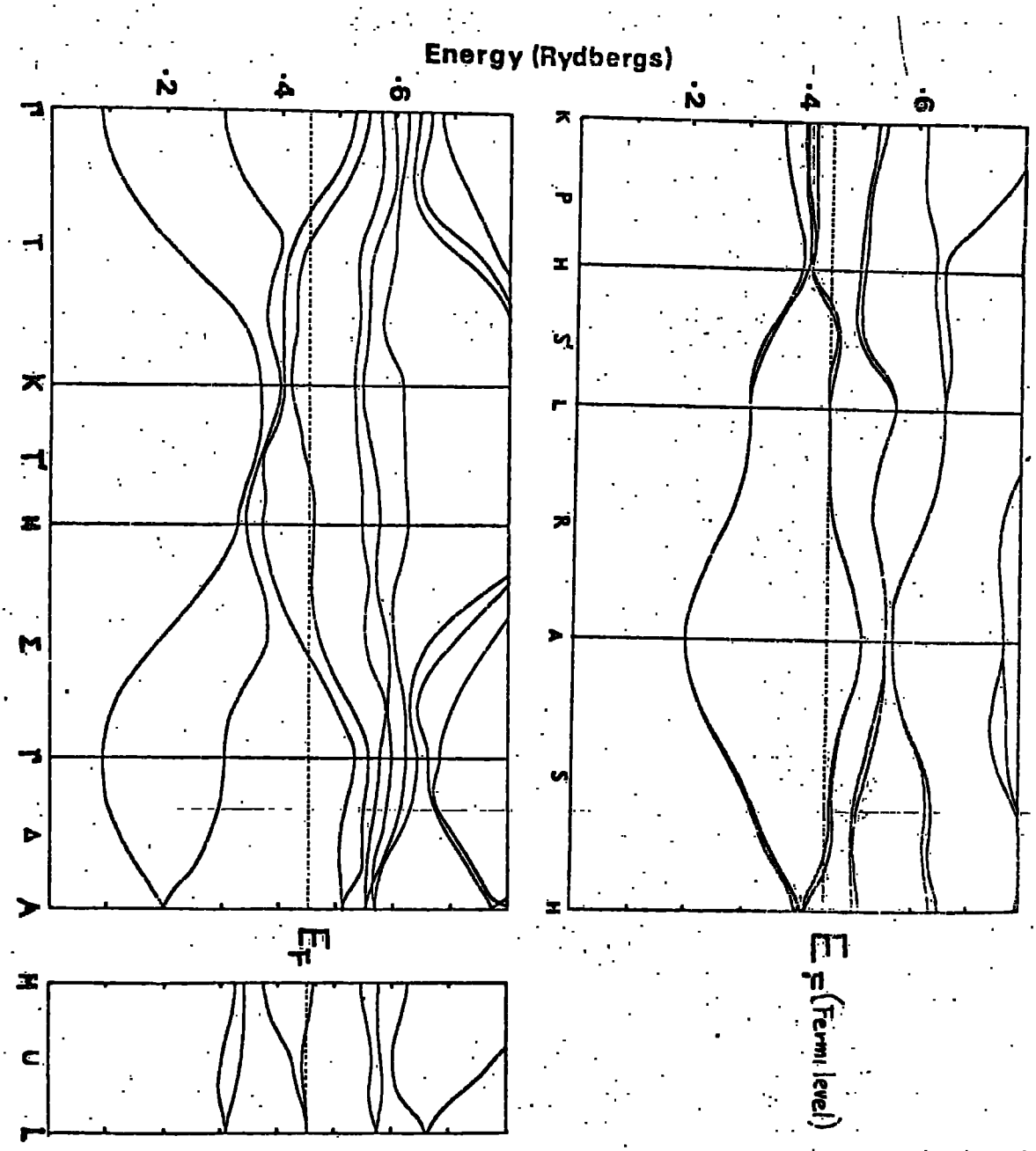

Fig.II.9 Energy bands of terbium metal (relativistic effects included).(after Jackson(1969)).

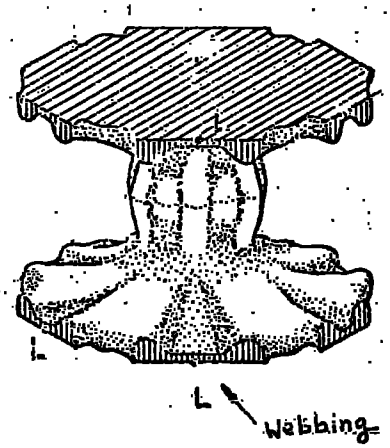

Fig.II.10

Fermi surface of terbium(Jackson(1969)).

The band nesting near to the point L corresponds to the flat portions of the Fermi surface, the so called "webbing features", which are thought to have a significant value in the stabilization of the antiferromagnetic order in heavy rare earths. The Fermi surface of a heavy rare earth metal is shown in the Fig. II.10.

2.5. Transport Properties

The theory of magnetic splitting of conduction electron states (Section 2.3.3) predicts anomalies in the resistivity variation with temperature (Elliot and Wedgwood 1964) which provides a link between optical properties and electronic properties of rare earth metals.

Such anomalies have been observed for a number of elements (Lodge 1969). A typical example of the resistivity of a polycrystalline rare earth metal is given in Fig. II.7.

The close relation between optical, electrical and magnetic properties of rare earth metals can be used for both the interpretations of the results and, in our case, served as a useful check of the quality of measured samples (see Results).

2.6 Conclusion

In the Section 2.3.3 it was pointed out that magnetic ordering produces a splitting of conduction bands. Such splitting causes reoccupation of the levels near to the Fermi energy and new optical transitions associated with it. Three mechanisms which are most likely to cause such splitting have been considered. These are ferromagnetic exchange splitting, energy gaps at the superzone boundaries and magnetostriction. It was also pointed out that the exchange factor $A(\vec{r} - \vec{R}_i)$ defined by the equation II.3 is approximately constant throughout the series of heavy rare earths. Also calculated energy bands are very similar throughout the series.

It may be seen from the following Chapter that exchange splitting may

be studied by means of optical investigations. From similarity of energy bands in rare earths and the fact that exchange constant A(0) is approximately constant throughout the series we can make a study of the common energy band model by systematic investigations of "magnetic" optical absorption bands of the rare earth metals.

The other important fact is that for such studies we can use, as a first approximation, results of band structure calculations for non-magnetic rare earth metals. With this in mind, we have studied the effects of magnetic ordering on the optical constants of the rare earths to investigate the degree of correlation with the calculated band structure. The results of this investigation are described in the following Chapters.

CHAPTER III.

OPTICAL PROPERTIES OF RARE EARTH METALS.

3.1 Introduction

It was pointed out in the previous chapter that magnetization processes produce changes in the band structure of Rare Earth metals. These changes may be investigated by optical studies as described below. This chapter deals with the microscopic theory of optical properties of R.E. metals and gives a comparison with recently published experimental results. A brief macroscopic definition of optical constants is presented in Appendix D.

The optical properties of R.E. metals are discussed in this chapter in terms of the behaviour of the real part of the optical conductivity $\sigma(\omega)$ as a function of the angular frequency ω of the radiation. The real part of the optical conductivity is briefly referred to as the "optical conductivity".

Since most of the R.E. metals under investigation have the hexagonal close packed crystal structure (Section 2.2) their optical constants are expected to be anisotropic and, strictly speaking, the above defined $\sigma(\omega)$ should be always presented in the tensor form.

However, thin polycrystalline films under investigation have, from the macroscopic point of view, no preferred lattice orientation (Hodgson and Cleyet (1969), Lodge (1969)). Hence, their apparent optical conductivity is an average over all lattice directions.

From the microscopic point of view the grains of the polycrystal are single crystals with anisotropic electronic structure. Therefore, in order to interpret, microscopically, the measured optical conductivity, the anisotropy of the band structure and optical conductivity has to be considered bearing in mind that the resulting optical conductivity is an average over all lattice directions.

The formal connection of optical properties with band structure presented in section 3.2 is made through the tensor form of the optical conductivity; the 3 x 3 components of the tensor are denoted as $\sigma_{ij} (i,j = 1,2,3)$.

On the other hand, the theory of free electron absorption (section 3.3) uses isotropic values of σ. The theory is mainly used to derive some empirical parameters from isotropic values of optical constants needed in the discussion of experimental results.

3.2 Direct Interband Optical Transitions

This section deals with electron transitions between the conduction bands in a solid caused by interaction with electromagnetic waves. The interaction Hamiltonian is given by Callaway (1964).

$$\hat{H}_{rad} = \frac{e}{mc} \vec{A} \cdot \vec{p} = \frac{e\hbar}{imc} \vec{A} \cdot \vec{\nabla} \qquad \text{III 1}$$

where e,m are electron charge and mass, c is the velocity of light, $\hbar$ is Plank's constant, $\vec{A}$ is the vector potential of the electromagnetic field and $\vec{p}$ is the momentum operator of an electron. The scalar potential can be assumed to be zero for the field of an electromagnetic wave, so the electric field $\vec{E}$ is given by the time derivative of the vector potential, i.e.

$$\vec{E} = -\frac{1}{c} \frac{\partial \vec{A}}{\partial t}$$

The real vector potential of a travelling wave of the frequency ω and wavevector $\vec{k}_{rad}$ will be represented by

$$\vec{A}(\vec{r},t) = A_o \vec{\alpha} \exp\left(i(\vec{k}_{rad} \cdot \vec{r} - \omega t)\right) + \text{complex conjugate} \qquad \text{III 2}$$

$\vec{\alpha}$ is the unit vector of the polarisation in the direction of the electric field. The transition probability between an occupied state $|i\rangle$ and an empty state $|j\rangle$ due to the absorption of one radiation quantum $\hbar\omega$ is given by Callaway (1964) as,

$$W_{ij} = \frac{2\pi}{\hbar} \left| \langle j | eA_o \vec{\alpha} \cdot \vec{p}/2mc \exp(i \vec{k}_{rad} \cdot \vec{r}) | i \rangle \right|^2 \delta(\varepsilon_j - \varepsilon_i - \hbar\omega) \qquad \text{III 3}$$

$\varepsilon_j, \varepsilon_i$ are corresponding energy levels; the δ-function indicates the conservation of energy during the transition $|i\rangle \rightarrow |j\rangle$. The rest of the symbols are defined above.

The rate of absorption of unit intensity electromagnetic radiation

per unit time and volume is given by real part of the tensor of optical conductivity (see also Appendix D).

Summing over all transitions $|i\rangle \rightarrow |j\rangle$ corresponding to a single frequency ω, taking the occupation number of electronic states $|i\rangle$ as ϱ_i into consideration, the real part the tensor of optical conductivity $\sigma_{\ell\ell}$ along a principal axis, say ℓ., is given by (Kohn 1965)

$$\sigma'_{\ell\ell}(\omega) = \frac{\pi}{\omega} \sum_{i,j} |\langle j | \Pi_\ell | i \rangle|^2 (\varrho_i - \varrho_j) \delta(\varepsilon_j - \varepsilon_i - \hbar\omega) \qquad \text{III 4}$$

where Π_ℓ is the component of $\hat{H}_{rad}$ for the polarisation along the coordinate axis indexed by ℓ, i.e.

$$\Pi_\ell = (e/2mc) \alpha_\ell \, p_\ell \, \exp(i\vec{k}_{rad} \cdot \vec{r}) \quad .$$

Since $\hat{H}_{rad}$ does not depend on spin, the optical transition matrix element in equation III 3 is zero if the states $|i\rangle$ and $|j\rangle$ correspond to different spin. The spin flip optical transitions are therefore not generally allowed.

If $|i\rangle, |j\rangle$ in equation III 3 are Bloch states $|n,\vec{k}\rangle = e^{i\vec{k}\cdot\vec{r}} u_n(\vec{k},\vec{r})$ $|n'\vec{k}'\rangle = e^{i\vec{k}'\cdot\vec{r}} u_{n'}(\vec{k}',\vec{r})$ respectively (n,n' are band indices, $\vec{k},\vec{k}'$ are conduction electron wavevectors), then the matrix element in III 3 can take the form

$$\langle n'k' | \hat{H}_{rad} | nk \rangle = \int d^3r \, u_{n'}(\vec{k}',\vec{r}) \, \hat{H}_{rad} \, u_n(\vec{k},\vec{r}) \cdot \delta(\vec{k}' - \vec{k} - \vec{k}_{rad}) \qquad \text{III 5}$$

The δ-function indicates the conservation law of the wavevectors, i.e.

$$\vec{k}' = \vec{k} + \vec{k}_{rad} \qquad \text{III 6}$$

In the optical region the radiation wavevector $\vec{k}_{rad}$ has an absolute value $|\vec{k}_{rad}|$ less than 10^6 cm^{-1} while maximum absolute value of the electron wavevector $\vec{k}$ is about 10^8 cm^{-1} (Callaway 1964). The selection rule III 6 corresponds to approximately vertical transitions between bands n and n', i.e.

direct transitions.

For Bloch electrons the expression III 4 takes the form (Kohn 1965)

$$\sigma^{1}_{ll}(\omega) = \frac{\pi e^2 \hbar^2}{m^2 \omega} \sum_{n n'} \int ds \frac{|\langle n,\vec{k}|(\vec{p}.\vec{\alpha})_l|n',\vec{k}\rangle|^2 [f_n(\vec{k}) - f_{n'}(\vec{k})]}{|\nabla_k [\varepsilon_n(\vec{k}) - \varepsilon_{n'}(\vec{k})]|} \qquad \text{III } 7$$

in which the occupation numbers ρ_i, ρ_j were replaced by the Fermi-Dirac distribution functions $f_{n'}(\vec{k})$, $f_n(\vec{k})$ corresponding to the energy levels $\varepsilon_{n'}(k)$, $\varepsilon_n(k)$; E_j, E_i correspond to $\varepsilon_{n'}(\vec{k})$, $\varepsilon_n(\vec{k})$. The sum in III 7 is over all bands n, n' involved in the transitions, the surface integration is in the wavevector space over the surface of the constant energy differences given by

$$\varepsilon_{n'}(\vec{k}) - \varepsilon_n(\vec{k}) = \hbar\omega$$

The matrix element is given by the equation III 5; $\nabla_k = \frac{\partial}{\partial \vec{k}}$; the rest of the symbols are as above.

Equation III 7 predicts striking features in $\sigma^{1}_{ll}(\omega)$ near van Hove critical points (Callaway 1964) defined by equation

$$\nabla_k \left(\varepsilon_{n'}(\vec{k}) - \varepsilon_n(\vec{k})\right) = 0 \qquad \text{III } 8$$

i.e. denominator in III 5 is equal to zero and the integrand has a singularity. The critical points correspond to the direct optical interband transitions at those points in the Brillouin zone given by the wavevector $\vec{k}$ for which the bands n, n' are parallel.

In cases where critical points occur in relatively small parts of the Brillouin zone the matrix elements in III 7 can be safely assumed to be "slowly" varying functions of the wavevector $\vec{k}$, such that the optical conductivity is proportional to the quantity

$$J_{nn'}(\omega) = \int \frac{ds\,[f_n(\vec{k}) - f_{n'}(\vec{k})]}{\nabla_k \left(\varepsilon_{n'}(\vec{k}) - \varepsilon_n(\vec{k})\right)} \qquad \text{III } 9$$

usually called the joint density of states function; it measures the product density of full and empty states of equal energy difference. In this case the energy difference $\mathcal{E}_n(\vec{k}) - \mathcal{E}_{n'}(\vec{k})$ may be expanded in a Taylor series. The signs of the coefficients of the series are important in determining the behaviour of $J_{n\,n'}(\omega)$ near a critical point. The four types of the van Hove critical points determined by the coefficients correspond to the characteristic striking features in the behaviour of the optical conductivity as a function of frequency. The critical points usually occur at the symmetry points in the Brillouin zone. Also, due to the high symmetry of the states at the symmetry points the levels are usually highly degenerate.

The study of optical transitions is usually concentrated on the points of high symmetry in the Brillouin zone where the critical points may occur and optical transitions are relatively intense. An example of optical transitions which may occur at the critical points in the Brillouin zone for paramagnetic Gd is given in Fig III 1.

On the other hand when a number of critical points occurs at the same frequency, as may be seen to happen in the above example, it is very difficult to resolve any features in the optical spectra connected with the particular critical point.

Relatively more information may be obtained by studying the critical points where large portions of the Brillouin zone are involved, because the optical transitions are comparatively more intense than in the above case and are therefore better resolved in the optical spectra.

If a large portion of the zone is involved in the "critical points" the matrix element in III7 has to be considered as a function of the wavevector as has been discussed in detail by Aschroft and Sturm (1971).

An example of such critical points connected with magnetic ordering is discussed in the following section (3.4).

Selection rules

Selection rules of optical transitions between the states in the conduction band determine which of the possible transitions between the two states say $|i\rangle$ and $|j\rangle$ are allowed. They are given by non-zero matrix elements of the optical transitions given by equation III 3, i.e.

$$\langle j|\hat{H}_{rad}|i\rangle \neq 0 \qquad \text{III 10}$$

where $\hat{H}_{rad} = (e/2mc)\,\vec{A}\cdot\vec{p}$ is defined by III 1.

Two examples of the selection rules such as the conservation of spin and wavevectors during the transitions have been discussed above.

In general, selection rules follow from the symmetry properties, of the states involved in transitions. These states generally satisfy a one-electron Schrödinger equation of the type

$$\hat{H}|i\rangle = E_i\,|i\rangle \qquad \text{III 11}$$

Symmetry transformations of the Hamiltonian are those transformations of coordinates and spins which leave the Hamiltonian unchanged. Such transformations form a finite group called the symmetry group of the Hamiltonian. The properties of the symmetry group corresponding to the hexagonal close packed structure of the Rare Earths are described in Appendix A (for detailed treatment of the group theoretical background the reader is also referred to a number of textbooks such as Callaway (1964), Cornwell (1969) etc.). The symmetry of eigenfunctions $|i\rangle$ of the Hamiltonian is then characterised by irreducible representations of this group in matrix form. Traces of the matrices form the character tables which have a particular importance for working out selection rules of optical transitions.

Character tables of the irreducible representations of the symmetry groups corresponding to the hexagonal close

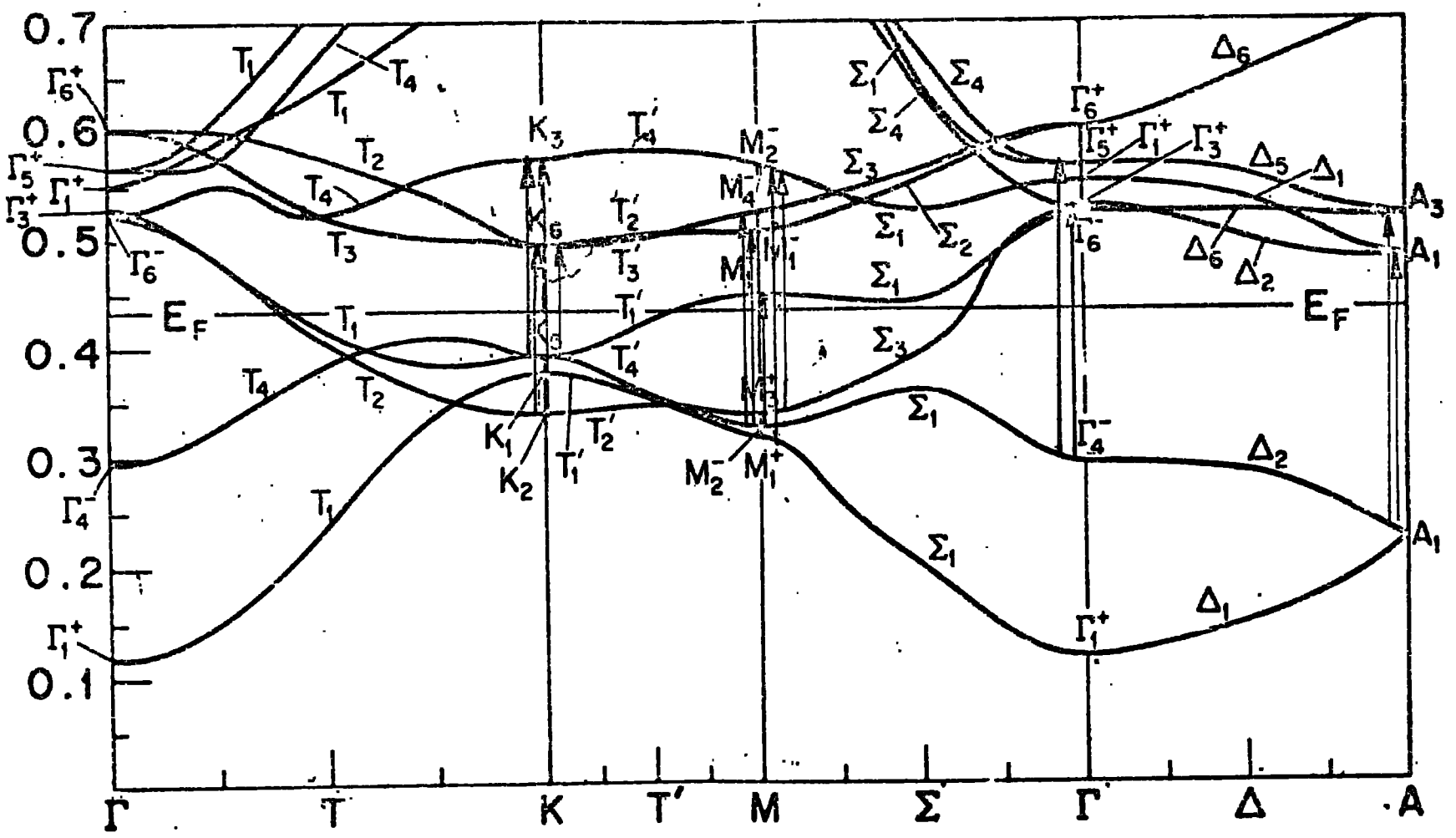

Fig.III.1
Optical transitions at the symmetry points in paramagnetic gadolinium metal(after Schüler (1965))

packed structure have been tabulated by Herring (1942) and Elliott (1954) for all symmetry points and axes of the Brillouin zone. With the help of some group theoretical considerations we can obtain the selection rules of optical transitions. For rare earth metals, these are tabulated for the critical points at the symmetry axes and points of the Brillouin zone in Appendix B.

Optical transitions in paramagnetic Rare Earths

In the case of a non-magnetic metal, the one particle Hamiltonian of conduction electron motion has the full symmetry of the crystal lattice. Selection rules therefore follow from the full symmetry of the crystal lattice and are discussed at length in Appendices A and B. Using Table B1 in Appendix B and non-relativistic energy bands for Gd shown in Fig.II 8 we can deduce the allowed interband transitions which occur in the Brillouin zone. Some of these are shown in Fig.III.1.

This clearly shows that numerous interband transitions occur between 1 eV and 2 eV. Since the rest of the heavy rare earths have practically the same energy band structure, the same diagram of allowed optical transitions applies for them also.

3.3 Intraband transitions

The interband transitions discussed in section 3.2 require a certain minimum energy corresponding to the separation between the energy bands.

However, the most common feature in the optical absorption of metals is a characteristic rise in absorption as photon energy approaches zero. This phenomenon is connected with the fact that conduction energy bands are partially occupied by electrons and transitions within these bands occur. These intraband transitions are indirect, because a change within a band must be associated with a change in crystal momentum; i.e. electrons undergo collisions during one optical period.

Absorption connected with these intraband transitions (free electron absorption) is in its isotropic form defined by the real part of optical conductivity $\sigma(\omega)$ given by a modification of Drude's equation (see for instance Hodgson (1970)).

$$\sigma(\omega) = \frac{\sigma(0)}{1+\omega^2\tau^2} \qquad \text{III 12}$$

where ω is the angular frequency, $\sigma(0)$ is the optical conductivity corresponding to zero frequency ($\omega=0$), τ is the electron relaxation time in isotropic form. $\sigma(0)$ is given by [Hodgson (1970)]

$$\sigma(0) = \frac{Ne^2\tau}{m^*_{opt}} \qquad \text{III 13}$$

where N is the number of free carriers per unit volume and m^*_{opt} is the optical effective mass. Its reciprocal value is an average of the electron velocity over the Fermi surface. If the material is anisotropic the Fermi surface is non-spherical and joint anisotropy of relaxation time and velocity over the Fermi surface should be considered. This would be the case of rare earth metals where the Fermi surface is very anisotropic as indicated in Fig II.10.

Hodgson and Cleyet (1969) used Eq.III.12 for the low energy extrapolation of room temperature optical conductivity $\sigma(\omega)$ of Gd films below 0.5 eV. The extrapolation was chosen by comparing the values of the real part of dielectric constant $\epsilon_1(\omega)$, obtained from $\sigma(\omega)$ by the Kramers-Krönig relations (Eq.VI.1) with those obtained experimentally.

The values of zero frequency optical conductivity $\sigma(0)$ obtained from extrapolation were comparable to values of d.c. conductivity $\sigma_{D.C.}$ ($\sigma(0)$ was slightly smaller than $\sigma_{D.C.}$). The good agreement of the two values suggests that thermal broadening effects at room temperature mask any possible structure in $\sigma(\omega)$ for photon energies below 0.5 eV. Slightly smaller values of $\sigma(0)$ with respect to d.c. values are expected, according to Abelés (1972); optical relaxation time includes the effects of both electron-electron and electron-photon collisions while electron-electron scattering plays no role in d.c. conductivity.

However, the above agreement may be only accidental since strong interband transitions may occur below 0.3 eV, as may be deduced from the calculated band structures.

In order to check this point, the extrapolations were carried out for the sequence of R.E. metals and the zero frequency values of the conductivity, $\sigma(0)$, were compared with the d.c. conductivity value. This is presented in Chapter VI.

3.4 Optical Transitions connected with magnetic ordering

3.4 (a) Ferromagnetic phase

New transitions in a ferromagnetic metal are connected with the exchange splitting of the conduction bands and with energy level shifts which are produced by magnetostriction. In this section we will only deal with the effect of the exchange splitting since the role of the magnetostriction is not yet sufficiently understood.

The optical effect of the exchange splitting can be divided into two types. The first are new transitions which occur when one of the spin-split subbands crosses the Fermi level and consequently reoccupation of the subband causes new transitions. This is the effect which is the most likely to occur in R.E. since there is a number of places in the Brillouin zone of R.E. with flat portions of the d-like bands near to the Fermi level. For this case there is no need to reconsider the symmetry of the new states in spin-split subbands and we therefore can in fact use the selection rules for a non-magnetic metal.

The other type of optical effect is connected with large mixing of the bands near the Fermi level due to the spin-orbit coupling making allowed dipole transitions between spin-split subbands(Dimmock et al (1965)). The energy of the spin orbit interaction was estimated by Watson et.al. (1968) to be approximately 0.4 eV. The estimated value for exchange splitting is 0.5 eV for Tb, 0.61 for Gd etc., as is shown in Table II 1. This means that intense parallel band transitions may occur in the region of 0.5 eV. As the bands near to the Fermi level are quite flat, large areas of the Brillouin zone are likely to be involved in these transitions and the joint density of states is very high. This type of effect has a very characteristic anomaly in the optical absorption spectra typical to all parallel band transitions. Optical conductivity

$\sigma(\omega)$ is given by the relation (Ashcroft and Sturm (1971))

$$\sigma(\omega) \sim \frac{(\Delta_{ferro})^2}{\left[(\hbar\omega)^2 - (\Delta_{ferro})^2\right]^{1/2}} \qquad \text{III 14}$$

where Δ_{ferro} is the exchange splitting defined and discussed in the previous chapter. Places where parallel band transitions due to exchange splitting are likely to occur are discussed in Section 6.1.

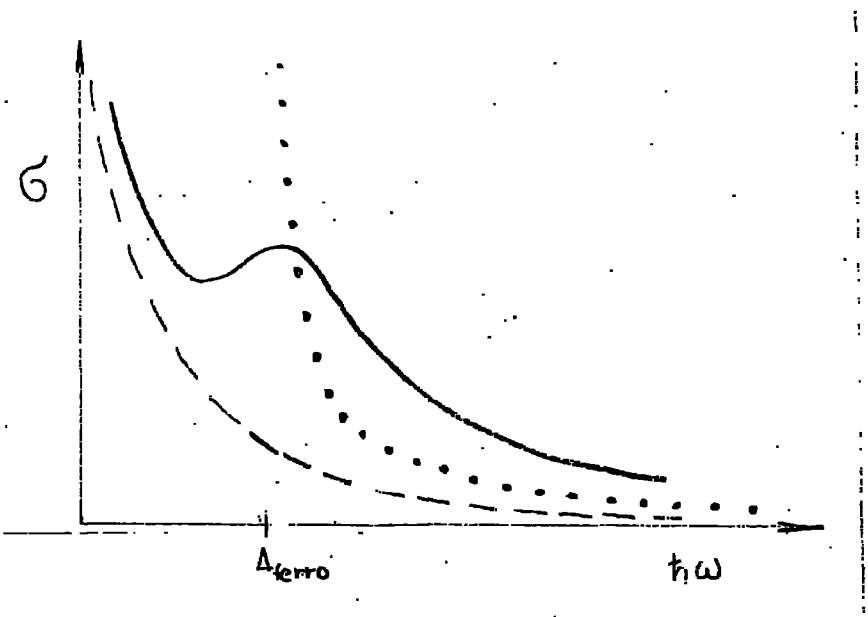

Fig III 2. Schematic diagram of the structure in the optical conductivity connected with transitions between the spin split parallel bands in ferromagnetic rare earth metals; dotted line is a theoretical curve given by equation III 14; dashed line is the Drude contribution.

The expression for absorption shows that the anomaly is in the form of a hyperbolic function with the singularity for $\hbar\omega = \Delta_{ferro}$. If the free-electron contribution and the thermal broadening are also considered, the optical conductivity $\sigma(\omega)$ takes the form as indicated by the full line in Fig III 2.

Summarising it can be said that a unique structure has been ~~found~~ suggested in the spectral dependence of optical absorption which corresponds to the ferromagnetic exchange splitting of the conduction bands.

3.4 (b) Effect of superzone boundaries on the optical properties

As suggested by Miwa (1963) optical transitions can occur across gaps at the superzone boundaries induced by a periodical spin structure. Superzone boundaries are planes bisecting vectors $\vec{P} = (\vec{k}_n + \vec{Q})$, where $\vec{Q}$ is the wavevector characteristic of the periodic potential of the spin structure, (defined by Equation II 1), $\vec{k}_n$ is a reciprocal lattice vector. Considering the simplest model, that of almost free electrons with the isotropic effective mass, optical conductivity associated with the transitions across the gap at the superzone boundary $\vec{P}_n = (\vec{k}_n + \vec{Q})/2$ is given by Miwa (1963).

$$\sigma(\omega) \sim (\cos^2\lambda\, P_n)/(\hbar^2\omega^2((\hbar\omega)^2 - \Delta^2)^{\frac{1}{2}} \times 1/m^* \qquad \text{III 15}$$

λ is the angle between the polarization vector of the radiation and the vector $\vec{P}$. Δ is the energy gap at the superzone boundary given by equation II 11 depending on the type of the periodic structure and m* is the effective mass of the conduction electron.

The shape of the absorption band is very similar to that produced by the ferromagnetic exchange splitting and is schematically shown below in Fig.III.3. The dashed curve in this figure shows the $\sigma(\omega)$ curve predicted by Eq.III.15. The full curve shows that obtained by considering life-time broadening and free electron absorption.

The above peak in the optical absorption spectrum is strongly dependent on the size of the gap and the type of the structure. Miwa's theory therefore predicts some changes in $\sigma(\omega)$ at the transition between anti-

ferromagnetic and ferromagnetic phases which is in disagreement with the experimental results. The question of the role of superzone boundaries is therefore left until optical properties of single crystals are thoroughly investigated.

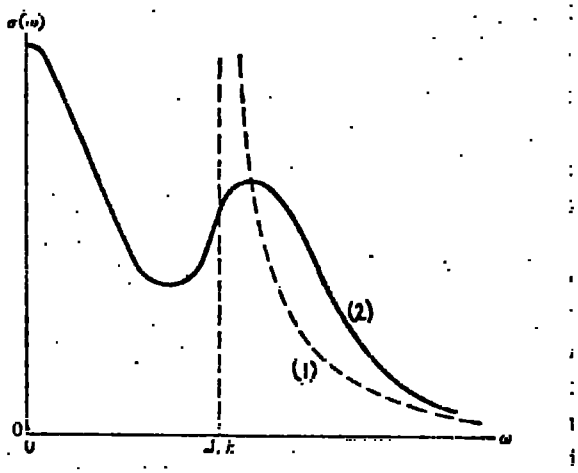

Fig.III.3. Schematic diagram of the structure in the optical conductivity curve connected with the band gaps at the antiferromagnetic superzone boundaries (from Miwa 1963). (1) Predicted by Eq.III.15; (2) Life-time broadening and free electron absorption included.

3.5 Contemporary Data on Optical Properties of Rare Earth Metals and comparison with other Magnetic Metals

3.5 (a) Optical properties of trivalent R.E.

Considerable effort has been devoted by Schüler (1963, 1966) to measuring the optical properties of Gd, Dy, Ho and Lu. The absorption bands are broad and it is not possible to relate the numerous critical points in the band model to the spectral structure of optical constants at room temperature. In the magnetic phases new optical anomalies were observed in Gd, Dy, Ho and it is reasonably clear that these anomalies are related to the magnetic ordering. No low temperature changes except those due to a Drude contribution were observed for instance in Lu which is non-magnetic and has a band structure very similar to the rest of the heavy rare earths.

As an illustrative example we quote Fig III.4 obtained by Hodgson and Cleyet (1969) measuring optical constants of Gd thin films by a polarimetric reflection method. The room temperature data show one broad peak in optical conductivity $\sigma(\omega)$ extending from 0.6 eV to 2.5 eV. On cooling far below the Curie point of Gd bulk material (T_c = 289°K) new, quite pronounced, peaks in $\sigma(\omega)$ were observed at photon energies 0.7 eV and 1.8 eV and a very small structure at 1.1 eV. The calculated reflectivity and transmission data agreed with the results of Schüler (1965). The peak in $\sigma(\omega)$ at 0.7 eV was attributed to the transitions between the spin-split bands. The size of the band-gap produced by ferromagnetic exchange splitting is assumed to be of the same size for Gd. (Watson et.al. 1968).

The elements with helical spin structures below the first ordering temperature show rather complicated phenomena and so far it is not clear what is the origin of the optical effects of magnetic ordering of those metals. Cooper and Reddington (1965) reported an attempt to record

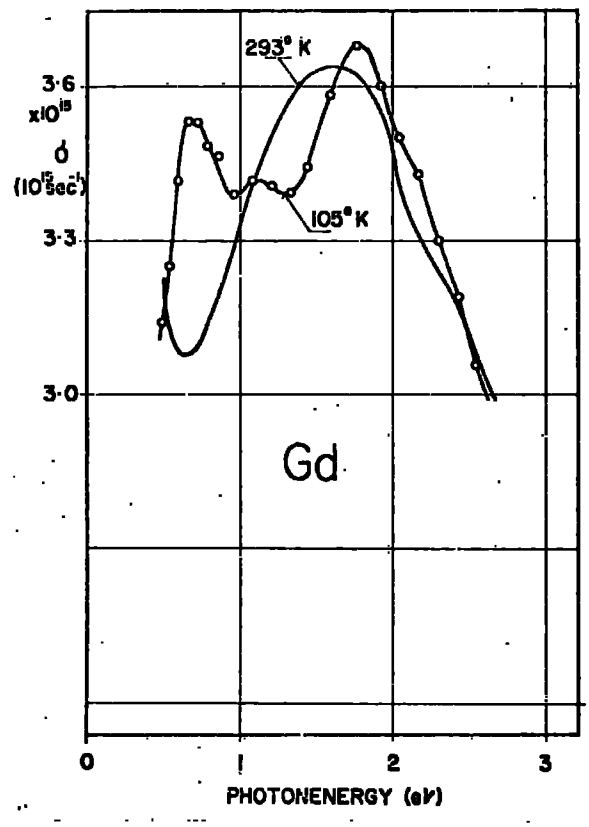

Fig.III.4 Optical conductivity $\sigma(\omega)$ of gadolinium films (after Hodgson & Cleyet (1969)) measured at 293°K and 105°K.

changes in optical absorption of Dysprosium thin films during transition from the helical to the ferromagnetic ordering by the application of a magnetic field in excess of critical field strength. No changes in absorption due to the transition were observed. The ferromagnetic splitting of the conduction band was calculated by Watson et.al. (1968) and appears to be approximately the same as the size of the energy band gaps produced by helical spin structures at magnetic superzone boundaries. (This is discussed in detail in the following chapter). From this Watson et.al. conclude that "no appreciable changes in absorption due to transfer into the ferromagnetic region are to be expected". Even though the sizes of the gaps and consequently the positions of optical anomalies on the photon energy scale are not expected to change during this transfer it does not mean that the shape of the anomaly should necessarily stay fixed. This would rather suggest that superzone boundaries do not contribute to the optical effects of magnetic ordering and that a more general approach to the problem has to be taken.

Optical constants of very thin films of rare earth metals Gd, Tb, Tm, Ce and Nd were reported by Pétrakian (1972). These films were prepared in static ultra high vacuum conditions at a pressure of 10^{-10} mm.Hg. Even though the results seem to show some similarities with those obtained on thick samples ($\sim 2000A^{\circ}$) overall agreement with them is rather poor. (Compare for instance the Gd data obtained by Pétrakian (1972) and Hodgson et al. (1969)). The source of these differences may be associated with the thickness itself, since in a study of the variation of the characteristics of rare earth films with thickness Lodge (1969) has shown that below $500A^{\circ}$ the magnetic and electrical behaviour of the film rapidly deviates from that of bulk material. We would rather exclude these results from our further discussion.

Photoemission investigations on several heavy elements recently reported by Brodén (1971) did not show any sign of structure in the photoemission spectra in the energy region 0 eV -10 eV below the Fermi energy, which could be attributed to the transitions from 4f-shell. This suggests that 4f states in the heavy elements are too far below the Fermi level to be observed in this photon energy range. This could be taken as further support for the theory of magnetic ordering described in Section 2.3.3 which is based on assumption, that 4f-electrons are localized.

3.5 (b) Comparison with other magnetic metals

Before the subject of the optical properties of magnetic rare earth materials reported in the literature is closed it would be interesting to compare these with published work on the optical properties of other magnetic materials such as Cr, Ni. The optical properties of these metals have been studied more extensively than those of rare earths most probably because Ni and Cr are less reactive in air and have a simpler band structure than rare earths. Also the band structure of Ni is closely related to that of Cu which has been studied in the most detail in the past (for a review see Abelés (1972) Section 3.3.3) and is well understood.

There is therefore a good chance of finding some general indication of the processes which make the most important contributions to the optical effects of magnetic ordering of metals in general.

As a first example Nickel will be considered. It is ferromagnetic below 580°K and its ferromagnetic exchange energy is found to be approximately 0.4 eV (Hanus et al 1968).

It has been found by (Scouler (1967)) that the ferromagnetic ordering induces new structures in temperature modulated reflectance spectra at photon energies 0.25, 0.40 and 1.3 eV. The most successful interpretation has been reported by Hanus et al (1968). They have connected these absorption peaks with exchange splitting of conduction bands. In their theory the ferromagnetic exchange produces two types of the band structure, one of them corresponding to the electrons with spin ↑ the other to those with spin ↓. The exchange splitting of the levels near to the Fermi level leads to their reoccupation and consequently new transitions occur. Both majority and minority bands contribute to the effect. For instance the peak at 0.25 eV corresponds to transitions between majority spin bands; peaks at 0.40 eV and 1.3 eV correspond to minority spin band transitions.

The above theory is thought to be the most likely explanation of the effects in Nickel in ferromagnetic phase and is also considered for discussion of the present results on rare earth metals as may be seen in section 3.4 and chapter VI.

However, there may be another mechanism involved in the optical effect of exchange splitting. As discussed in section 3.4 the presence of a strong spin-orbit coupling mixes the spin character of the conduction electron states making the transitions between the "spin up" and "spin down" bands allowed. The above may be investigated by a study of magnetooptical spectra since the spin-orbit interaction makes a contribution to the non-diagonal elements of the dielectric tensor which is responsible for the Kerr-effect (Cooper 1965).

However, as may be seen from Krinchick (1969, 1970, 1971) although the Kerr effect was found to be relatively large in Nickel the magnetooptical anisotropy failed to be explained by considering solely the effects of spin-orbit coupling. Parker (1972) shows that the anisotropy can be explained satisfactorily by considering, in addition to the effects of spin-orbit coupling, the anisotropic effects of magnetostriction.

The above suggests that spin orbit coupling is probably not comparable with the exchange splitting in Ni and the mixing of spin character mentioned in section 3.4 is not large enough for optical transitions between the spin split bands to occur. The role of magnetostriction has been briefly discussed in the section 2.3.4.

The other metal that may seem to be relevant is antiferromagnetic Cr. Below the Néel temperature it shows an optical absorption band near 0.12 eV (Barker et.al. 1968). A model for the interpretation of this absorption band is based on the theory of itinerant antiferromagnetism and is formally similar to the theory of the band gaps connected to the superconductivity (Fedders and Martin 1966). Here, too, one thinks of two band structures,

one for electrons with spins in phase with antiferromagnetism and the second for electrons with spins out of phase. In agreement with the experimental results the theory predicts an absorption maximum at approximately 0.12 eV which is temperature dependent and disappears above the Neél point.

However, the usual approach to the magnetic properties of Rare Earth metals uses the localized moment model and it would not seem that the interpretation used for the Chromium results would be relevant for the discussion of the results reported in this thesis.

CHAPTER IV

EXPERIMENTAL - APPARATUS

4.1 Introduction - Discussion of experimental methods

A particular problem in all optical studies on metals is that of sample preparation. For the rare earth metals, the ordinary methods of polishing and etching fail because of their extreme reactivness. Most of the work, therefore, has been done on thin films prepared in high vacuum conditions and protected by a thin layer from exposure. It is,however,frequently found that thin metal films have properties different from those of bulk material. In order to examine this point, the resistivity variation with temperature was measured on each evaporated film and the results compared with those of polycrystalline material published in the literature. The results show that the curves are essentially identical apart from the expected difference in residual resistance due to built in strain in the films.

The second problem is associated with the selection of the right method of film preparation for optical measurements. Results published by several authors on rare earth metals show that even the use of ultra-high vacuum condition such as 10^{-9} mm Hg used by Blodget et.al (1965) is not enough to protect the surface of the films from gradual oxidation and subsequent change of optical constants.

On the other hand, the optical constants of metals are best determined by studying reflected radiation. The examination of transmitted light is restricted by strong absorption in the visible and infra-red region to the use of very thin specimens ($< 800\text{Å}$ or less) and the question then arises as to what extent the properties of such specimens accord with those of bulk materials. In studies by reflection the relevant thickness is directly related to the penetration depth of the electromagnetic radiation and care must be taken in the preparation of representative surfaces.

In order to avoid oxidation while still maintaining good surface

conditions R.E. metals were deposited on to the base of a silica prism in high vacuum and covered by a protective layer of SiO.

The most accurate method of measuring the optical constants $\underline{n}$ and $\underline{k}$ (or ε_1 and optical conductivity σ) in the visible and infrared region is by the use of phase compensators, but unfortunately these compensators are usually restricted by absorption to wavelengths less than 2.5μm. These methods measure the ellipticity of polarised light reflected from the metal surface. There are though several other methods for measuring optical constants which require only one or two polarisers. One of them measures the principal angle of incidence $\bar{\theta}$ and azimuth $\bar{\psi}$.* Its advantage lies in the fact that it uses a detector of radiation only as means of indicating the equality of two optical intensities. However, this method is not suitable for most metals at wavelengths greater than 2.5μm because of the large values of $\bar{\theta}$ which occur. Further, this method is inconvenient since it needs a continuous change of the angle of incidence which leads to great difficulties if an internal reflecting surface is used. The values of optical constants can be found by measurements of reflectivity for at least two values of the angle of incidence (Bueche 1948). The method is not capable of high accuracy because the variation of reflectivity with θ is not sensitive to changes in ε_1 and σ . Before proceeding further in a discussion of the experimental apparatus it is necessary to mention briefly other work on the optical properties of the Rare Earth metals, namely that reported by Schüler (1964, 1965). Schüler observed anomalies in the low temperature reflectivity of the several heavy rare earth metals in the region 0.3eV - 0.5eV of photon energies. A classical technique of obtaining optical constants from the transmission and reflectivity data used by this author appear to be quite adequate for the first investigations of the optical effects of magnetic ordering in

* Ingersoll (1910)

the heavy rare earths. However, absolute values of the optical constants and even positions of the peaks derived from such measurements appeared to be quite inconsistent and therefore more accurate techniques have to be used to obtain meaningful information about optical effects of magnetic ordering.

In the present work the optical constants were determined by the polarimetric reflection method. This depends on the analysis of the elliptically polarized radiation obliquely reflected from a metallic film. (Basic principles of the polarimetric (or ellipsometric) method are presented in Appendix D). In the present case the metallic surface at the film-substrate interface was examined; the fused silica served as a transparent dielectricum. This method has the advantage that it requires measurements at only one, arbitrary, value of the angle of incidence φ. This advantage becomes important for measurements at helium temperatures where a rather elaborate cryostat had to be used. The method can also be made quite accurate for the determination of optical constants which gives an opportunity to study fine structures in optical absorption spectra due to the magnetization processes.

In order to check consistency of the polarimetric method, the reflectivity coefficient was calculated from the optical constants obtained by polarimetry and compared with the reflectivity coefficient directly measured. A block diagram of the reflectivity method used in the present work is shown in Fig IV.4. The sample reflecting surfaces for reflectivity measurements were prepared similarly to those for ellipsometry. Metallic films were deposited onto a silica glass plate and covered by a protective layer of SiO. The reflectivity was measured by examination of the reflection at the metal-to-substrate interface. A simple liquid nitrogen cryostat was made to examine reflectivity of R.E. films at low temperatures (as indicated in Fig IV.4). Some of the

results are presented in chapter V.

4.2 Theory of the ellipsometric method

In order to simplify the understanding of later sections of this thesis, it will be convenient at this point to examine the theory of the ellipsometric method of determining the optical constants. In this method plane polarized monochromatic radiation is obliquely reflected by a specimen and passes through an analyzer to the detector. If the intensity transmitted by the analyzer ← specimen ← polarizer system is $I(\psi_P, \psi_A)$ for azimuths ψ_P, ψ_A of the polarizer and analyzer respectively then $I(\psi_P, \psi_A)$ is of the form

(Beattie & Conn (1955))

$$I(\psi_P, \psi_A) = I_o (\sin^2\psi_P \sin^2 \psi_A + \varsigma^2 \cos^2\psi_P \cos^2 \psi_A + \tfrac{1}{2}\sin 2\psi_P \cdot \sin 2\psi_A \cos\Delta) \qquad \text{IV 1}$$

where ς and Δ are quantities defined in Appendix D by the equation

$$\varsigma e^{i\Delta} = \frac{R_p}{R_s} \quad . \qquad \text{IV 1a}$$

$R_p R_s$ are the complex reflection coefficients for the "parallel" and "perpendicular" components with respect to the plane of incidence. I_o is the intensity of radiation reflected from the metallic surface and is given by (Beattie & Conn (1955))

$$I_o = \tfrac{1}{2} \left| E^{(0)} \right|^2 . R^2$$

where R^2 is the reflectivity from the surface. Measurements of the transmitted signal are required for at least three different azimuths to obtain ς and Δ and to exclude terms dependent on the intensity of incident radiation $\left| E^{(0)} \right|^2$. At a fixed azimuth of the polarizer

(i.e. $\psi_P = \frac{\pi}{4}$) the transmitted intensity $I(\frac{\pi}{4}, \psi_A)$ is measured for three different azimuths of the analyzer $\psi_A = 0; \frac{\pi}{4}; \frac{\pi}{2}$. ($0, \frac{\pi}{2}$ corresponding to the plane of polarization parallel to and perpendicular to the plane of incidence respectively). The two ellipsometric parameters are then given by expressions

$$\rho = \sqrt{\frac{I(\frac{\pi}{4}, 0)}{I(\frac{\pi}{4}, \frac{\pi}{2})}} \qquad \text{IV 2}$$

$$\cos\Delta = \frac{I(\frac{\pi}{4}, 0) + I(\frac{\pi}{4}, \frac{\pi}{2}) - 2 \cdot I(\frac{\pi}{4}, +\frac{\pi}{4})}{2 \cdot \sqrt{I(\frac{\pi}{4}, 0) \cdot I(\frac{\pi}{4}, \frac{\pi}{2})}} \quad .$$

Equation IV 1 is symmetrical in ψ_A, ψ_P so that the polarizer and analyzer are interchangeable.

Role of detector

If the radiation detector shows polarization then the corresponding output from the radiation receiver is given by

$$I(\psi_P, \psi_A) = T(\psi_A, \lambda)\, I(\psi_P, \psi_A)$$

$I(\psi_P, \psi_A)$ is given by Eq IV.1 and $T(\psi_A, \lambda)$ allows for the instrumental polarization. In general it is dependent on the wavelength λ of the radiation. In this case Eqs. IV.1 and IV.2 have to be altered accordingly. The determination of the $T(\psi_A, \lambda)$ is discussed in section 4.4.4.

Computing the Optical Conductivity and Dielectric Constants

In this section we will restrict ourselves to thin films which are the subject of this thesis. This means that we assume the dielectric constants to be isotropic and there is no optical activity;

combining Eqs. D12 and IV.1a using the same notation as above we can write (Beattie & Conn (1955))

$$\frac{\sqrt{\varepsilon - \varepsilon_o \sin^2\varphi}}{\sqrt{\varepsilon_o}\tan\varphi \sin\varphi} = \frac{1+\frac{R_p}{R_s}}{1-\frac{R_p}{R_s}} = \frac{1+\varrho e^{i\Delta}}{1-\varrho e^{i\Delta}} = \tan P \cdot \exp(iQ). \qquad \text{IV 4}$$

$\varepsilon = \varepsilon_1 + i\varepsilon_2$ is complex dielectric constant of the metal film; φ is the angle of incidence; ε_c is dielectric constant of Spectrosil ϱ and Δ are defined by Eq. IV.1a, R_s, R_p are complex reflectivity coefficients defined above.

$$\tan^2 P = \frac{1 + \varrho^2 + 2\varrho \cdot \cos\Delta}{1 + \varrho^2 - 2\varrho \cdot \cos\Delta}$$

$$\tan Q = \frac{2\varrho \cdot \sin\Delta}{1 - \varrho^2} = x \qquad \text{IV 5}$$

$$\sin 2Q = \frac{2x}{1+x^2} \cdot \qquad \cos 2Q = \frac{1-x^2}{1+x^2} \cdot$$

Hence from IV.4 and IV.5 we have ($\varepsilon_1 = n^2-k^2$; $\varepsilon_2 = 2 \cdot n \cdot k$; n , k are optical constants of the metal film in the usual notation)

$$X(n^2 - k^2) = \frac{n^2 - k^2 - \varepsilon_o \sin^2\varphi}{\varepsilon_o \, tg^2\varphi \, \sin^2\varphi} = \tan^2 P \cdot \cos 2Q$$

IV 6

$$Y(2nk) = \frac{-2nk}{\tan^2\varphi \, \sin^2\varphi \, \varepsilon_o} = \tan^2 P \cdot \sin 2Q \cdot$$

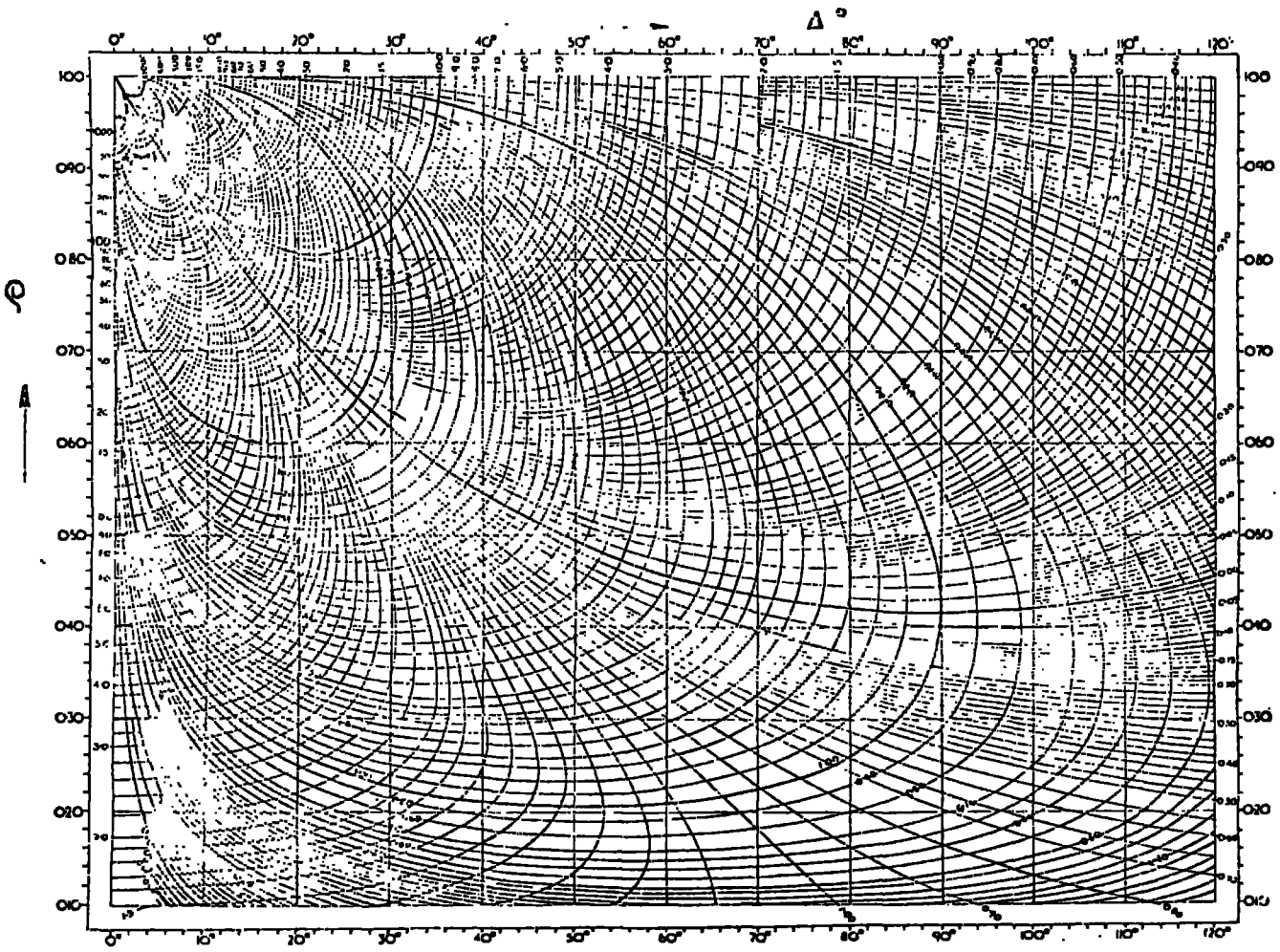

Fig.IV.1 Contours of X and Y defined by Eq.IV.6 referred to rectangular axes φ and Δ . φ and Δ are defined by Eq. IV 1a. (from Battie & Conn (1955)).

These two equations were used for the calculation of the real and imaginary parts of the dielectric constant and the optical conductivity using the computer programme shown in Appendix C. Fig IV 1 shows the families of contours of $X(\varphi, \Delta) = \text{const}$ and $Y(\varphi, \Delta) = \text{const}$ which can be divided into two types. The first types of contours are closed loops which terminate at the top left hand corner of the diagram. The abscissa are Δ, the relative phase. The ordinates are amplitude ratios φ. These loops are the loci of constant values of

$$Y (2 n k) \qquad \text{see equation IV.6.}$$

The second set of contours are very roughly orthogonal to $Y(2 nk) = \text{const}$ and are loci of constant values of

$$X (n^2 - k^2) .$$

Even though this chart was not used for the calculation of ε_1, ε_2 it was a very practical aid for an estimation of errors and a quick examination of the measured quantities.

The real and imaginary parts of the dielectric constant

ε_1, ε_2

and $\frac{\sigma}{c} = \frac{\text{optical conductivity}}{\text{light velocity}}$

were the output from the computer. The latter term is directly proportional to the energy of radiation absorbed per unit volume per unit time.

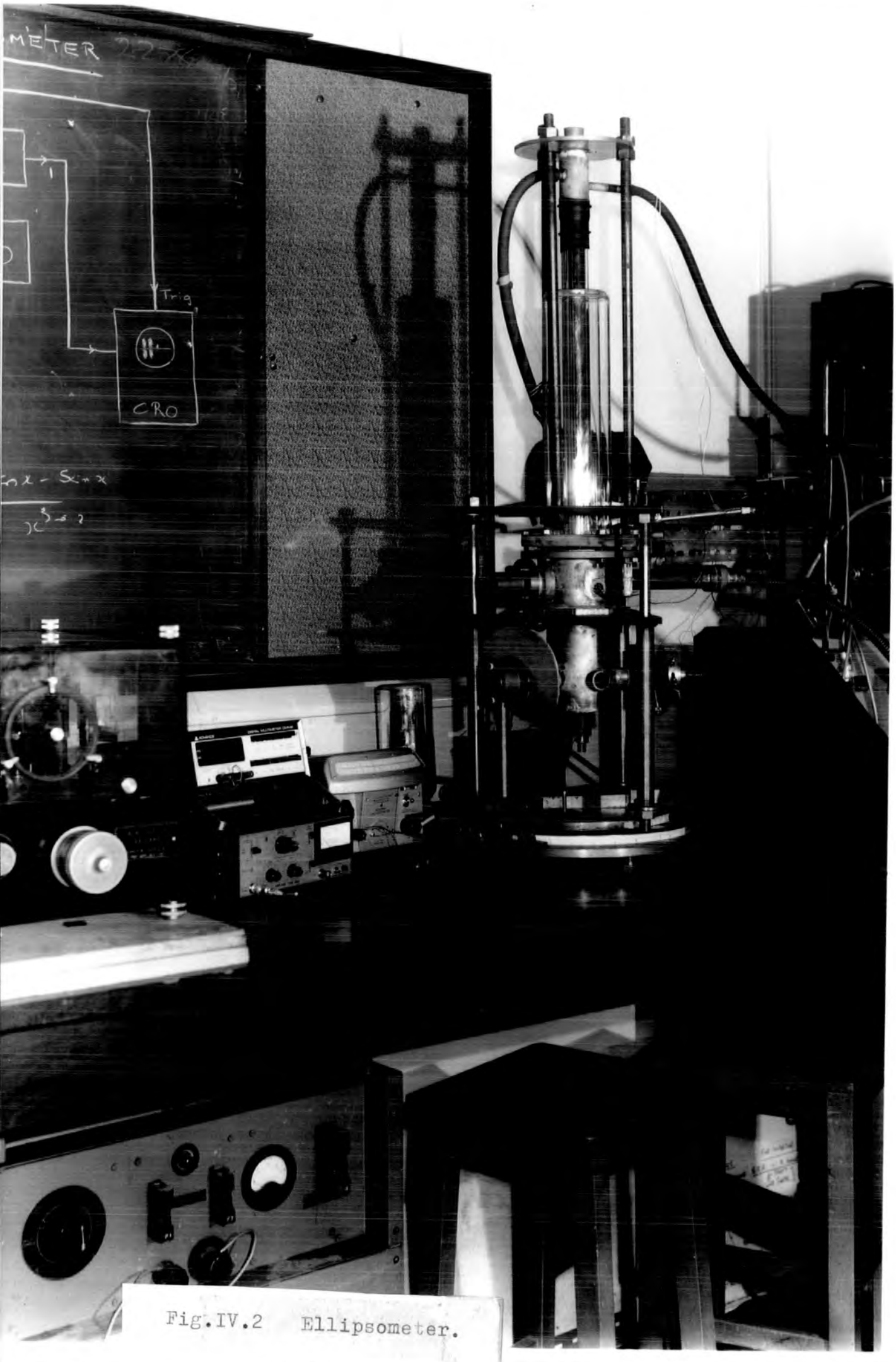

Fig.IV.2 Ellipsometer.

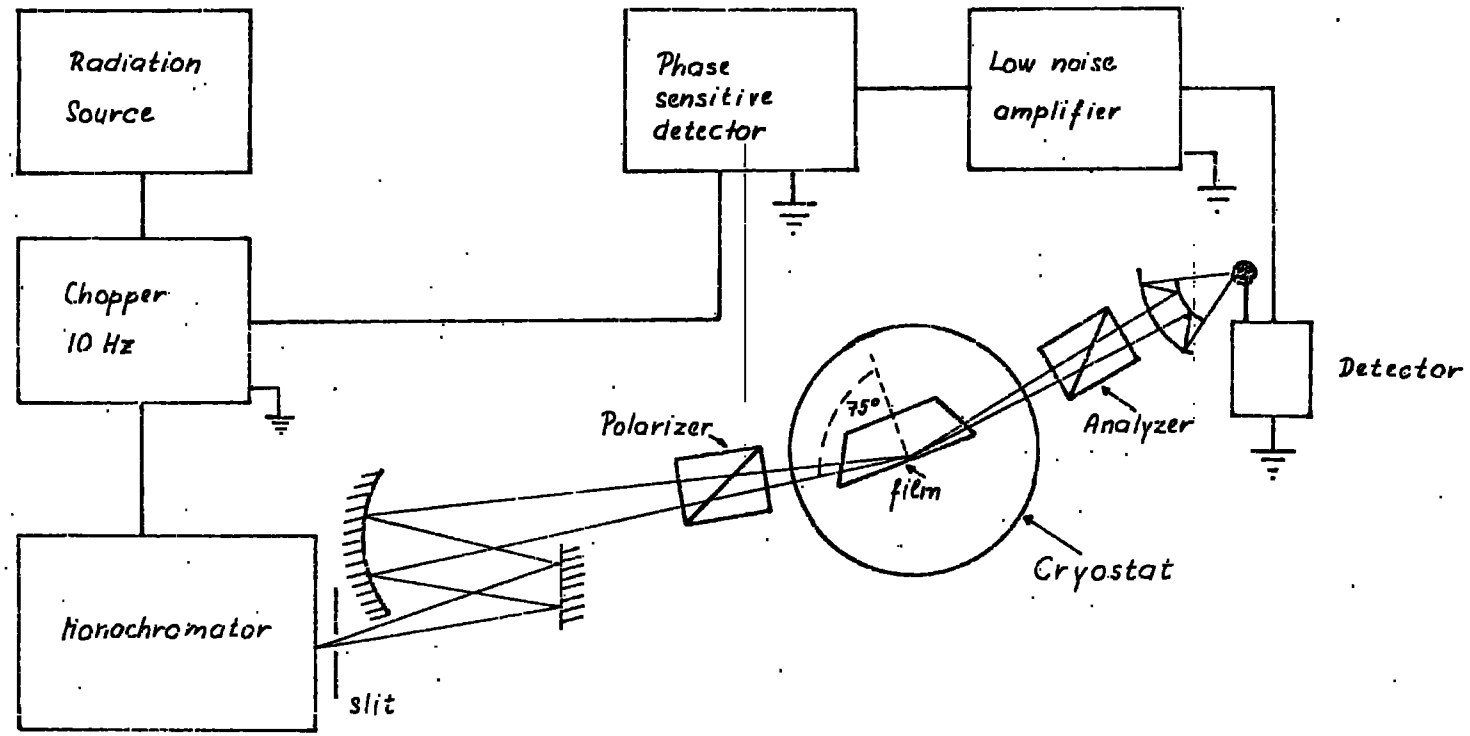

Fig.IV.3 Block diagram of the polarimetric method.

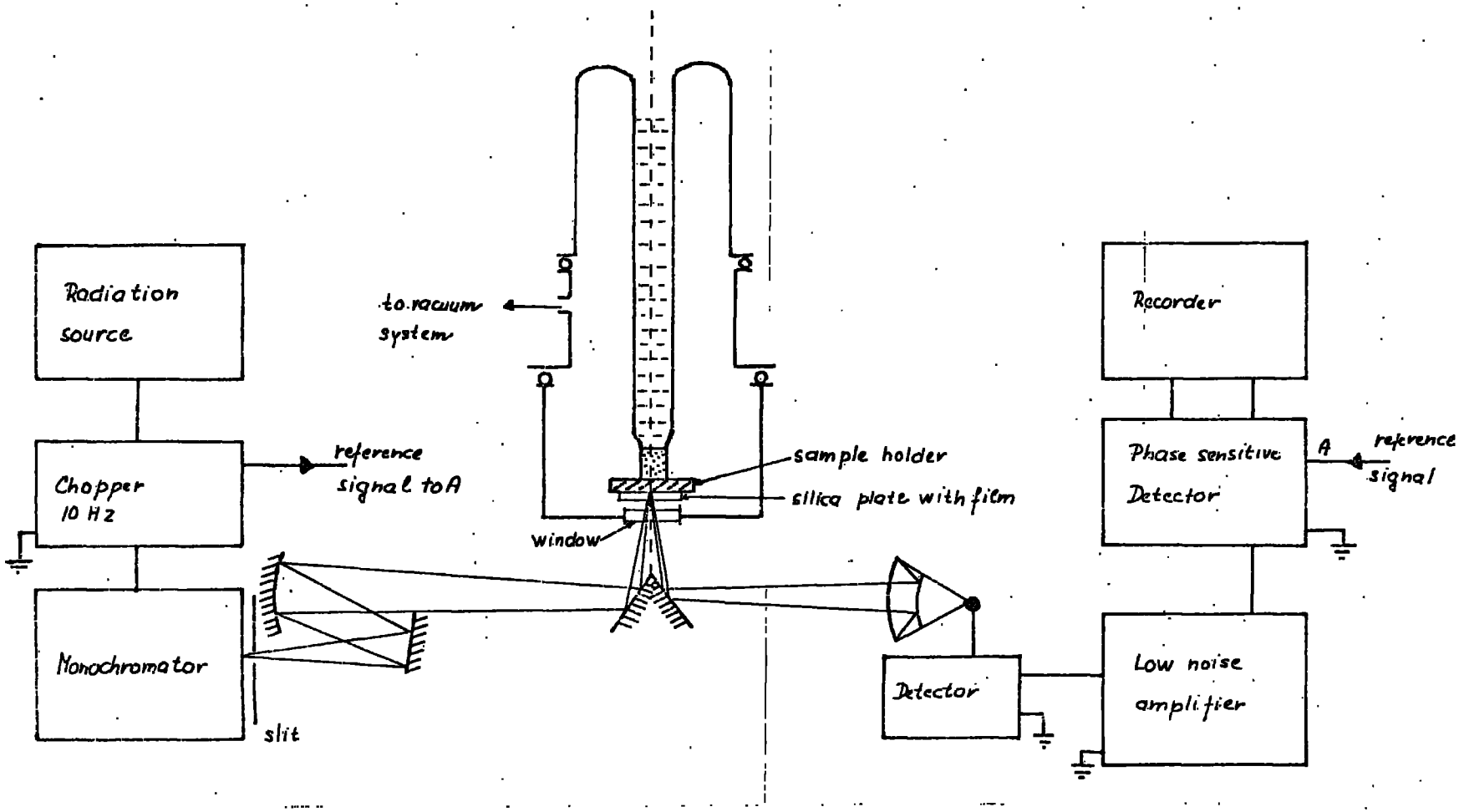

Fig.IV.4 Block diagram of reflectivity measurments.

4,3 Experimental errors and description of settings

4.3.1 Azimuths of polarizer and analyzer

Both azimuths ψ_p, ψ_A are measured with respect to the plane of incidence. The origins of the azimuths ψ_A^o, ψ_p^o were approximately located by observing a minimum of the radiation intensity $I(\psi_p^m, \psi_A^m)$ passing through the system. The minimum intensity $I(\psi_p^m, \psi_A^m)$ occurs when the incident radiation is polarized parallel to the reflecting surface (i.e. $\psi_p^m = \psi_p^o + \frac{\pi}{2}$) and the analyzer is set so as to pass radiation polarized parallel to the plane of incidence (i.e. $\psi_A^m = \psi_A^o$). The zero azimuths ψ_p^{10}, ψ_A^{10} obtained in this way differ by $\delta\psi_p$ and $\delta\psi_A$ from the true readings. $\delta\psi_p$ and $\delta\psi_A$ are then determined in two stages (Beattie & Conn (1955)). In the first experiment the polarizer is set at a nominal azimuth of $\frac{\pi}{2}$ and intensities are compared for two settings $\pm\psi_A^1$ of analyzer. Zero azimuth of the analyzer (i.e. $\delta\psi_A = 0$) is given by equality of the above two intensities. In this way the analyzer azimuth may be set very accurately; in the present work $\delta\psi_A = 0^o \pm 0.1^o$. $\delta\psi_p$ was determined to the same accuracy by the second experiment in which the following ratios of intensities are compared

$$\alpha = \frac{I(\psi_p', 0)}{I(\psi_p^1, \frac{\pi}{2})} \qquad \beta = \frac{I(\psi_p^1 + \frac{\pi}{2}, 0)}{I(\psi_p^1 + \frac{\pi}{2}, \frac{\pi}{2})} \quad . \qquad \text{IV 7}$$

$\delta\psi_p = 0$ if $\alpha = \beta$ and $\psi_p = \frac{\pi}{4}$.

In order to achieve maximum accuarcy in the settings of ψ_p and ψ_A the above experiments were carried out at wavelengths for which the radiation receiver was the most sensitive; then the errors in azimuths may be neglected with respect to errors due to random fluctuations of intensities.

4.3.2 The reflectance ratio

If ψ_p is set to be 45°, then from equation IV.2 the relative change of ρ due to random fluctuations of intensities $\frac{\delta I}{I}$ is [Battie + Conn (1955)]

$$\frac{\delta \rho}{\rho} = \frac{\delta I}{I}\left(1 + \frac{1}{\rho^2}\right) \qquad \text{IV 8}$$

As an example, taking as a practical figure $\frac{1}{300}$ for $\frac{\delta I}{I}$ equation IV.8 indicates that $\frac{\delta \rho}{\rho}$ is about 1.6% for $\rho = 0.5$ which is the case for most of heavy Rare Earth elements in the near infra-red region.

4.3.3 The relative phase

For the estimation of the error $\delta\Delta$ in the relative phase readings due to random fluctuations the following relation may be used (Beattie & Conn (1955))

$$\delta\Delta = \frac{\delta I}{I}\sqrt{\frac{1 + \cos\Delta}{1 - \cos\Delta}} \qquad \text{IV.9}$$

which means that the minimum $\delta\Delta$ occurs at $\Delta = \frac{\pi}{2}$.
Using a similar practical value for $\frac{\delta I}{I}$ of $\frac{1}{300}$ we find that if Δ is less than $\frac{\pi}{6}$ and greater than $\frac{7}{6}\pi$, the random error in the readings of the relative phase is greater than 5°. In most of the cases for the heavy rare earths in the infra-red region up to $4\mu m$ the relative phase was in the interval $\left\langle \frac{\pi}{3}, \frac{4\pi}{3} \right\rangle$ which means

$$\delta\Delta \leqq \pm 0.2^\circ .$$

Having derived values $\delta\Delta$ and $\frac{\delta\rho}{\rho}$ (and knowing values ρ and Δ, of course) we can obtain the random error in optical conductivity σ and dielectric constants ε_1, ε_2. To do this either Eq. IV 6 combined with IV 5 or Fig IV 1 may be used. The use of Fig IV 1 is explained in section 4.2.

4.3.4 Angle of incidence

From Eq. IV 6 we can deduce the errors in deterimination of dielectric constants ε_1, ε_2 and optical conductivity σ due to errors in setting of the angle of incidence φ. These are given by

$$\frac{\delta \varepsilon_1}{\varepsilon_1} = \frac{\delta \varepsilon_2}{\varepsilon_2} = \frac{\delta \sigma}{\sigma} = \frac{\delta (\tan^2\varphi \sin^2\varphi)}{\tan^2\varphi \sin^2\varphi} = \frac{\tan\varphi (2+\cos^2\varphi)}{\sin^2\varphi} \quad \text{IV.10}$$

The error due to incorrect setting of φ increases with increasing φ. From section 4.3.3 it follows that the method is the most accurate if φ is equal to the principal angle of incidence $\overline{\varphi}$ for which the relative phase $\Delta = 90^\circ$. For R.E. metals in the near infrared $\overline{\varphi} \cong 75^\circ$. φ was therefore set at 75°.

The error which arises from the inaccuracy of setting φ was $\delta\varphi \leq \pm 0.1^\circ$ of arc which corresponds to

$$\frac{\delta \sigma}{\sigma} = \frac{\delta \varepsilon_{1,2}}{\varepsilon_{1,2}} \leq \pm 1.6\%$$

4.4 Apparatus for the Polarimetric Method

4.4.1 Optical system - Introduction

Fig IV.2 and IV.3 show the experimental arrangement of the apparatus used in these measurements. The source of radiation and the monochromator were made into one unit. The monochromatic radiation was then plane polarized with the plane of polarization at 45° to the plane of incidence. The elliptically polarized radiation reflected from the metallic film is studied by an analyzer. These measurements of the signal in the radiation detector were made at each wavelength for ($\Psi_P = \frac{\pi}{4}$; $\Psi_A = 0; +\frac{\pi}{4}$; $\frac{\pi}{2}$). From these three recorded

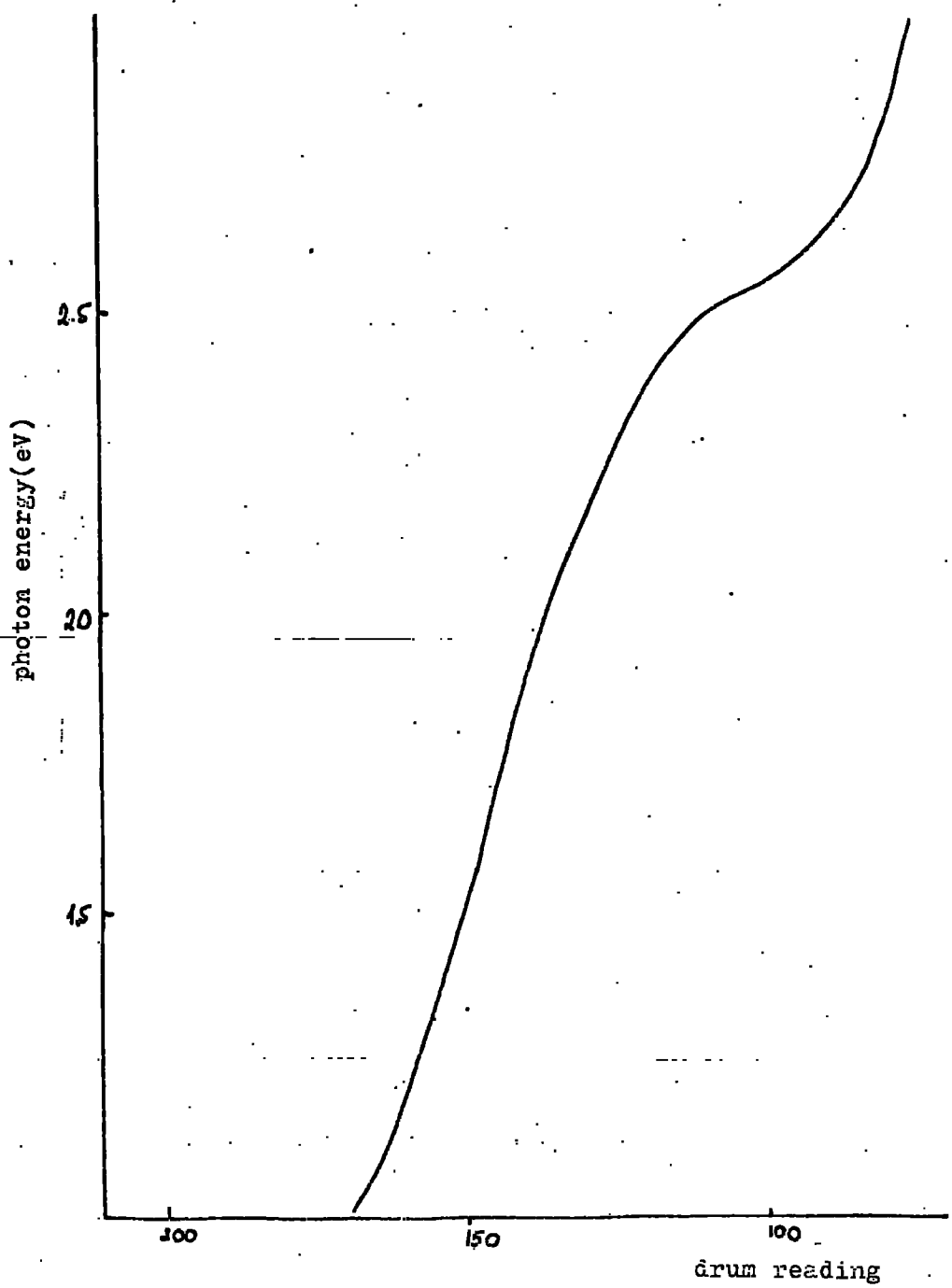

Fig.IV.5 Calibration curve of Spectrosil prism (Grubb-Parsons spectrometer, type PM2).

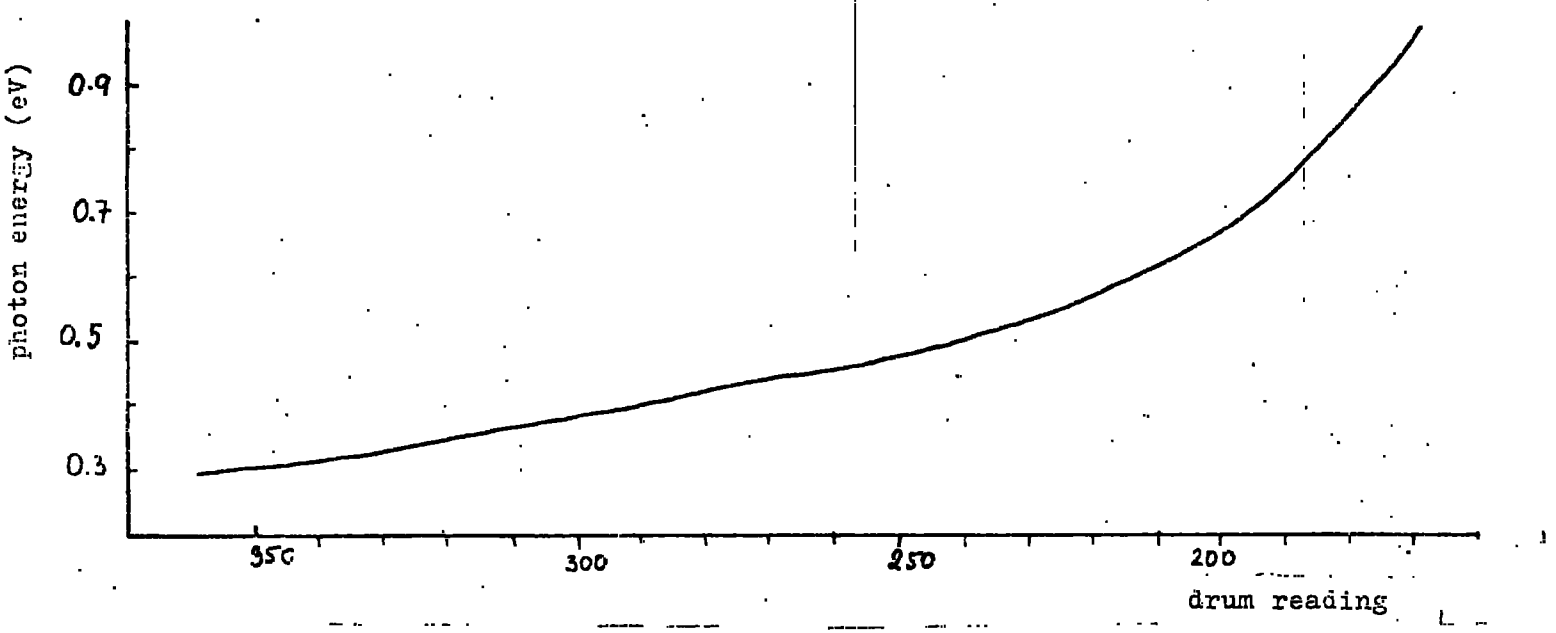

Fig.IV.6 Calibration curve of Spectrosil prism (contn'd)
(Grubb Parsons spectrometer, type PM2)

intensities , optical constants and normal incidence reflectivity were calculated as discussed in sections 4.2 and 4.1. The values of reflectivity obtained this way were then compared with those directly measured using the experimental set up which is shown on Fig IV.4.

4.4.2 Source of Radiation

A quartz iodine lamp operating at 12V, 100W was used as a radiation source. A stabilised d.c. power supply was used to eliminate fluctuation of power.

4.4.3 The Monochromator

A modified P.M.2. Grubb Parsons single prism monochromator was used with a 60° prism to produce monochromatic radiation for wavelengths up to 4μm. In the region of photon energies 0.3 - 3.0 eV a Spectrosil prism was used. The calibration curve for the Spectrosil prism is shown in Figs$\overline{\text{IV}}$5 and$\overline{\text{IV}}$6. Most of the measurements were made up to 4μm where cut off in transmission of Spectrosil A occurs.

The results of previous workers indicate that low temperature absorption bands of Rare Earths were rather broad (0.3eV). A resolving power of about 20 was considered adequate for the present work.

4.4.4 Detecting system

1) For the measurements in the visible and near infra-red region (4000 Å - 10000 Å) a sensitive SGD-100 photo-diode was used as a radiation receiver.

2) For measurements in the infra-red region a Grubb Parson's thermocouple detector with a KBr window was used. This detector was employed with a transformer to match the impedance of the thermocouple detector. A typical a.c. output on the secondary of the transformer was 100 μV.

The system of signal detection was differential. The radiation coming out of the radiation source was chopped by a 10Hz chopper. The

a.c. signal from the radiation detector corresponding to the radiation intensity passing through the optical system was then amplified using usual techniques of phase sensitive detection. The reference signal for the phase sensitive detector was generated at the chopper using a simple circuit with a phototransistor OCP71.

The a.c. output from the detector was amplified by a low noise amplifier (LNA) made by Brookdeal Electronics (type LA450). The amplifier had a variable band width (3 dB points) and for the operation at 10Hz the points were set at 1Hz and 100Hz. The maximum gain of 100 dB (x 10^5 voltage gain) was adjustable in 10 dB steps and with a fine continuous gain adjustment (from 0 to -12 dB). The input impedance of the LNA could be switched to 80kΩ, 100kΩ and 50MΩ. The output impedance was 100Ω.

From the above characteristics it is evident that the Brookdeal LA450 was quite adequate for the purpose. The phase sensitive detector used with LA450 in the early stages of the work was the Brookdeal detector type 401. At the last stages of the work a Solatron DVM d.c. digital voltmeter was used instead of a phase sensitive detector. The D.C. output voltage from the meter circuit of the LA 450 was taken to the input of the Solatron DVM. This arrangement decreased errors in reading the reflectance ratios due to fluctuations of the measured intensities by approximately 50%.

Special care was taken to obtain correct output signal variation with rotation of the analyzer. It was found important to use the type of analyzer which did not shift the transmitted beam during rotation. A similar problem may arise due to the spurious polarization of the detector. To eliminate these difficulties a polarizer with planes normal to the optical axis was used as an analyzer. To work out the allowance for the spurious detector polarization the radiation was

allowed to pass through the optical system using a prism without the metallic film and the variation of the detector signal with the rotation of the analyser gave the allowance of the detector polarization.

4.4.5. Specimen holder

Fig IV.2 and Fig IV 7 show the cryostat and a specimen holder used for the present polarimetric investigations of Rare Earth thin films. The optical constants were measured by internal reflection from the films deposited onto the base of a fused silica prism cut as indicated in Fig IV.8 to give an angle of incidence of 75°. The prism was placed on to the sample holder at the bottom of the cryostat. As inside reflection was used for the measurements it was necessary to avoid any spurious birefringence of the silica prism due to strain. The prism material was spectrosil (A-quality) specially selected as "strain free", and it was obtained from Thermal Syndicate Ltd., Wallsend, Newcastle-upon-Tyne. While placing the prism onto the sample holder, special care had to be taken not to clamp the prism. The prism was located in a deep groove and a very light spring kept the prism in the contact with the sample holder. The bottom part of the prism was slightly smeared with vacuum grease to get better thermal contact with the sample holder. Optical constants of the uncoated prism were measured both at ambient and low temperatures to be sure that no spurious effects are involved. Ellipsometric parameters ϱ and Δ of an uncoated prism should satisfy the following conditions

$$\varrho = 1$$

$$(1+\cos\Delta) = 2\sin^2\varphi \quad tg^2\varphi/(tg^2\varphi - \frac{1}{n_o^2}) \qquad \text{IV 11}$$

(n_o is refractive index of spectrosil, φ is angle of incidence)

as follows from equation IV.5. For prism polarizers this agreed for the measured Δ to within $\pm 0.1^{\circ}$ even at low temperatures showing that double refraction in the prism and the cryostat windows could be neglected. Low temperature cryostat windows were made of the same material as the prism.

Values of refractive index of spectrosil A used in equation IV.11. were obtained from the published Technical Data supplied by Thermal Syndicate.Ltd. The values in the visible range were checked by the author using a minimum deviation technique.

Considerable effort was made to obtain accurate prism location during the experiments since an error in ς and Δ could arise if the prism is placed so that the angle of incidence was different from 75°, due to the big dispersion of Spectrosil A in the infra-red region.

4.4.6. The Cryostat

The cryostat for helium temperatures was capable of working in the temperature range $4.2^{\circ}K$ to room temperature. The cryostat was made of three parts

a) the "double" glass dewar

b) the middle part

and c) cryostat cup.

a) The Glass part of the cryostat was made of Pyrex glass. The outer part served as a liquid nitrogen dewar and the inner part of the dewar was for liquid helium. The sample holder was attached to the bottom of the helium dewar with a glass-to-metal seal as shown in Fig IV.7. The inner parts of the dewar were silvered in order to protect the helium dewar from heating by radiation. The collar of the glass part was ground flat so that it made a vacuum fit on to the "O" ring junction with the metal part. In order to avoid any relative movement the dewar was tied to the middle part using a wooden collar with six screws.

b) The middle part was made of brass. There were vacuum leads through for the thermocouple placed in it. The brass part was fastened on to a massive steel stand with three legs resting on the ellipsometer table. The steel stand was made as massive as possible. The three steel

legs 1" in diameter were welded to the stand triangle as indicated on the Fig IV.2. The top of the helium cryostat was mounted onto the three steel rods which were screwed into the triangle of the steel stand.

c) The Cryostat cup, was made of brass and had an "O" ring to make a vacuum tight connection with the middle part. It had three windows for oblique incidence reflectivity measurements. The angle between the windows was 75°. The cup closed the working chamber which was evacuated through the flexible vacuum tube attached to the middle part of the cryostat. Typical vacuum inside the cryostat was 10^{-5} mm Hg.

4.4.7. Ellipsometer table.

This was made of three steel concentric discs with ball bearings in between and was designed so that no relative motion was possible between the discs. It was supported on three points to give adjustable height. The plane of the table was set parallel to the optical path by the use of a fine level. The cryostat was screwed on to the middle disc on which the scale for the angle of incidence was placed. The scale was big enough to read to an accuracy of $\pm$ 0.1° of arc.

4.4.8. Polarizers.

In the visible and infra-red ranges, Glan-Thomson prism polarizers were used. Below 0.5 eV selenium film polarizers were used similar to those described by Buijs (1960). Eight selenium films were mounted on a piece of 1.5 inch perspex tube at an angle of 25° to the axis of the tube. The efficiency of the polarizers was estimated from the minimum and maximum intensities when radiation was passed through polarizers. The estimated value was 0.995. The corrections for the unpolarized component were worked out from the measurements of the refractive index of an uncoated prism using the ellipsometer with selenium polarizers and using data for the refractive index of spectrosil A obtained from Thermal

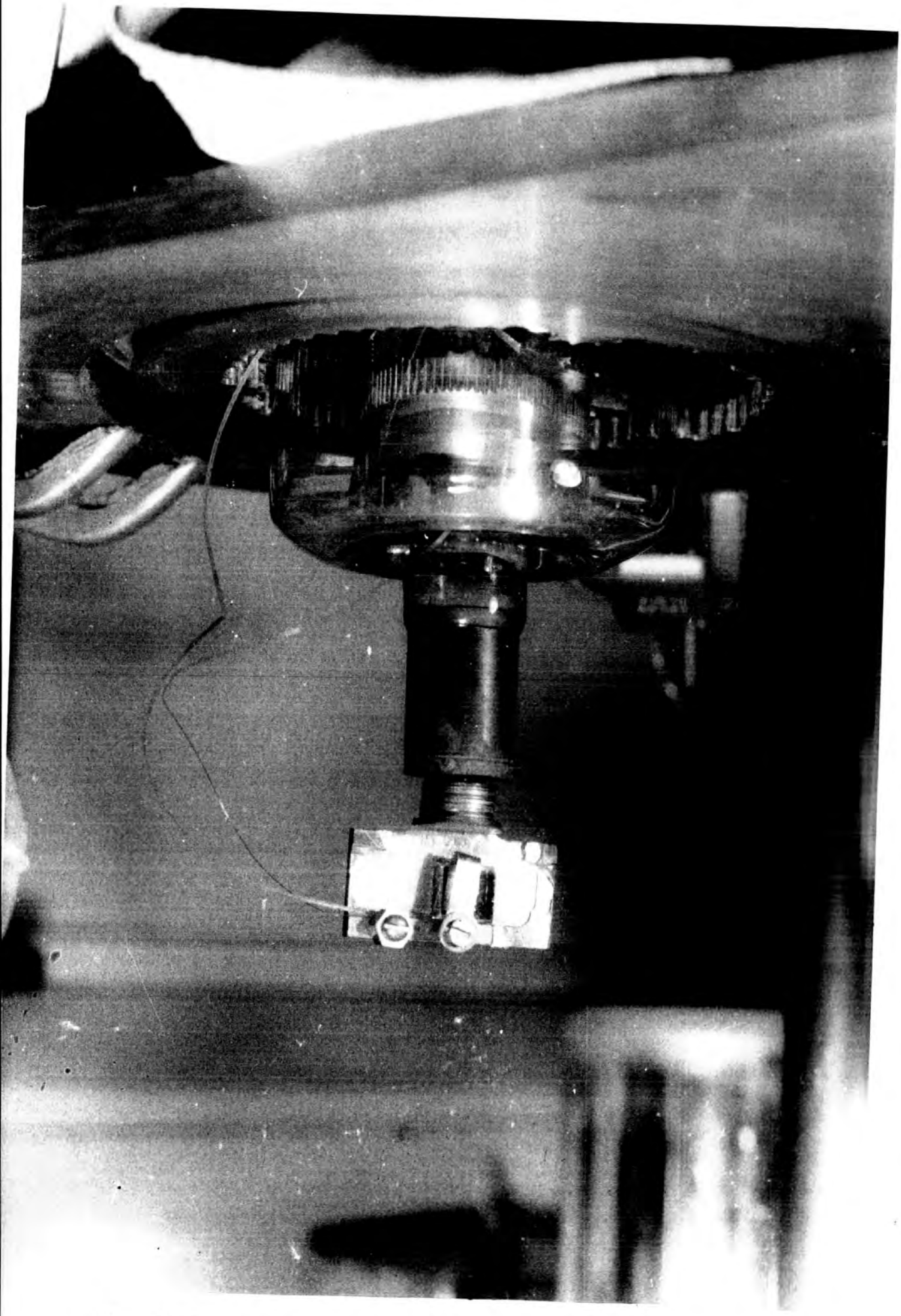

Fig.IV.7 Bottom of the cryostat with sample holder for ellipsometry.

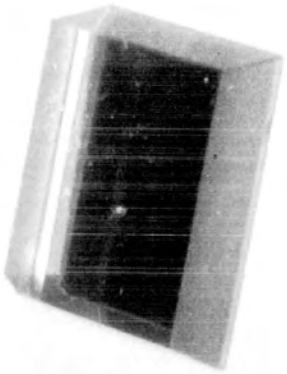

for ellipsometry

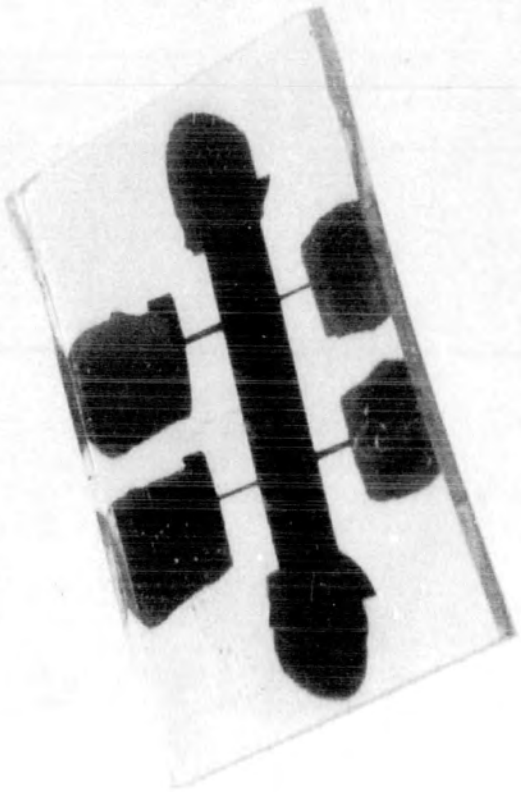

for 4point probe
resistivity measurments

Fig.IV.8 Samples.

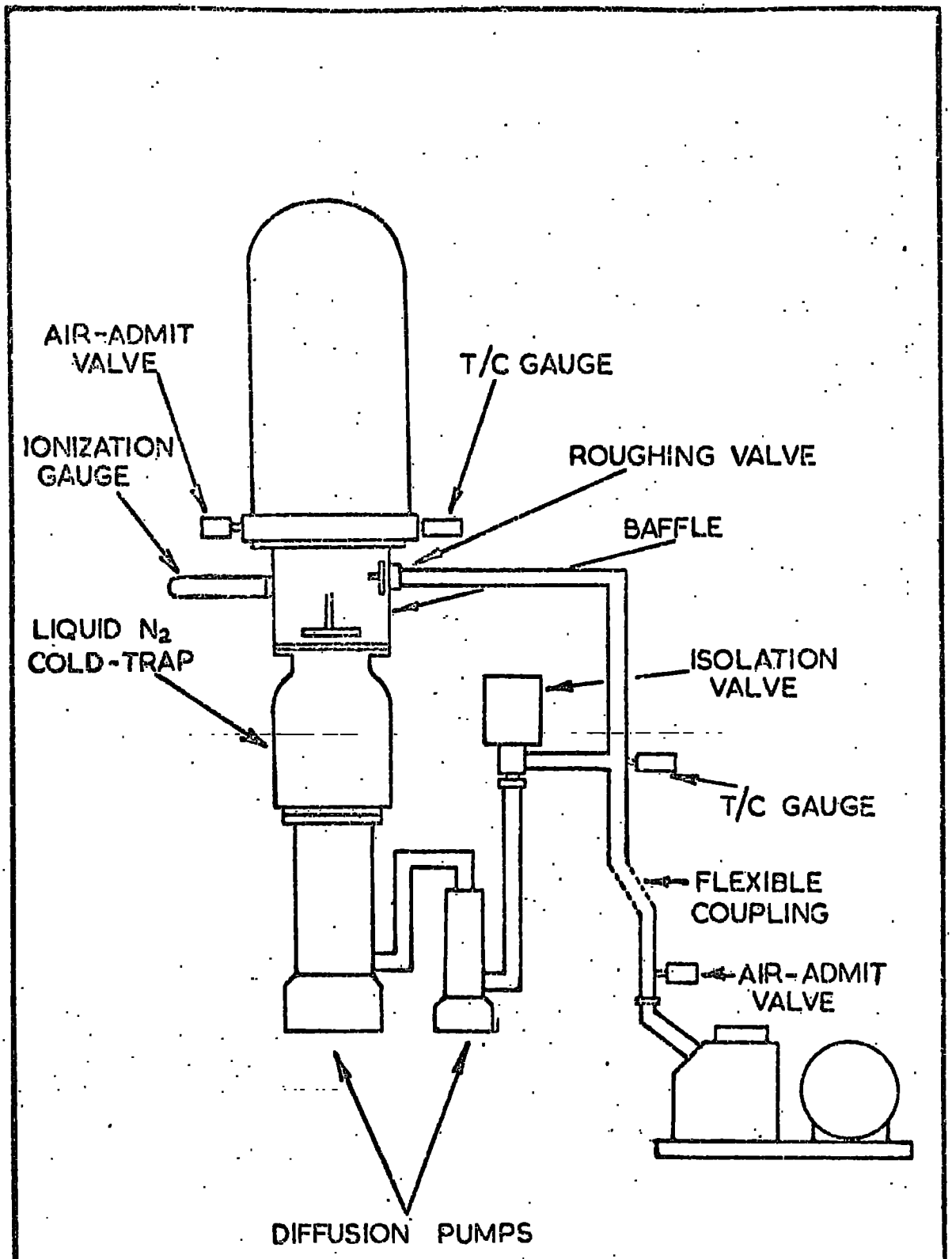

Fig. IV.9 The Vacuum System

Syndicate Ltd.

4.5. Thin Film Preparation.

The Rare Earth Metals have a high affinity for oxygen, even in the bulk form and since their melting points are only in the region of 1500°C it appears that fast evaporation in high vacuum will most efficiently reduce contamination by oxygen and water vapour.

a) The vacuum system used for the present work had a conventional layout employing two diffusion pumps in series, a rotary pump and a liquid nitrogen cold trap. The Pyrex bell jar closed the working chamber. There was also a small chamber attached to it where activated alumina was held to reduce contamination by oxygen and water molecules during the evaporation. The bell jar was baked out for eight hours before evaporation took place. The lowest pressure achieved in the chamber using the liquid nitrogen cold trap and bake out was 2.10^{-7} mm Hg. In order to achieve a lower pressure than 2.10^{-7} mm Hg a pre-evaporation of SiO and rare earth metals was used. This then gave the pressure of 10^{-7} mm Hg just before evaporation. The system is described in detail by Lodge (1969) (Fig. IV.9).

b) Substrates. Glass substrates 1" x ¾" x .032" were used primarily for the resistivity measurements. A fused silica prism and a silica glass plate were used for the optical measurements. The method of substrate cleaning adopted for the present work was a modification of the technique reported by F.M.K. Lodge (1969). It consisted of ultrasonic cleaning of the substrate in the 0.1% solution of Teepol in hot distilled water followed by ultrasonic cleaning in isopropylalcohol. Immediately after cleaning, the substrate was inserted in the substrate holder of the evaporation system and evacuation was commenced.

It is important to make the transfer as quickly as possible to reduce the density of small particles which set on the surface.

During the early stages of the pump down period to the working pressure the substrate was heated to approximately 200°C for eight hours by irradiation from a 250W quartz iodine lamp attached to the substrate holder to bake out residual absorbed gasses from the substrate.

c) The film evaporation. The Heavy Rare Earth metals in the form of small chips of purity 99.9% were supplied by Koch-Light Laboratories Ltd. The powder was evaporated by resistive heating of a tantalum boat of dimensions 4 cm x 1 cm x 0.01 cm. Neodymium and Ytterbium were evaporated in the form of very thin sheets cut from the bulk material in an Argon atmosphere. The bulk material of purity 99.9% was also supplied by Koch-Light Laboratories.

Prior to evaporation, the boats and their charges were thoroughly outgassed by passing a moderate current through them, insufficient to cause evaporation, but enough to drive off the residual gas. During this, the substrate was shielded from the source by a stainless steel shutter, which could be removed magnetically from outside of the system. In order to assist the aggregation of the film, the substrate temperature was allowed to regain the ambient room temperature. Then the source was slowly brought up to the melting point of the evaporant. When melting occurred, the shutter was opened, the power was sharply raised and the source material was evaporated in four seconds. The temperature of the substrate usually rose to approximately 70°C, owing to radiation from the source. When evaporation was completed, the power was at once transferred to the boat containing outgassed SiO and the metal film was over-deposited by a protective layer of SiO. Following this, the film was annealed at about 300°C in high vacuum (1.10^{-7} mm Hg) for 20 minutes before being left to return

to ambient temperature while under vacuum. This is similar to the annealing procedure used by Schüler (1963) to reduce the residual resistivity of thin films due to strain. Three films were grown during every evaporation as discussed above.

The thickness of the film was estimated from the weight of the metal evaporated from the boat as discussed by Lodge (1969). In later stages it was measured by an interferometric microscope.

CHAPTER V

RESULTS

5.1 Introduction

Using the method described in Chapter IV, the optical characteristics have been determined for thin films of the heavy rare earth elements, gadolinium, terbium, dysprosium, holmium, erbium and ytterbium and for the light element neodymium. The measurements were carried out at a number of temperatures between 4.2 and 300°K. In the following, the detailed variations of the optical conductivity $\sigma(\omega)$ and the real part of the dielectric constant $\varepsilon_1(\omega)$ with both the incident photon energy and sample temperature are given element by element, the discussion being reserved in toto for Chapter VI.

Before giving these results however, it is necessary to make the following points.

a) The previous results of Lodge (1969), and Schüler (1963) on films prepared in a similar way to those presently under investigation, which involved electrical conductivity and magnetoresistance showed that these properties are very similar to those of polycrystalline material. In view of this we assume similarly to Hodgson and Cleyet (1969) that the reported values of $\sigma(\omega)$ and $\varepsilon_1(\omega)$ are averaged values taken over all lattice directions.

b) Since the grain size is very much smaller than the diameter of the incident beam, and the films are not magnetized, then it can be anticipated that the Kerr effect plays no part in the form of the results.

c) The gap in the observations near to $\lambda = 2.7\mu m$ occurs as a result of the absorption of the spectrosil A substrates at that wavelength. The absorption curve for the material used for the substrates is shown in Fig V.1.

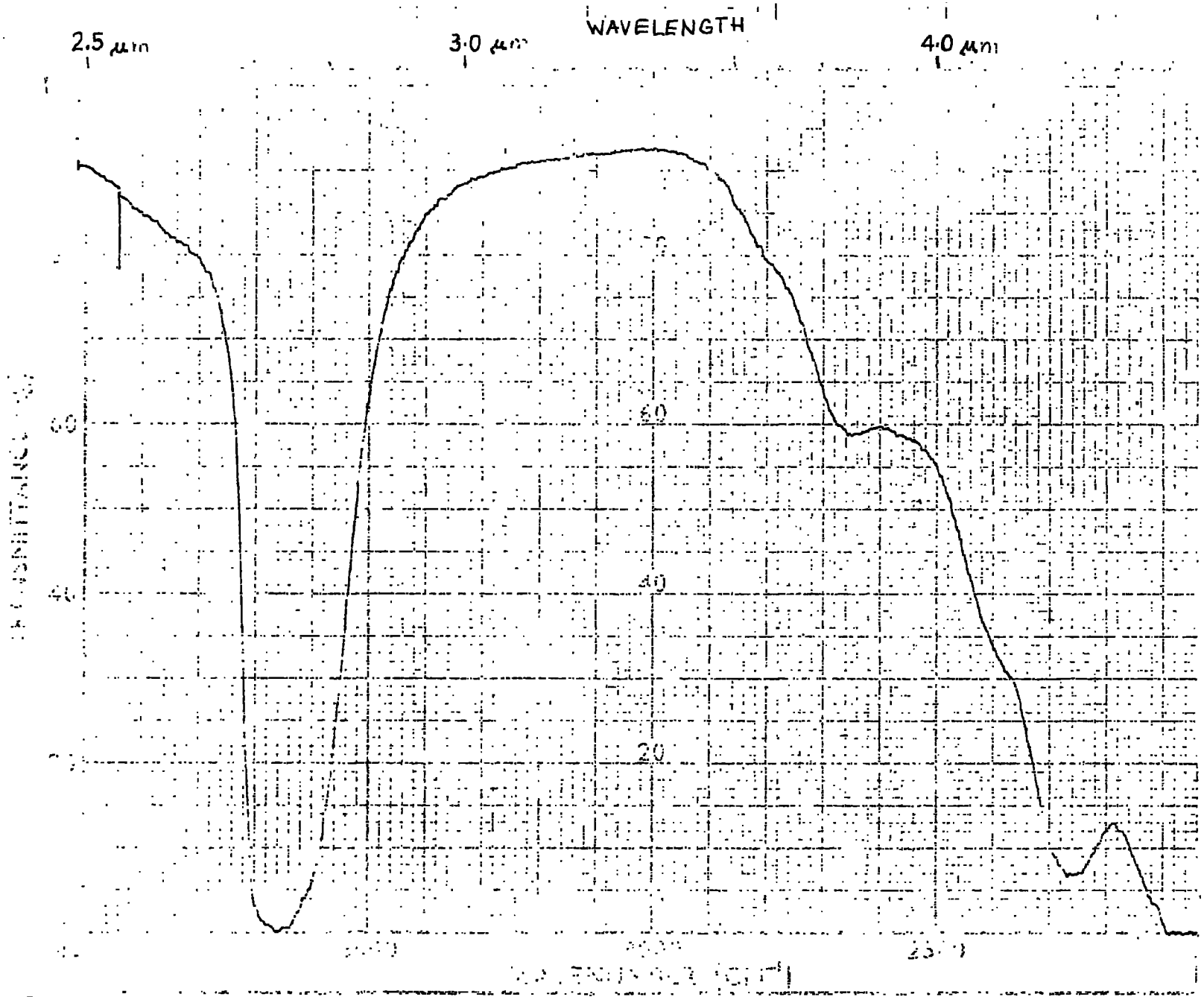

Fig VI

Fused Silica
THERMAL SINDICATE Ltd

d) Experimental errors

Random error in the determination of $\sigma(\omega)$ and $\varepsilon_1(\omega)$ by ellipsometry was due to fluctuations of the detected intensities. For photon energies above 0.5 eV the random fluctuation of the intensities $\frac{\delta I}{I}$ was less than $\frac{1}{300}$ giving the random errors in $\sigma(\omega)$ and $\varepsilon_1(\omega)$ as

$$\frac{\delta\sigma(\omega)}{\sigma(\omega)} \leqq \pm 1\% \quad ; \quad \frac{\delta\varepsilon_1}{\varepsilon_1} \leq \pm 4\% \text{ provided } \quad |\varepsilon_1| \geq 0.4.$$

The relative error in ε_1 rapidly increases as ε_1 goes to zero. For photon energies below 0.5 eV the intensity fluctuations $\frac{\delta I}{I}$ were less than 1% and the random error increased accordingly, i.e.

$$\frac{\delta\sigma(\omega)}{\sigma(\omega)} < \pm 3\% \quad ; \quad \frac{\delta\varepsilon_1}{\varepsilon_1} \leqq 12\% \text{ provided } \quad |\varepsilon_1| \geqq 0.4 \quad .$$

For any set of readings there was a factor constant in σ and ε_1 which did not exceed $\pm$ 1.6% due to the limitation on the accuracy with which the angle of incidence could be set. This did not, of course, affect the observation of structure in the curves of optical conductivity against photon energy. The errors due to the settings of zero azimuths were small with respect to the random error.

The variations of absolute values of $\sigma(\omega)$ and $\varepsilon_1(\omega)$ from film to film are discussed in the following sections.

5.2 Gadolinium

Fig V 2 shows the values of $\sigma(\omega)$ and $\varepsilon_1(\omega)$ for the photon energy ($\hbar\omega$) range from 0.50 eV to 2.5 eV at temperatures of 300°K, 90°K and 50°K. Limited measurements were also made up to $\hbar\omega = 5$ eV by observations of the transmission through very thin films (~600Å). The only significant structure observed in this extended range occurred near to 5 eV, but the resolution of the system in this region was very poor. The changes in reflectivity caused by magnetic ordering at low temperatures were evaluated from the results of Fig V.2 using equation D.14 and are shown in Fig V.3. The form of these changes agrees very closely with those derived in a similar way by Hodgson and Cleyet (1969) and those observed by direct measurement of reflectivity by Schüler (1965). The absolute values of $\sigma(\omega)$ and $\varepsilon_1(\omega)$ differ by only a few percent from those of Hodgson. This difference is well within the limits of error discussed below.

The absolute values of both $\sigma(\omega)$ and $\varepsilon_1(\omega)$ varied from film to film by ± 7.0%, depending on the ultimate evaporation pressure, the annealing procedure, the evaporation rate and so on. The basic form of their energy dependence, however, remained unchanged.

The room temperature results, corresponding to the paramagnetic phase of gadolinium, show only the rapid changes in $\sigma(\omega)$ and $\varepsilon_1(\omega)$ at low energies which are to be expected from the Drude contribution to the optical properties, and a broad peak in $\sigma(\omega)$ centred at $\hbar\omega = 2.0$ eV which is undoubtedly associated with the many possible interband transitions in the material. On cooling there is no sudden change in the form of the curve at the magnetic transition temperature, rather the minimum in $\sigma(\omega)$ near to $\hbar\omega = 0.7$ eV gradually becomes shallower and finally develops into the peak at 0.7 eV. This is in agreement with the results of earlier workers, although the low temperature peak reported by Hodgson at 1.1 eV was not

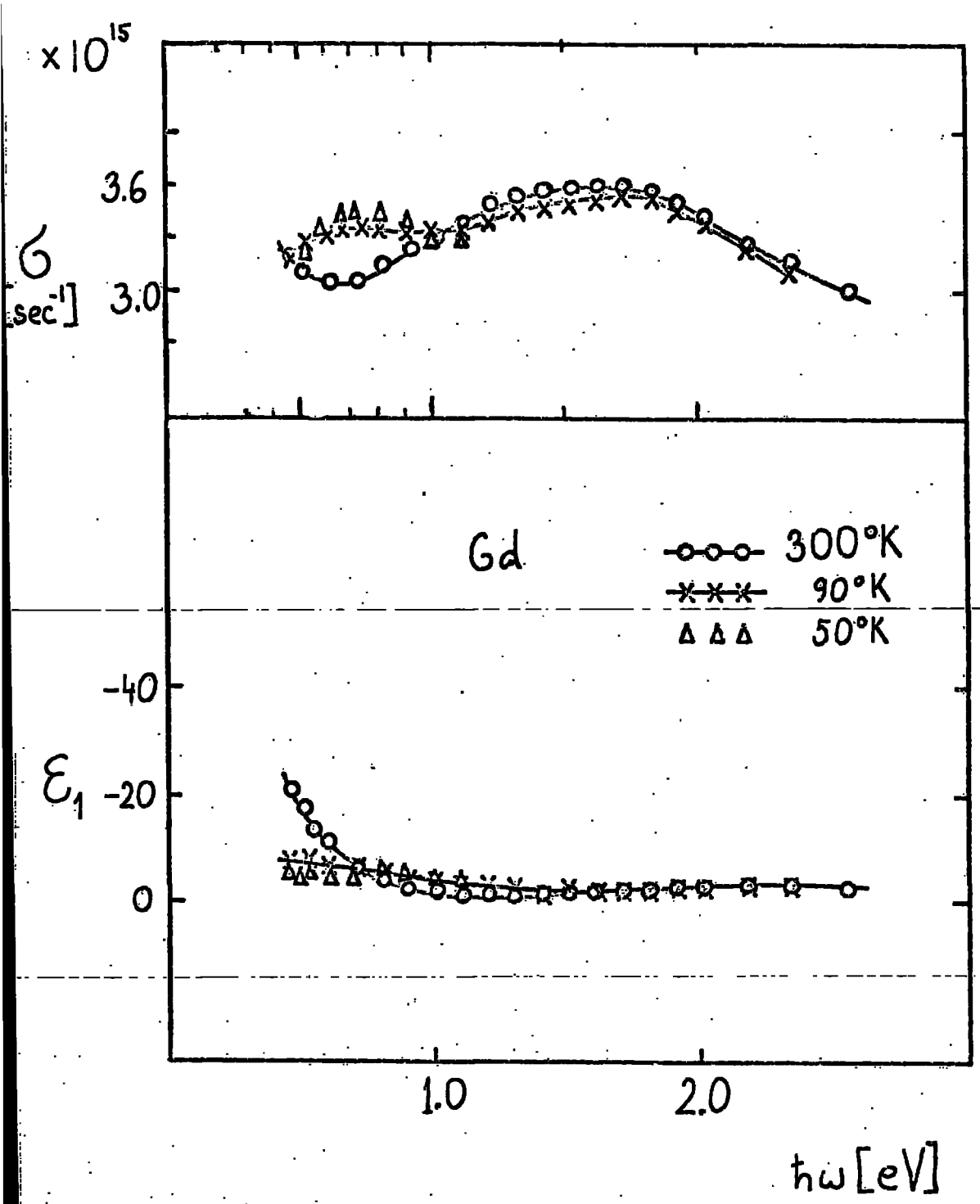

Fig.V.2 Optical conductivity $\sigma(\omega)$ and dielectric constant $\varepsilon_1(\omega)$ of Gd films at temperatures shown. $\hbar\omega$ is the photon energy. ($\sigma(\omega)=nk\omega/2\pi$; $\varepsilon_1=n^2-k^2$; n,k are optical constants)

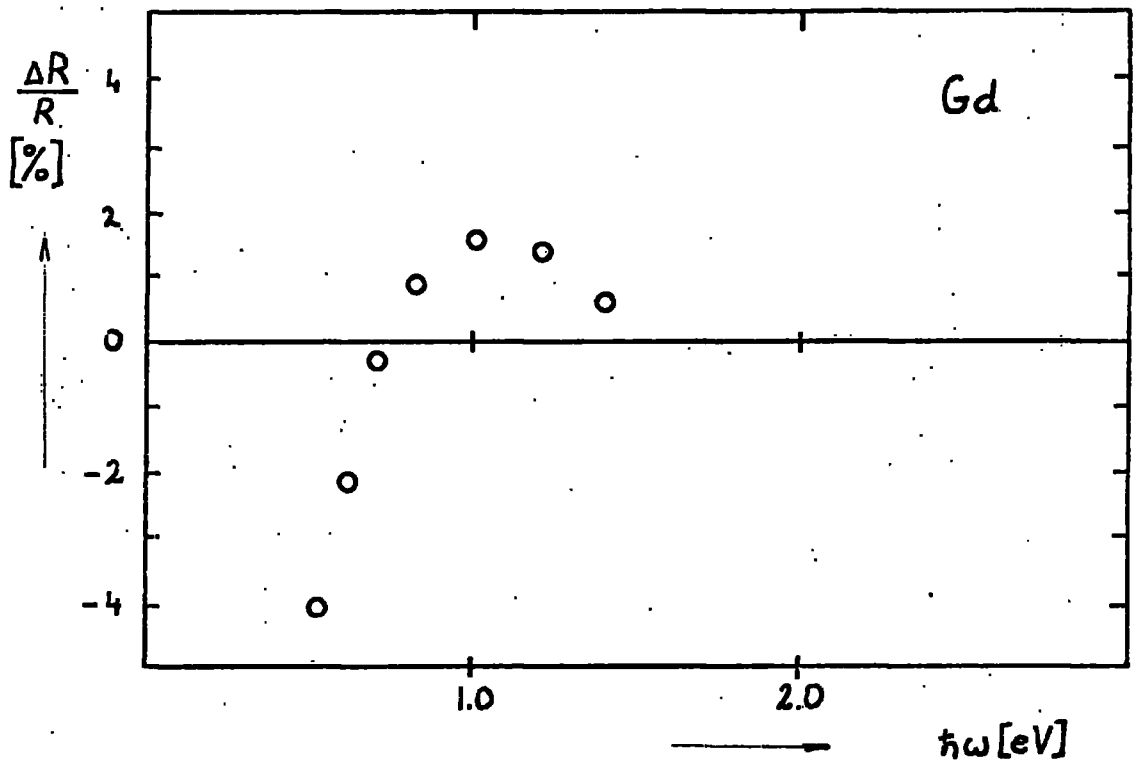

Fig.V.3. Fractional change of reflectivity on cooling of Gd films from 300°K to 90°K as calculated from data on Fig.V.2.

observed in any of the specimens used in this investigation.

5.3 Terbium

The frequency dependence of $\sigma(\omega)$ and $\varepsilon_1(\omega)$ for this metal at 300°K, 77°K and 20°K are shown in Fig V.4 over the range $\hbar\omega$ = 0.33 eV - 2.5 eV. In the paramagnetic region the form of the results is similar to those of gadolinium and again no drastic changes are found as the temperature is decreased through the two ordering temperatures. The optical conductivity $\sigma(\omega)$ increases gradually in the vicinity of the minimum (near to 0.7 eV) as the temperature is lowered and decreases above 1 eV. At liquid nitrogen temperatures this increase may perhaps be resolved into a double peak, with maxima at 0.7 eV and 0.56 eV. On further cooling to 20°K an unexpected rise with respect to the 77°K curve appears at about 0.5 eV.

The changes in $\sigma(\omega)$ caused by reducing the temperature, and presumably therefore arising as the result of magnetic ordering are shown in Fig V.6 in which these low energy peaks are clearly visible. Also from this figure it is evident that between 1 and 1.5 eV the total value of $\sigma(\omega)$ decreases on ordering, an effect which one must assume is related to the increase in $\sigma(\omega)$ at lower energies.

The calculated variation of the fractional reflectivity change on cooling to 77°K and 20°K ($\frac{\Delta R}{R} = \frac{R(300°K) - R(T)}{R(300°K)}$) is shown in Fig V.5, the values being derived from the data of Fig V.4. Also shown in this figure is the measured $\Delta R/R$ value obtained directly using normal incidence reflectivity observations. The directly measured absolute values of $\frac{\Delta R}{R}$ suffer from the systematic errors which arise because of the sample holder design which was inadequate to obtain values of $\frac{\Delta R}{R}(\omega)$ to be better than $\pm$ 3% accuracy. On the other hand the slope of the curve $\Delta R/R$ is quite meaningful and provides a qualitative comparison with that calculated from results in Fig V.5.

Again the form of the basic results (Fig V.4) are similar to those obtained independently by Hodgson, to whom I am indebted for his kindness in allowing me to see his data before publication. Minor differences exist however, in that at high energies Hodgson's peak in $\sigma(\omega)$ occurs at 1.6 eV compared to 1.9 eV in Fig V.4, and at low temperatureshe did not observe any peak near to $\hbar\omega = 0.55$ eV. Because of this difference at low energies the measurements were repeated several times on a series of different films and in all cases it was possible to detect some structure in this region.

The form of the results is very different from those of Pétrakian (1972) particularly at high photon energies as shown in Fig V.7. His measurements were carried out on extremely thin films evaporated in situ. Pétrakian's results for the other metals are also different from those of Hodgson et.al. (1969) and Schüler (1965) and also differ from those described in this thesis. He attributes these differences to the effects of oxidation in previous results.

In order to establish whether this was justifiable, or whether at the film thicknesses used by Pétrakian the electronic structure of the metal is fundamentally different from the "bulk-like" films used by Hodgson, Schüler and myself, measurements were made on deliberately oxidized films. The results of these measurements which were made on unprotected films heated in air at 900°K for various times are shown in Fig V.7. The resulting change in $\sigma(\omega)$ caused by the oxidation leads to results which are similar to those of Pétrakian. It should be remembered however, that since we are observing reflection at the inside face, the result of oxidation is to cause an effective decrease in the thickness of the metallic portion of the film. We must conclude therefore that the differences between the two different sets of results are not due to the

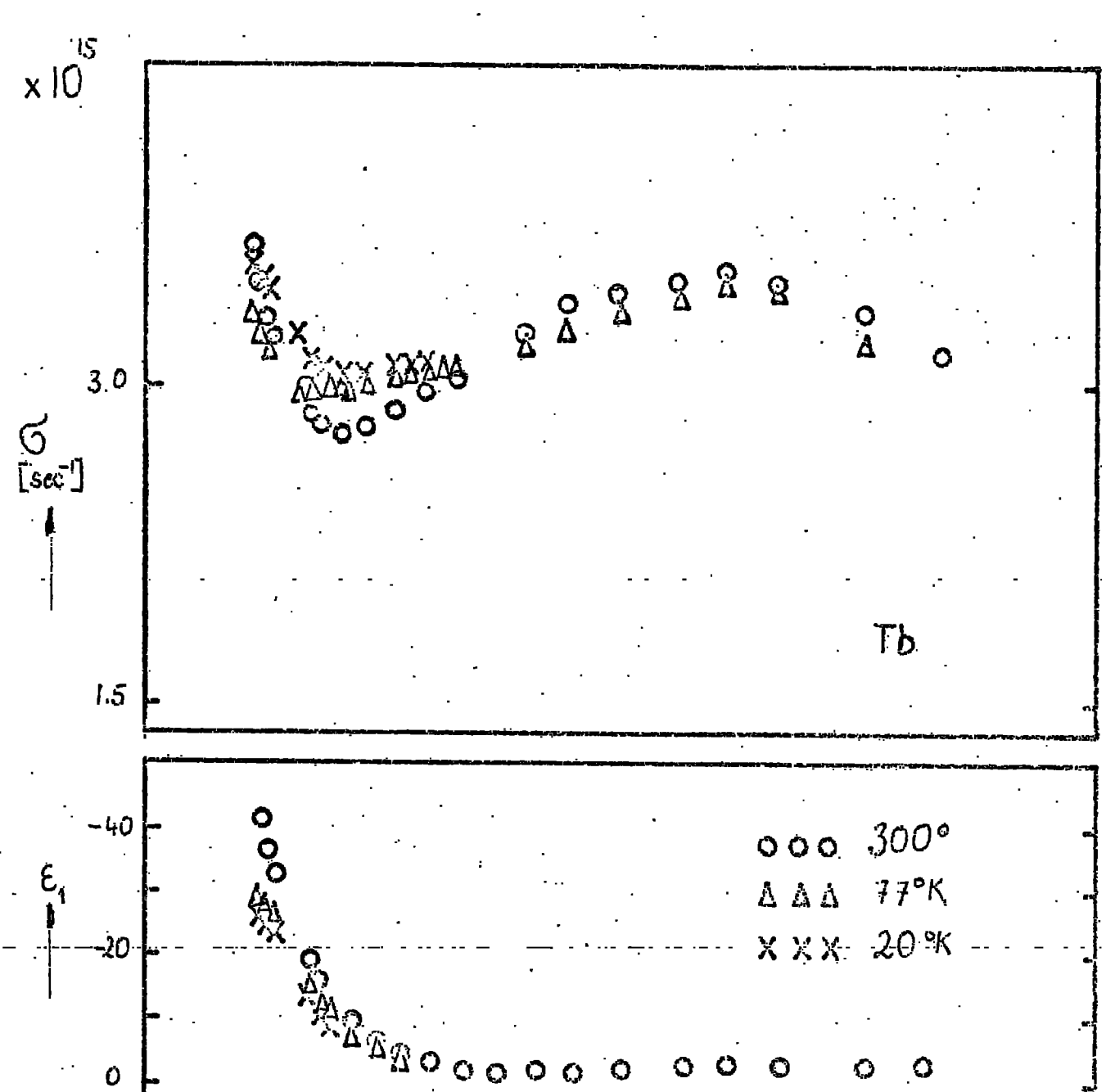

Fig.V.4 Optical conductivity $\sigma(\omega)$ and dielectric constant $\varepsilon_1(\omega)$ of Tb films at temperatures shown. $\hbar\omega$ is the photon energy. ($\sigma(\omega)=nk\omega/2\pi$; $\varepsilon_1=n^2-k^2$; n,k are optical constants)

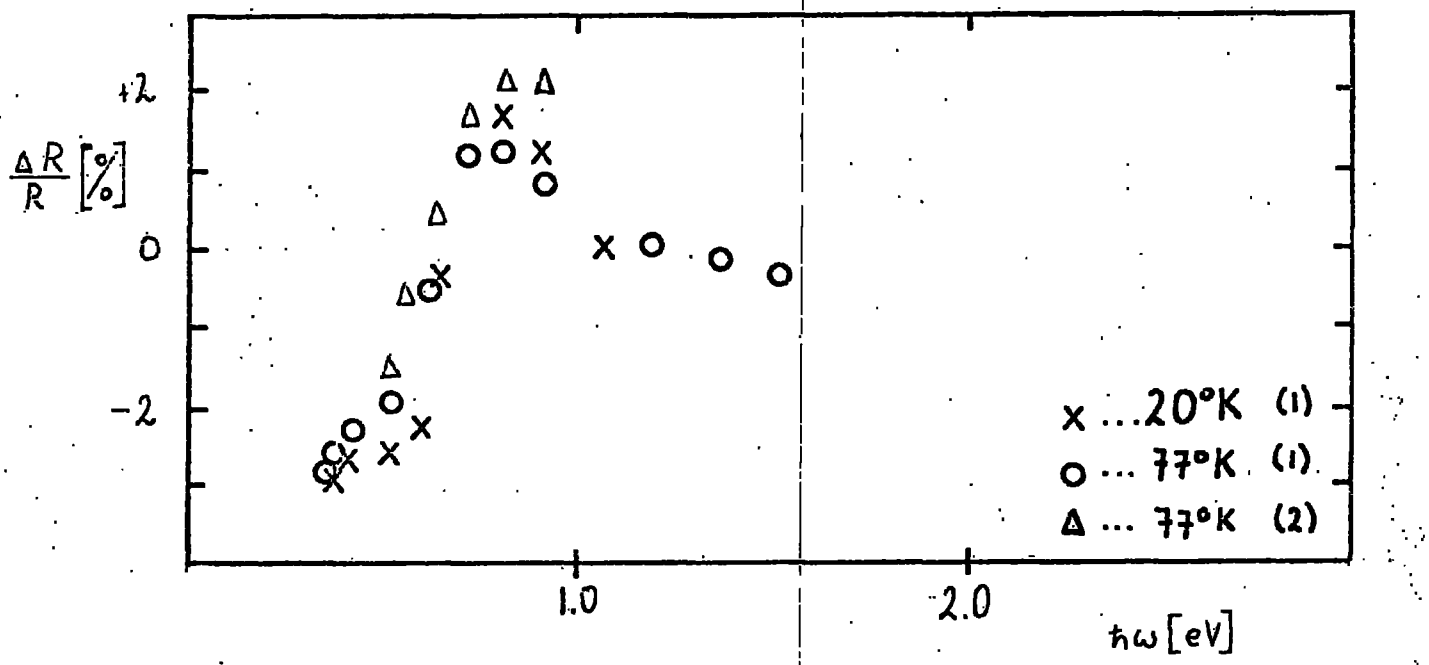

Fig.V.5. Fractional change of reflectivity $\Delta R/R$ = $=(-R(T)+R(300^{\circ}K))/R(300^{\circ}K)$ of Tb films on cooling to temperatures shown, (1) derived from the data on Fig.V.4;

(2) directly measured.

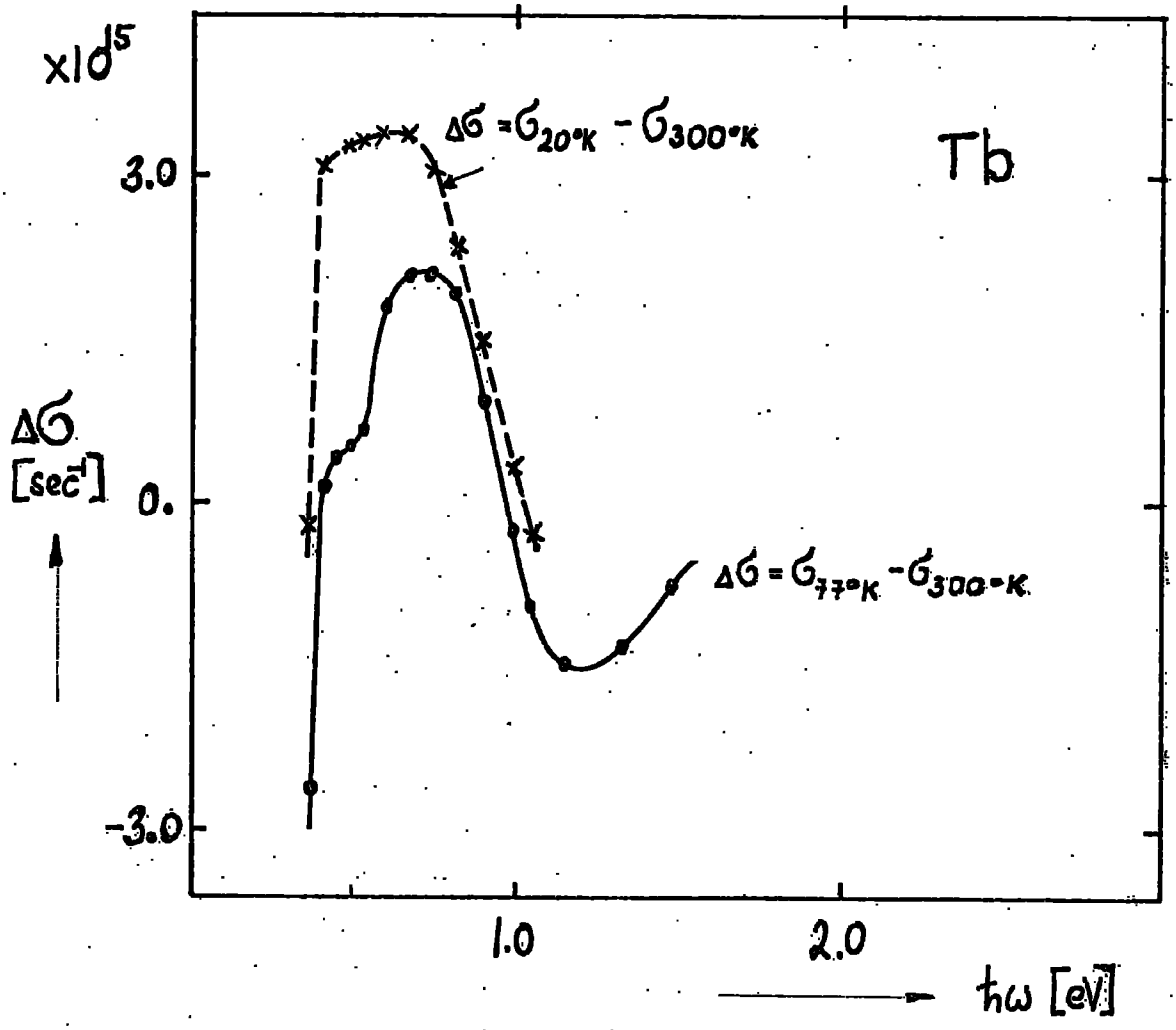

Fig.V.6. Changes in optical conductivity of Tb films on cooling to temperatures shown (derived from the data on Fig.V.4.)

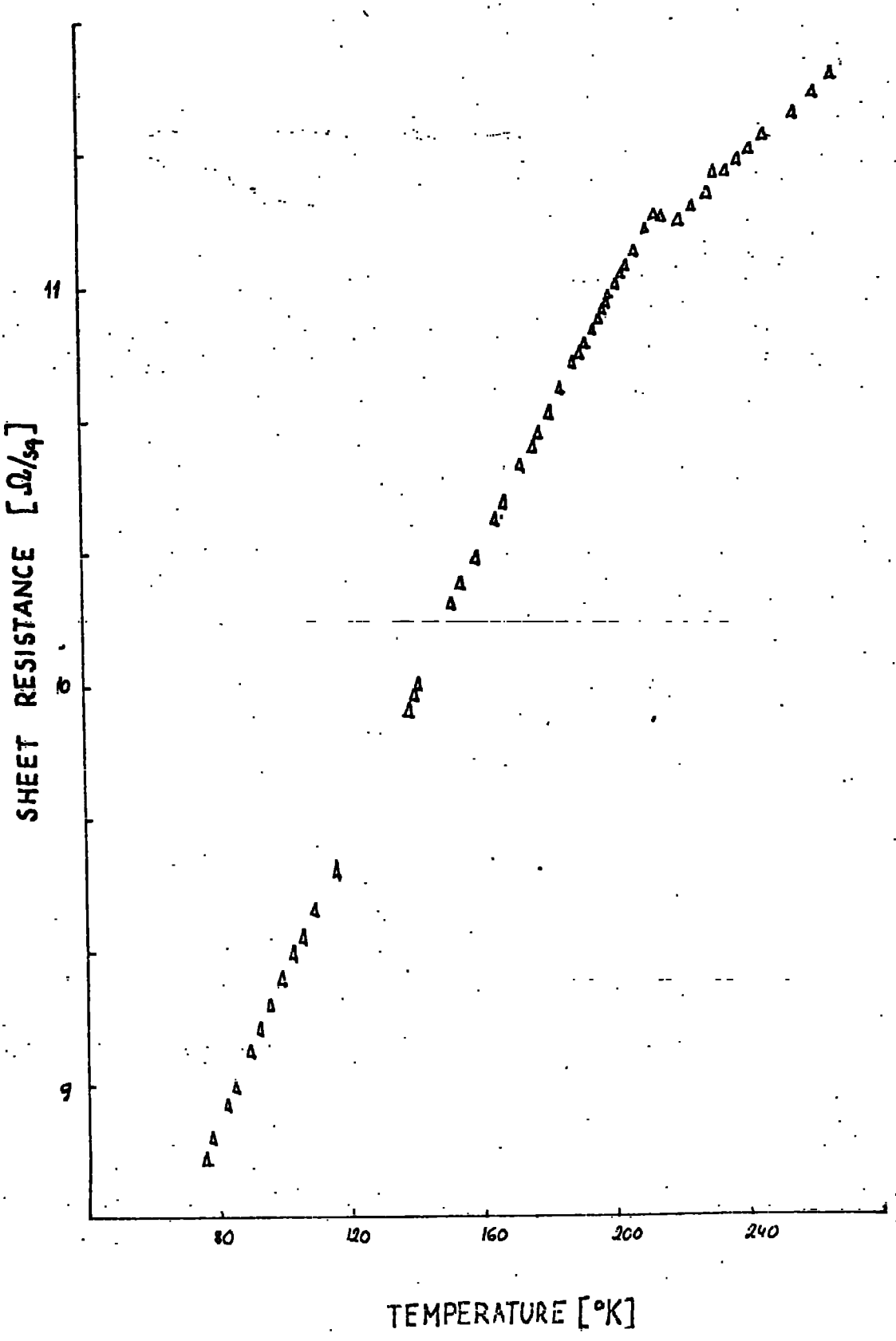

Fig.V.6a Temperature variation of sheet resistance of Tb films.

oxidation of the samples presently under investigation. It is possible however, that the presence of oxide in the very thin film samples of Pétrakian could lead to the observed differences, although in view of the very good vacuum conditions he used on evaporation it would seem more likely that the differences occur as the result of changes in the detailed electronic structure caused by the small thickness dimension in his films.

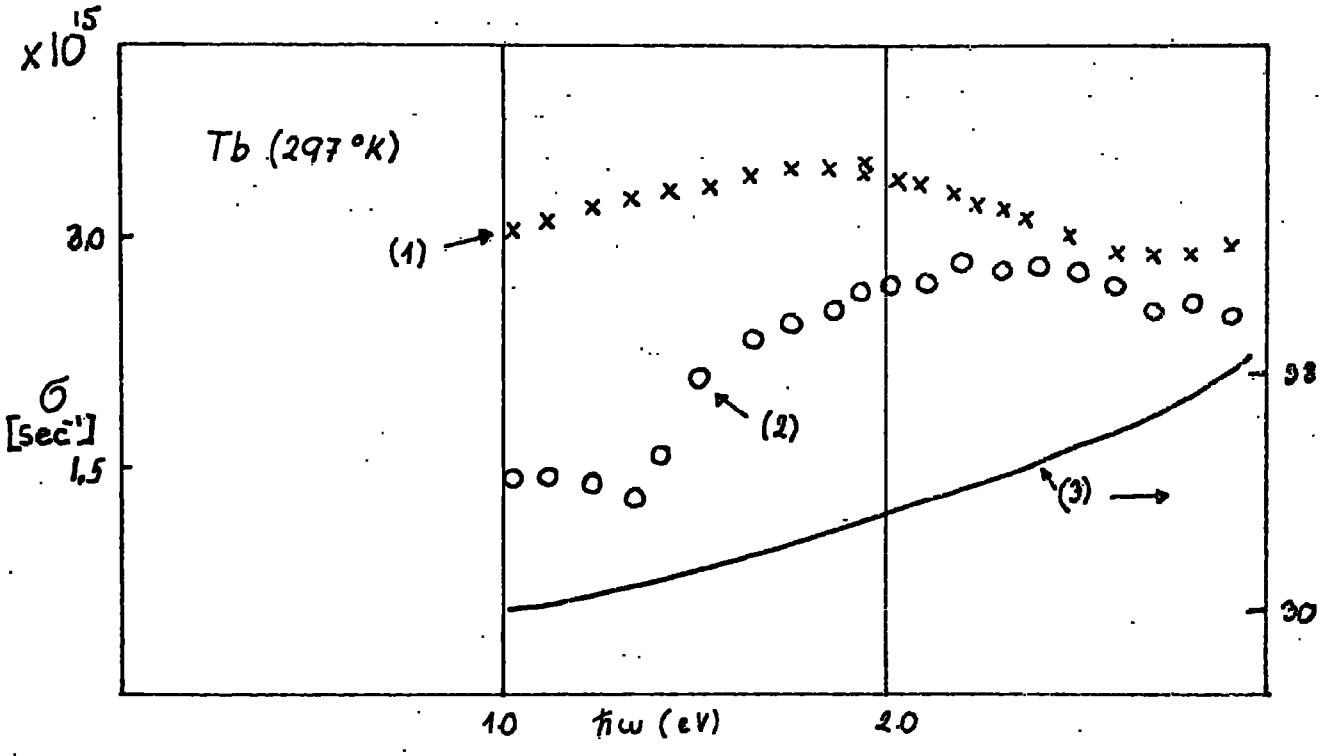

Fig V.7 Comparison of optical constants of Tb film after evaporation (1) and oxidized by heating at 600°C in air (2). Typical data for heavy rare earths obtained by Petrakian (3) (in arbitrary units)

5.4. Dysprosium

Fig V.8 shows the photon energy dependence of $\sigma(\omega)$ and $\varepsilon_1(\omega)$ at room temperature, 97°K and 50°K, corresponding to the para-, antiferro-, and ferromagnetic phases of dysprosium. There is a very slight structure in $\Delta\sigma(\omega) = \sigma_{97^\circ K}(\omega) - \sigma_{300^\circ K}(\omega)$ near to 0.4 eV, which is in agreement with the anomaly in the normal incidence reflectivity measurements reported by Schüler (1965). A comparison of the energy dependence

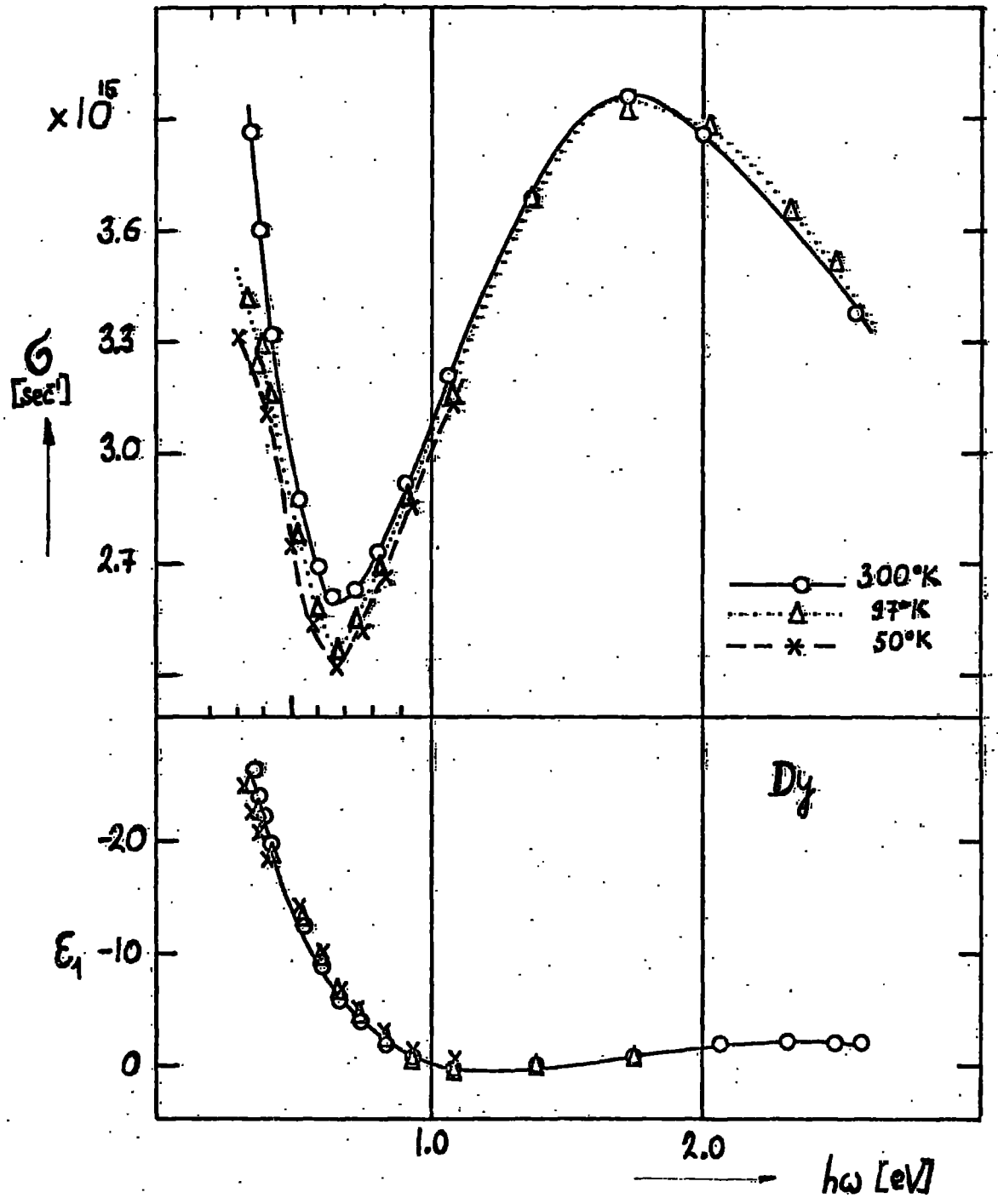

Fig.V.8 Optical conductivity $\sigma(\omega)$ and dielectric constant $\varepsilon_1(\omega)$ of Dy films at temperatures shown. $\hbar\omega$ is the photon energy. ($\sigma(\omega)=nk\omega/2\pi$; $\varepsilon_1=n^2-k^2$; n,k are optical constants)

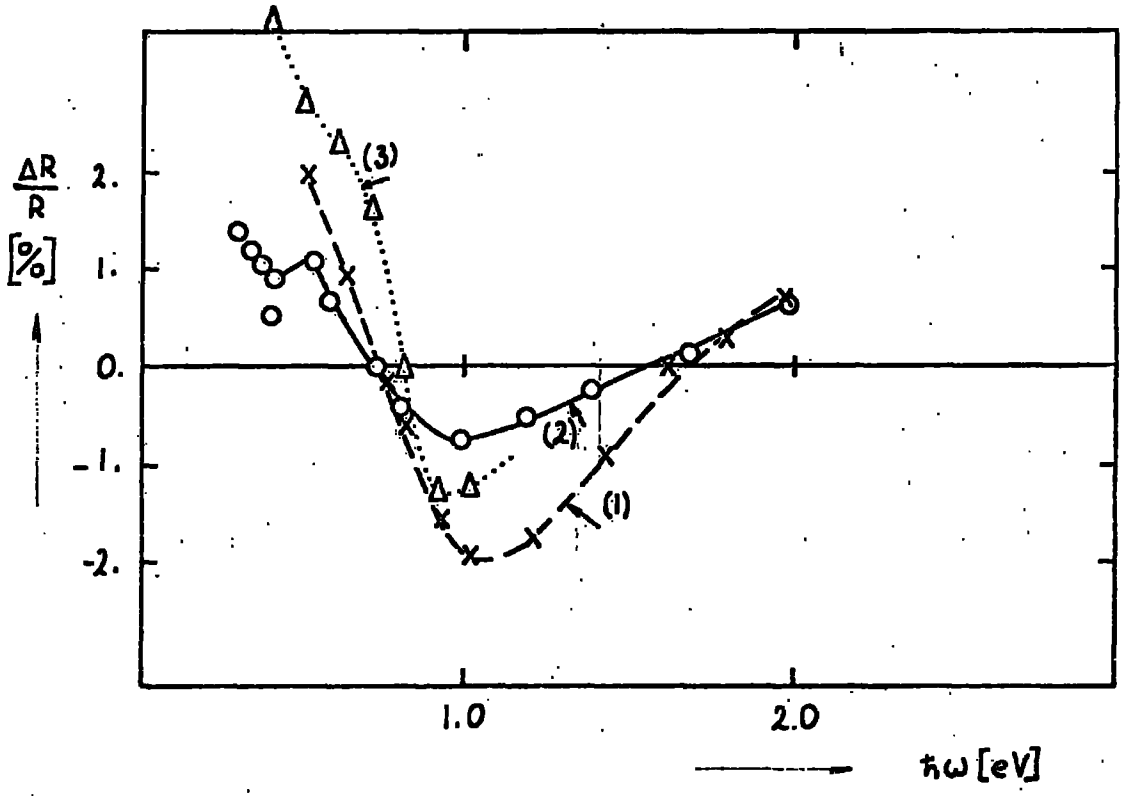

Fig.V.9. Fractional change of reflectivity of Dy films caused by cooling from 300°K to 95°K. (1) directly measured, (2) calculated from data in Fig.V.8, (3) obtained by Shüler (1965).

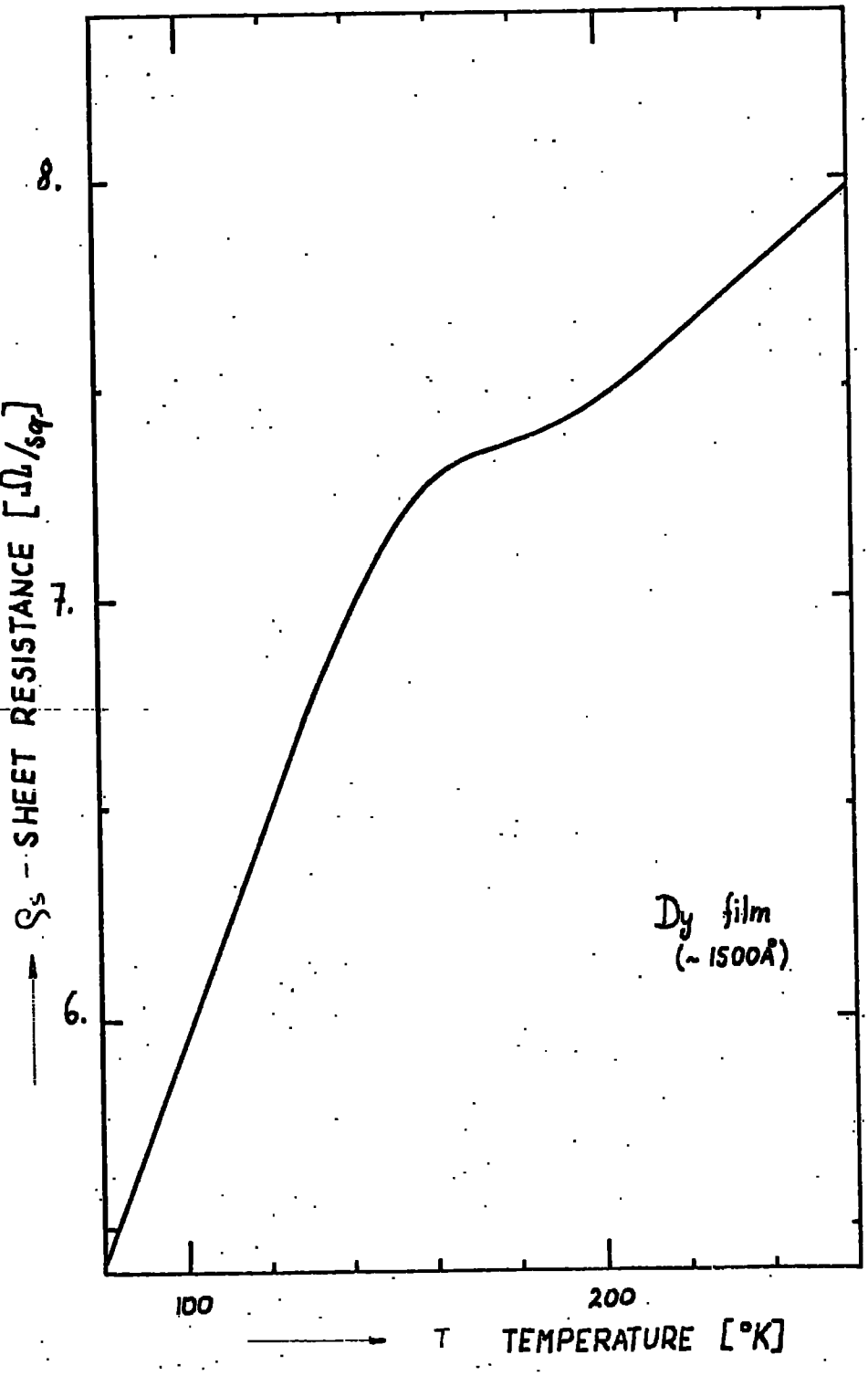

Fig.V.10 Temperature variation of sheet resistance of Dy films.

of the reflectivity derived from these ellipsometric measurements with the direct measurements of Schüler is shown in Fig V.9 from which it may be seen that these are in reasonable agreement.

Resistivity measurements were also made on dysprosium films, the results for one of which are shown in Fig V.10. The form of the curve $\rho_s(T)$ was reproducible but the residual resistivity was strongly dependent upon the method of preparation. The minimum residual contribution was found for films that had been annealed for 45 min. immediately after evaporation. The $\rho_s(T)$ curve clearly shows magnetic transitions at the Néel point ($180^{\circ}K$).

A similar dependence on the preparation procedure was found in measurements of the optical properties, the form of the curves describing both $\sigma(\omega)$ and $\varepsilon_1(\omega)$ and the absolute values of these quantities appeared to be much more sensitive to the substrate temperature during evaporation than did any of the other heavy rare earth metals.

In order to obtain reproducible low temperature changes $\Delta\sigma(\omega)$ and $\Delta\varepsilon_1(\omega)$ it was necessary to evaporate with the substrate at room temperature. In one instance it was found that a change in substrate temperature from $440^{\circ}K$ to $300^{\circ}K$ resulted in a reversal of sign of $\Delta\varepsilon_1(\omega)$ at low temperatures even though the $\sigma(\omega)$ dependences appeared identical.

An attempt was made to detect the Kerr-effect in the anti-ferromagnetic range where the critical field necessary to induce ferromagnetic ordering in dysprosium is quite low. The applied field was produced using a Helmholtz coil system with the field parallel to the film plane. No changes were observed within the sensitivity limit of the apparatus (intensity change $10^{-2}\%$). Further, no changes (to within 0.01%) were detected in the reflectivity at $90^{\circ}K$ using a.c. fields of 1kOe (rms) in conjunction with a phase sensitive detection system. These negative results appear to confirm the findings of Cooper and Reddington (1965).

Both transmission and ellipsometry measurements were carried out between 3 eV and 5 eV, but there was no evidence of any structure in either $\sigma_1(\omega)$ or $\varepsilon_1(\omega)$ dependence in this range.

5.5 Holmium

Fig V.11 shows the energy dependence of $\sigma(\omega)$ and $\varepsilon_1(\omega)$ at room temperature, 97°K and 20°K. There is an evident structure in $\sigma(\omega)$ at 20°K below 0.35 eV. This structure is comparable with the structure observed by Schüler (1963) in infra-red reflectivity of Holmium thin films below the Néel point (120°K). The fractional changes in the reflectivity $\frac{\Delta R}{R}$ on cooling to 20°K as calculated from the data on Fig V.11 are shown on Fig V.11 . The changes in the optical properties again occurred gradually on cooling showing no drastic behaviour at the Curie temperature (56°K).

This is very similar to what has been already mentioned above for Gd, Tb and Dy. If we compare the values of $\frac{\Delta R}{R}$ (Fig V.11b) calculated from the ellipsometric data with those directly obtained by Schüler we notice only a qualitative agreement. This would probably be caused by the limitations imposed by the polarizer in the far infra-red region between 0.33 eV and 0.44 eV to obtain absolute values of optical constants from which $\frac{\Delta R}{R}$ is calculated. $\frac{\Delta R}{R}$ therefore suffers quite a large systematic error even though changes $\Delta\sigma(\omega)$ in optical conductivity were quite consistent in that region. (Fig V.11a).

5.6 Erbium

The optical constants of Erbium films obtained by the present method are shown on Fig V.12. The room temperature data for Er show a behaviour which is characteristic of the rest of the heavy elements from Gd to Ho. At 20°K, which is below the paramagnetic Curie point of bulk material (85°K), a new peak in $\sigma(\omega)$ at 0.38 eV appears which is accompanied

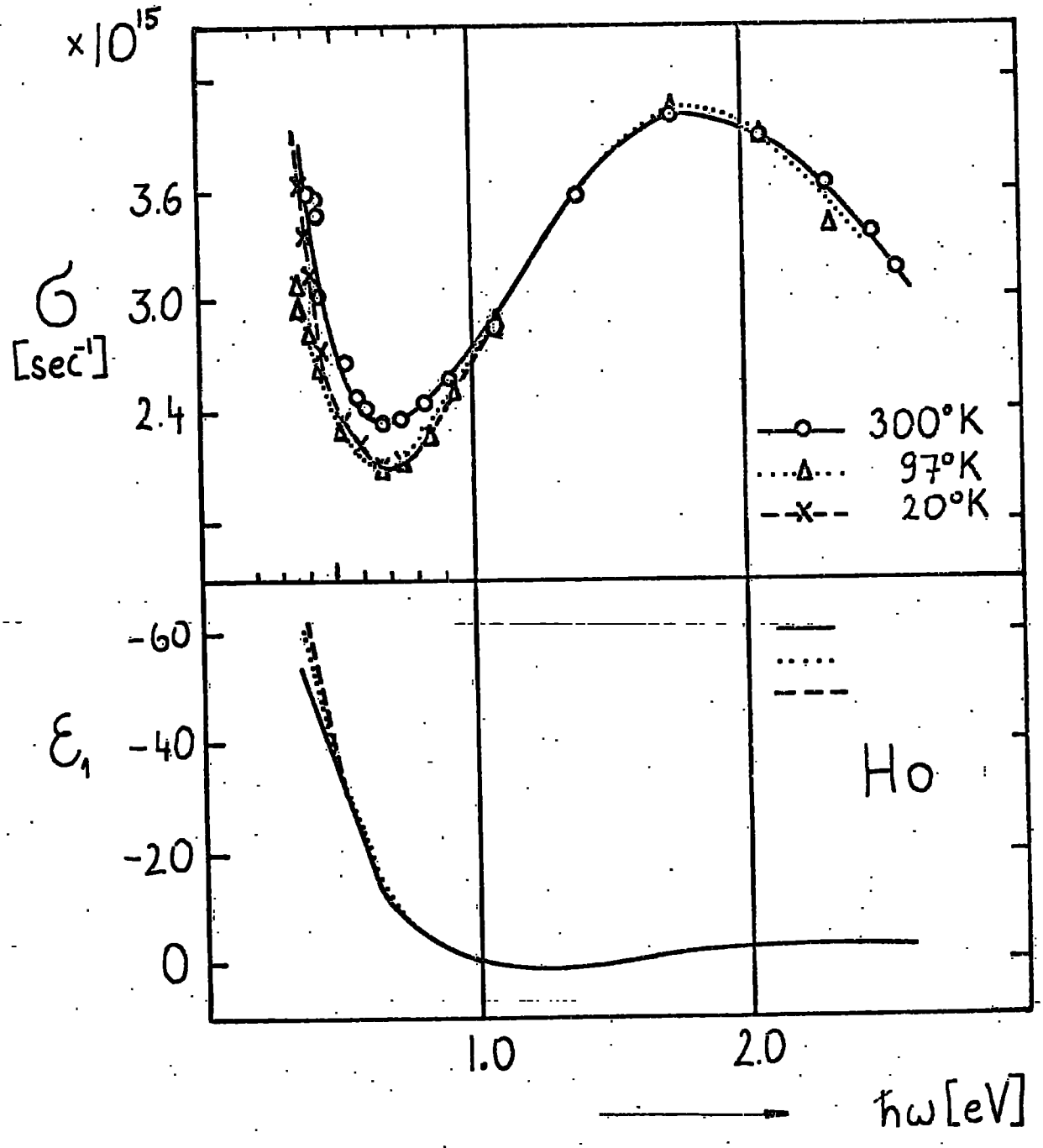

Fig.V.11 Optical conductivity $\sigma(\omega)$ and dielectric constant $\varepsilon_1(\omega)$ of Ho films at temperatures shown. $\hbar\omega$ is the photon energy. ($\sigma(\omega)=nk\omega/2\pi$; $\varepsilon_1=n^2-k^2$; n,k are optical constants)

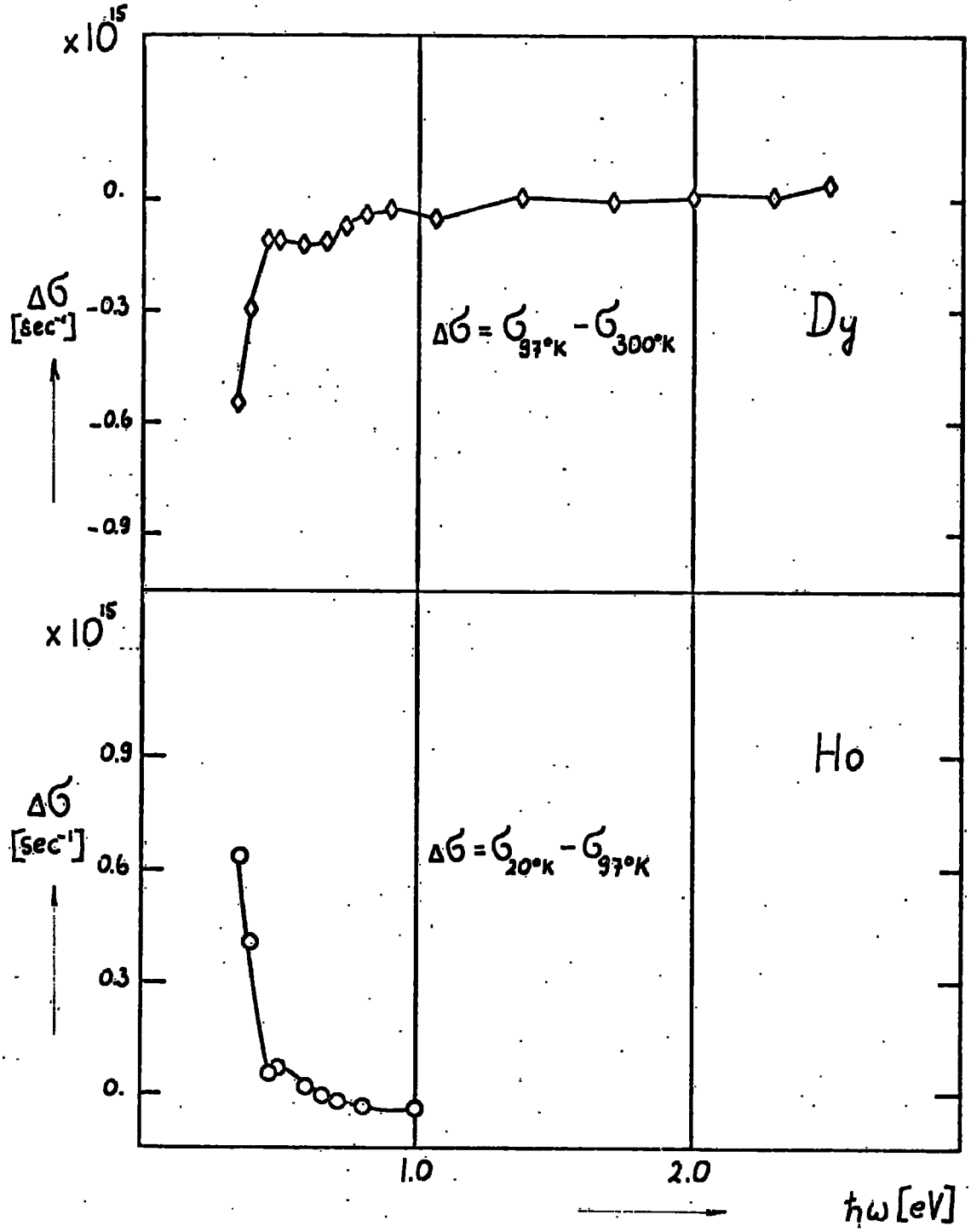

Fig.V.11.a. Changes in optical conductivity of Dy and Ho on cooling; $\hbar\omega$ is photon energy.

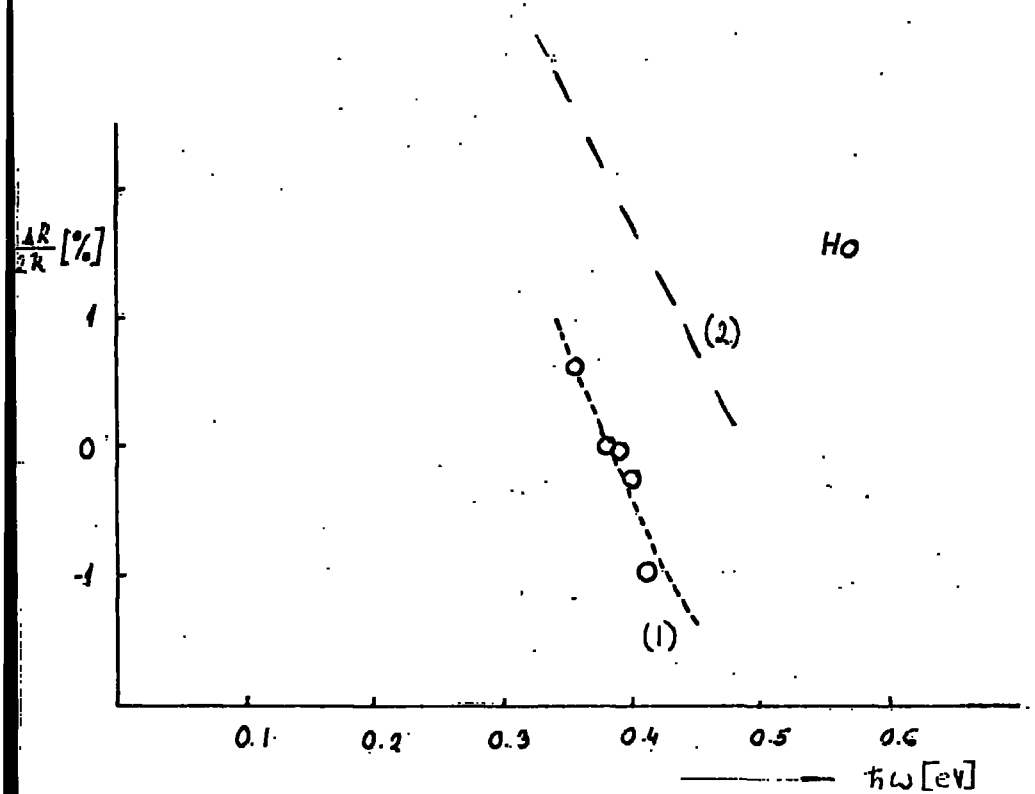

Fig.V.11 b. Fractional change of reflectivity of Ho films

(1) obtained from data in Fig.V.11 , $\Delta R/R = (R(97°K) - R(20°K))/R(97°K)$

(2) obtained by Schüler (1964). $\Delta R/R = (R(120°K) - R(77°K))/R(120°K)$

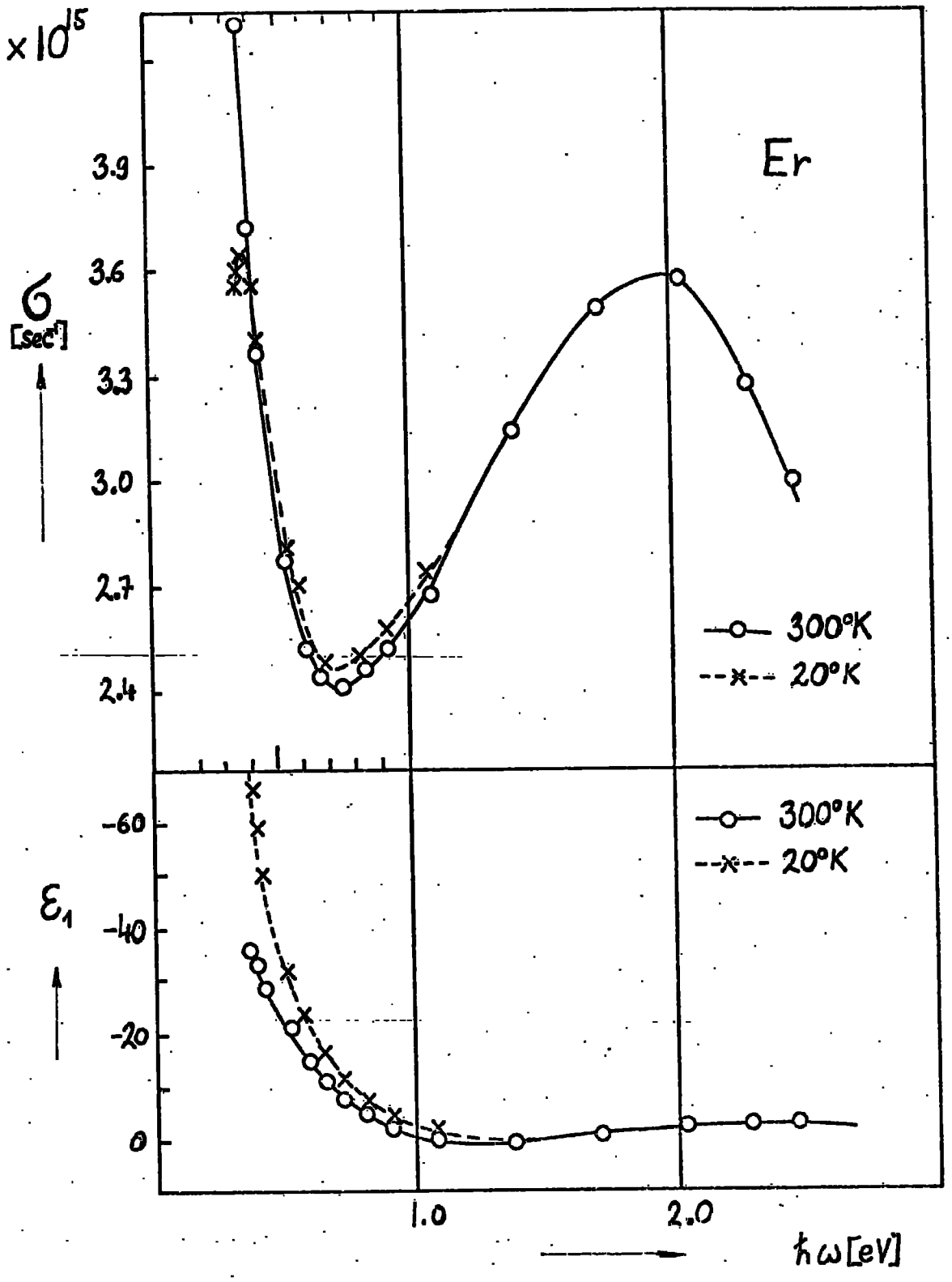

Fig.V.12 Optical conductivity $\sigma(\omega)$ and dielectric constant $\varepsilon_1(\omega)$ of Er films at temperatures shown. $\hbar\omega$ is the photon energy. ($\sigma(\omega)=nk\omega/2\pi$; $\varepsilon_1=n^2-k^2$; n,k are optical constants)

by quite a large increase in the negative dielectric constant $(-\varepsilon_1)$. The overall features of the low temperature behaviour of optical constants however, is similar to the Ho and Dy data rather than to those of Gadolinium and Terbium. To the author's knowledge no low temperature optical data have been reported for Er in literature.

5.7 Ytterbium

The optical constants of ytterbium at room temperature and 90°K are shown in Fig V.13. Comparison with the above data for the heavy elements shows no common features. It is also worth noticing that the absolute value of $\sigma(\omega)$ between 0.5 eV and 2.5 eV is much smaller than the corresponding values for the heavy rare earths. Measurements of the optical properties of Yb have also been reported by Müller (1965) and Endriz and Spicer (1970). The peak in $\sigma(\omega)$ at 1.3 eV in the present data corresponds to the slight bump in $\sigma(\omega)$ at the same photon energy in the data obtained by Endriz and Spicer (1970). The peak in Muller's results occurs at slightly higher photon energies. Absolute values of $\sigma(\omega)$ reported by Endriz and Spicer are approximately 40% higher than the presented data. The values obtained by Endriz and Spicer were calculated from reflectance data which presents uncertainties in low and high frequency extrapolation. To check on the discrepancy, reflectivity was calculated from ellipsometric data on Fig V.13. The results of these calculations are shown in Fig V.14. The present values are slightly higher than Müller's data and lower than those obtained by Endriz and Spicer.

This would probably be the cause of the discrepancy with Endriz's data.

5.8 Neodymium

An attempt was also made to prepare thin films of light Rare Earths which are comparatively more reactive in air than the heavy elements. Nd is one example of the investigated metal and the same technique was

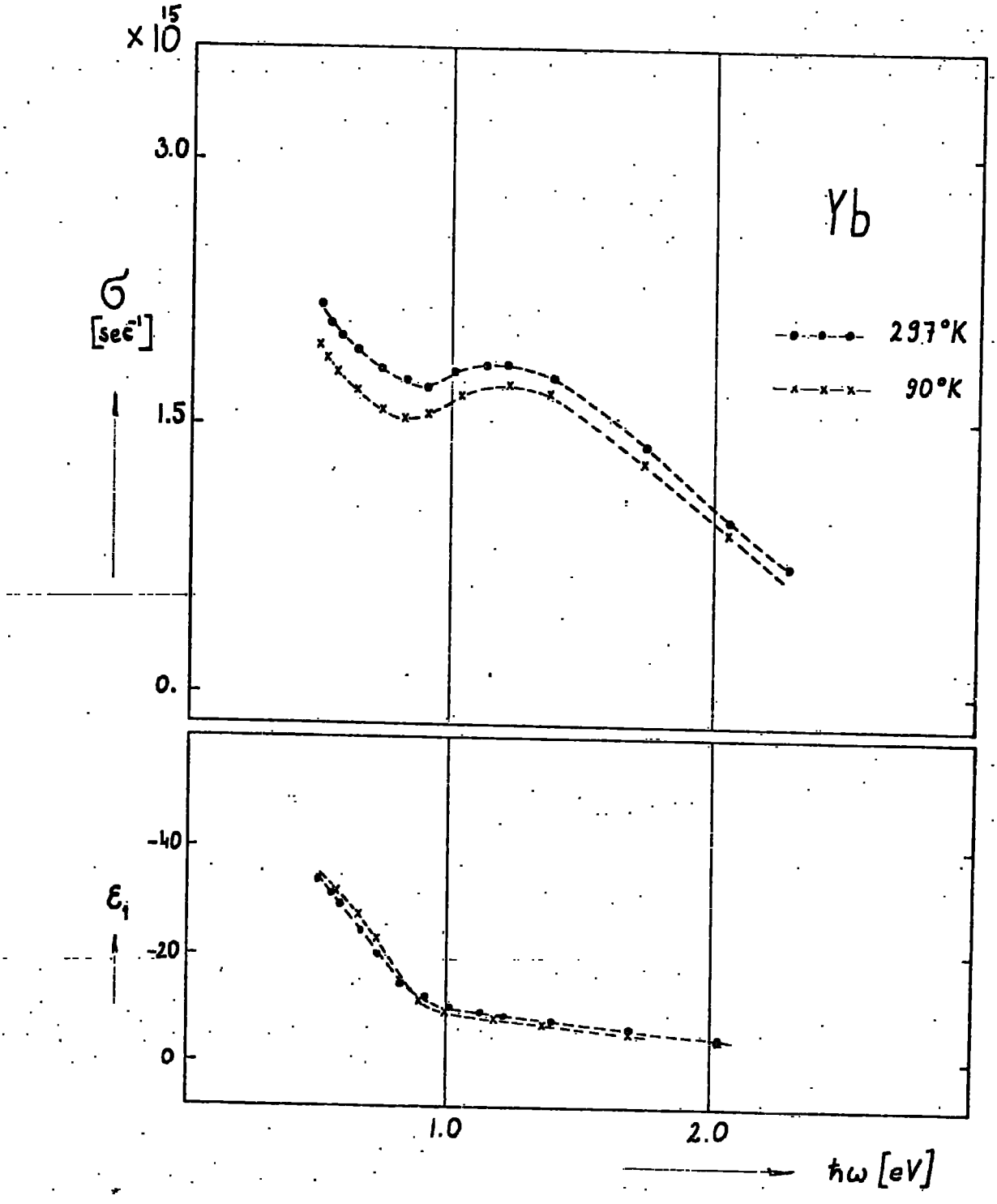

Fig.V.13 Optical conductivity $\sigma(\omega)$ and dielectric constant $\varepsilon_1(\omega)$ of Yb films at temperatures shown. $\hbar\omega$ is the photon energy. ($\sigma(\omega)=nk\omega/2\pi$; $\varepsilon_1=n^2-k^2$; n,k are optical constants)

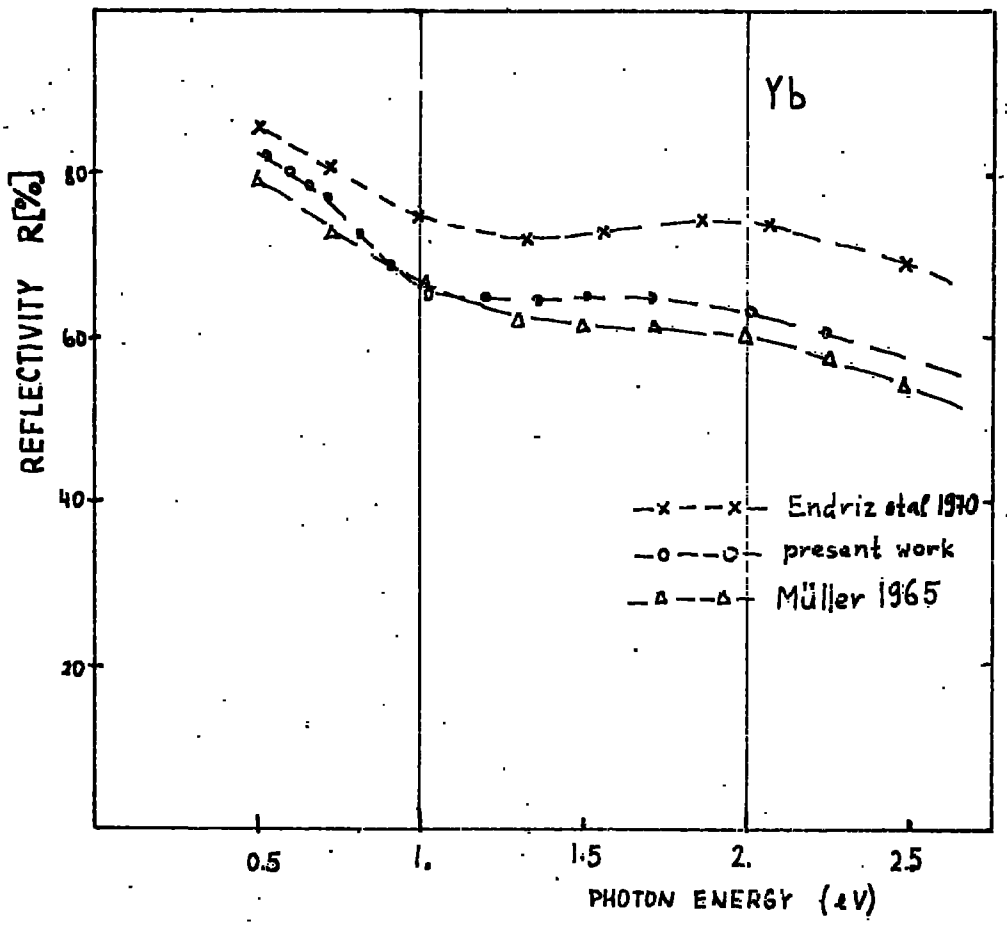

Fig.V.14. Reflectivity at normal incidence for Yb calculated from data on Fig.V.13. The results of other workers are shown for comparison.

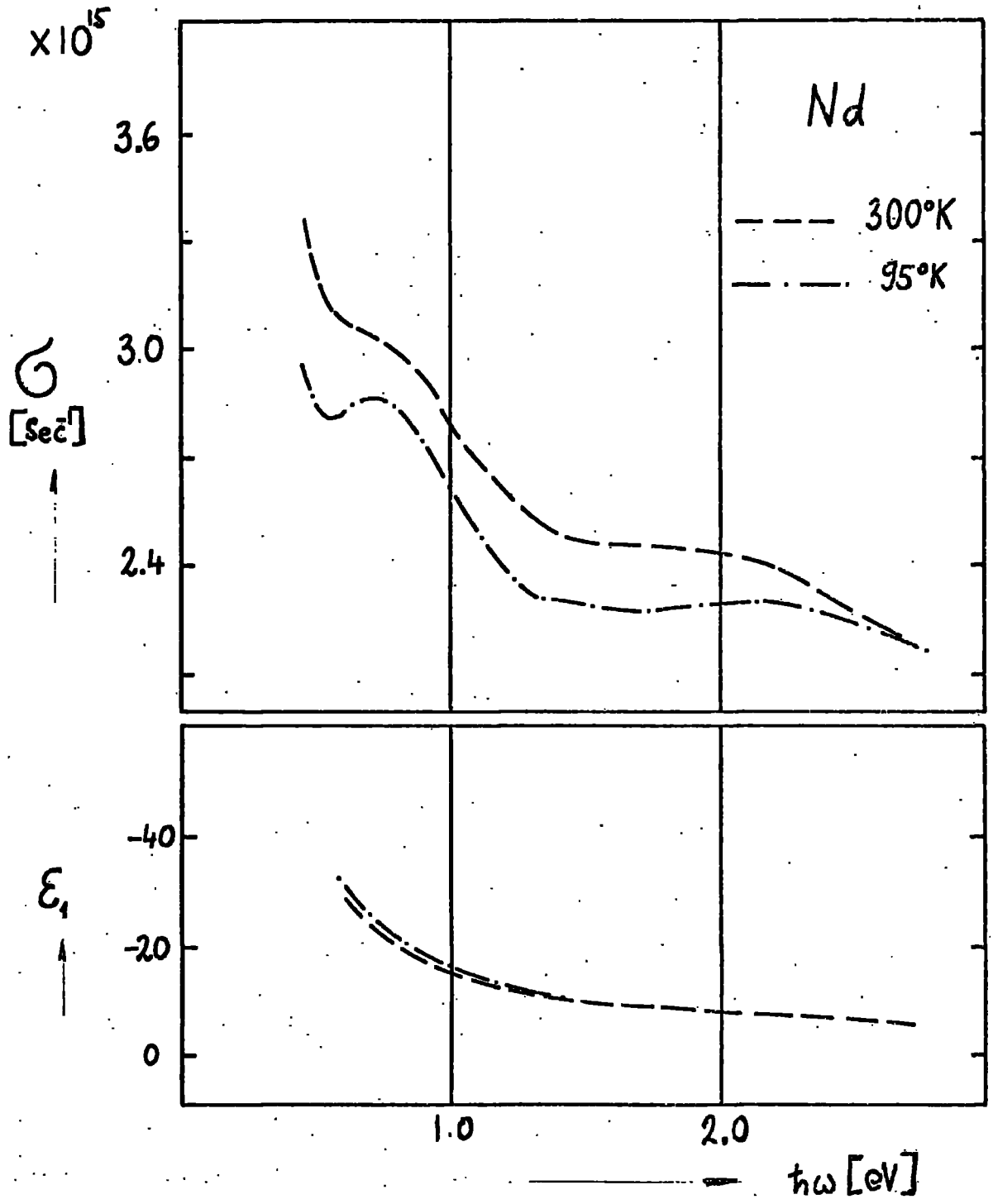

Fig.V.15 Optical conductivity $\sigma(\omega)$ and dielectric constant $\varepsilon_1(\omega)$ of Nd films at temperatures shown. $\hbar\omega$ is the photon energy. ($\sigma(\omega)=nk\omega/2\pi$; $\varepsilon_1=n^2-k^2$; n,k are optical constants)

used as for the heavy elements.

Fig V.15 shows variation of $\sigma(\omega)$ and $\varepsilon_1(\omega)$ with photon energy between 0.5 eV and 2.5 eV at 300°K and 95°K. No extra peaks in $\sigma(\omega)$ appeared on cooling to the lower temperatures. The only observable structure at 0.9 eV becomes more pronounced at low temperatures. The interesting feature of these results is that there is no broad peak in $\sigma(\omega)$ between 1 eV and 2 eV. This agrees with results reported by Kern (1957) and with those recently reported by Pétrakian (1972) even though this latter comparison should be considered rather carefully because Pétrakian's films were much thinner than ours.

CHAPTER VI.

DISCUSSION

6.1 Introduction

6.1.1 The Heavy Rare Earths in the Paramagnetic State

In this Chapter the experimental results of the rare earth metals will be discussed in the light of evidence that has appeared in the literature and data described in Chapter V. If we compare the frequency dependence of the optical constants of the heavy elements presented in the previous Chapter we can notice some common features in the results. The room temperature curves of $\sigma(\omega)$, $\varepsilon_1(\omega)$ are almost identical and are characterised by a broad peak in $\sigma(\omega)$ between 1.5 eV and 2 eV, a minimum at 0.7 eV and a large increase in $\sigma(\omega)$ and $(-\varepsilon_1(\omega))$ to lower photon energies due to absorption by the free carriers. This is consistent with the recently reported calculations of the electronic structure of these metals (Watson et al. (1968), Keeton & Loucks (1968)) which show a large number of possible direct optical transitions above 1 eV for all heavy R.E.'s. The direct optical transitions at the symmetry points have been considered by Dimmock et. al. (1965), Schüler (1965) and Pétrakian (1972); Schüler's results are presented in section 3.2 (Fig.III.1). In the analyses made by these workers non-relativistic band structures were employed.

However, similar results can be obtained using relativistic band structures as may be seen from the following. Unfortunately there is no relativistic band structure of heavy R.E.'s with calculated symmetry of the levels available in the literature. However, comparing non-relativistic and relativistic energy bands it was possible to deduce, approximately, which of the non-relativistic levels are split by relativistic effects. Then, using the relations between the symmetries of non-relativistic and

relativistic states discussed in Appendix A (Table A1) irreducible representations corresponding to the relativistic levels were deduced. The result of this procedure is given in Fig. VI.3 in which relativistic energy levels of Tb calculated by Jackson (1969) were labelled.

In some cases, when a level is split into several levels by spin-orbit interaction such analysis, solely based on the group theoretical considerations, does not provide full information about the symmetries of the levels but rather gives a list of the symmetries which occur among the split levels without, necessarily, being able to label every individual level. The uncertainty is indicated by quoting possible symmetry notations together, i.e. $H_{8,9}$, $P_4 + P_5 + P_6$ etc.

Using the Table B2 (Appendix B) optical transitions at symmetry points were deduced. These are indicated in Fig. VI.3. Comparison with Fig. III.1 shows that both relativistic and non-relativistic band structures predict similar optical properties in the paramagnetic phase. (Optical transitions at symmetry points which do not occur in Fig. III.1 can be derived from Fig. II.8 and Appendix B).

There are, however, other transitions, which were omitted in the above analysis and which are likely to be equally important. As may be seen from Fig.II.8 there are large flat bands along the symmetry axes T, P, S, Σ, T', U, R both below Fermi level E_F and above E_F. Their separation is approximately 2 eV. As may be deduced from Table B1 (Appendix B) and Fig. II.8. optical transitions between these bands are allowed. It is likely that a similar situation also occurs at the general points of the Brillouin zone. These transitions which involve a large area of the Brillouin zone are likely to be quite intense. Interpretation of the absorption spectra connected

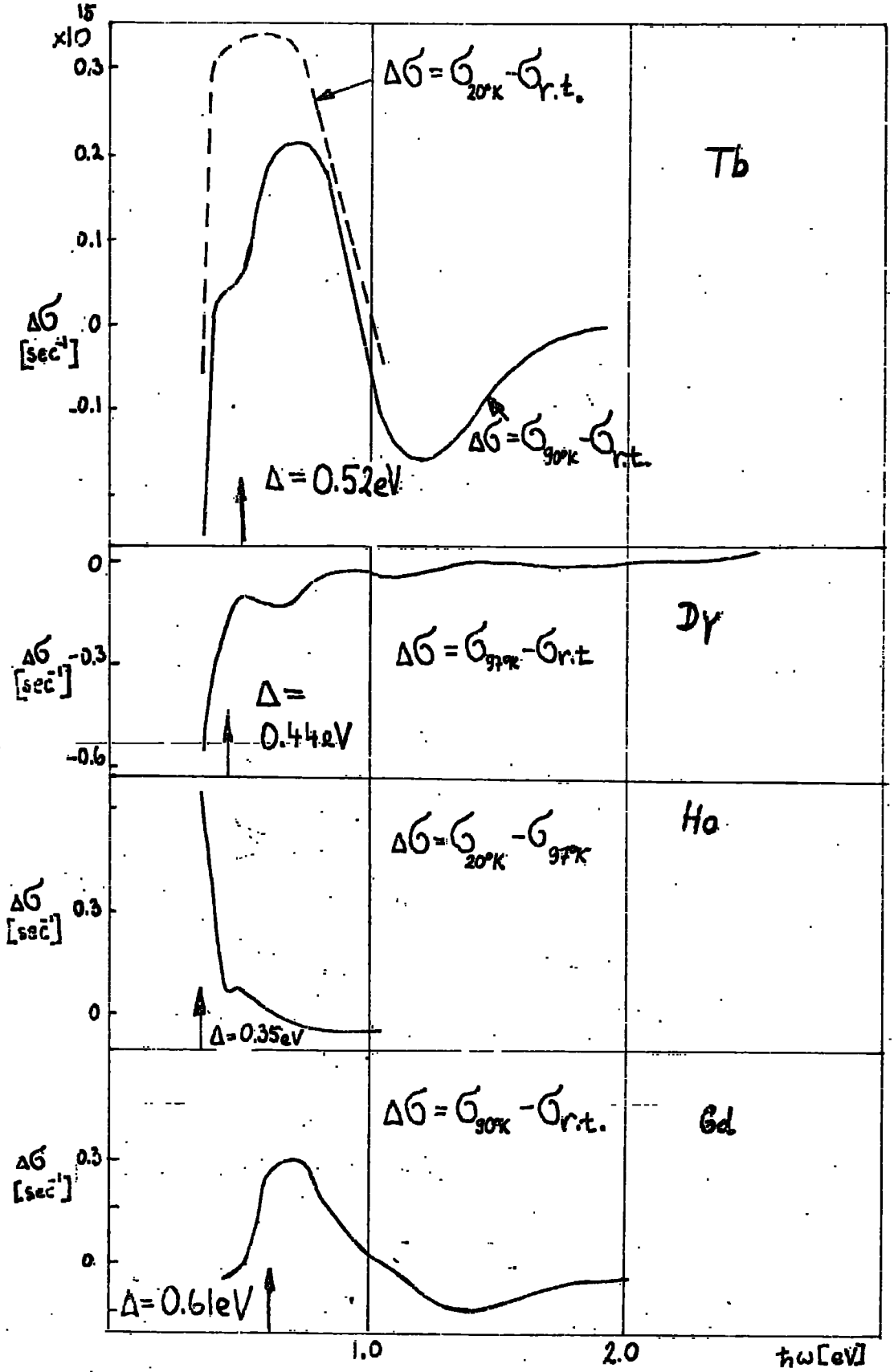

Fig.VI.1. Optical Effect of magnetic ordering in Heavy R.E. metals. Arrows indicate estimated exchange splitting due to Watson et al.(1968).

with such a complex system of interband transitions is very complicated and needs a detailed knowledge of the band structure and especially transition matrix elements.

6.1.2 Mechanisms involved in the Optical Effect of Magnetic Ordering of R.E. Metals

As described in the previous Chapter the most interesting feature of the present investigations is the study of the optical effects of magnetic ordering in R.E. metals. Since R.E. metals order at low temperatures let us summarize the observed effects of cooling on optical properties. These are as follows :

1) Changes in the optical properties in the paramagnetic range of R.E. metals are characterized by a decrease in $\sigma(\omega)$ in the region of the free electron absorption (i.e. below 1 eV). These changes occur in the magnetic phases also but are overshadowed by the other effects mentioned below. Nevertheless, the free electron contribution to the effect of cooling has to be considered even in the ordered phases.

2) The changes occur gradually on cooling and no sudden changes occur as the temperature is decreased below the ordering temperature. On the other hand, peaks in $\sigma(\omega)$ observed for the heavy R.E. metals below ordering temperatures are undoubtedly associated with ordering.

3) Optical properties seem to be independent of the particular type of magnetic order as no changes in optical constants of Dysprosium were recorded during the transition from the helical to ferromagnetic ordering by an application of an a.c. magnetic field in excess of critical field strength (section 5.4) even though Dysprosium shows anomalies connected with magnetic ordering.

4) Another interesting fact is that the photon energies, at

which the low temperature peaks in $\sigma(\omega)$ of R.E. metals are located, decrease along the R.E. series from Gd towards Ho (Fig.VI.1) i.e. the photon energy decreases as the total ionic moment of a metal decreases. As may also be seen from Fig. VI.1 the peak positions on the photon energy scale accord with the estimated values of the energy gaps produced by exchange splitting (Watson et. al. (1968)). The estimations were based on a simple theory of the ferromagnetic exchange mentioned in section 2.3.3 (b), (a).

This suggests that exchange splitting is a dominant force which is responsible for the structures in $\sigma(\omega)$ below the ordering temperatures.

The other feature which seems likely to be able to contribute to the optical effects is the large magnetostriction, which occurs in these metals and it is thought to be the driving force in the stabilisation of ferromagnetic ordering in these metals (Chapter II). Magnetostriction, characterised by changes in the lattice constants Δa, Δc below the ordering temperatures, produces changes in the band structure which in turn influence the optical constants. The magnetostriction however, depends upon the particular type of magnetic order. For Dy, for example, it produces changes in the ratio $\frac{c}{a} = 0.3\%$ at the transition temperature between antiferro and ferromagnetic phases, which should remarkably change the optical properties at this temperature if this effect is to be observed by optical investigations. Since no such changes have been observed so far, magnetostriction does not seem to contribute to the optical effects in the frequency region presently under investigation.

Another mechanism which, in theory, may influence optical properties is absorption due to transitions across the energy gap of antiferromagnteic superzone boundaries. However, as discussed in section 3.4 (b) and 2.3.3 (c) absorption bands connected with such gaps are in general

dependent on the type of the ordering which may again seem to be in disagreement with experimental results. On the other hand the estimated sizes of the gaps at superzone boundaries have the same value as those caused by exchange ferromagnetic splitting. The band structure of the antiferromagnetic metal is too complicated to make further analysis worth while; investigations on single crystals and calculations of the conduction electron wavefunctions are necessary. This also means working out symmetry of the wavefunctions.

To return to the discussion of optical effects due to the ferromagnetic exchange splitting relativistic energy bands of R.E. metals are adopted, since relativistic effects play an important role in the heavy elements and non-relativistic band structures may not be accurate enough for interpretation of the effects, which depend upon the fine level structure near to the Fermi level. The fine energy level structure is available only for Tb and Dy(Keeton and Loucks (1968), Jackson (1969)) and is shown in Figs. VI.3 and VI.4. However, as already mentioned in section 2.4 the electronic structures of heavy R.E. metals are very similar and for further discussion the RAPW band structure of Tb shown in Fig. VI.3 can be regarded as typical of all heavy R.E. metals.

The mechanisms involved in the optical effect of ferromagnetic exchange splitting are discussed in section 3.4 (a). It follows from this section that substantial spin orbit interaction, which occurs in heavy R.E.'s, is likely to produce non-zero optical transition probabilities for all levels which are within a half of the exchange splitting energy of the Fermi level. (The exchange splitting energy is estimated by Dimmock et.al (1965) to be 0.4 eV).

It follows that it is necessary to consider general points of the Brillouin zone, all axes and symmetry points where levels lie within

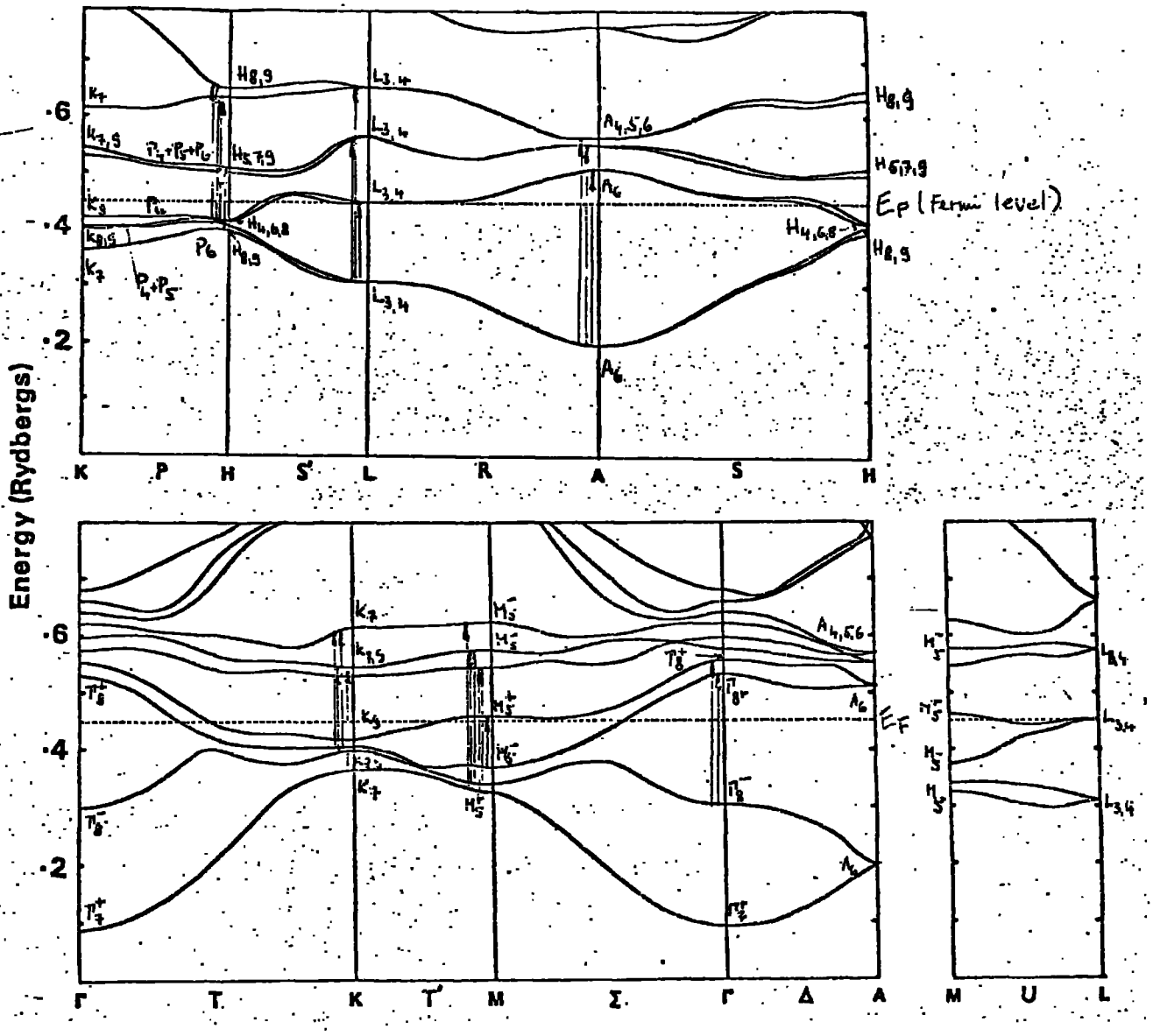

Fig.VI.3. Relativistic energy bands of paramagnetic Tb (Jackson 1969) with indicated symmetries of the levels. Arrows indicate interband transitions at the symmetry points in the Brillouin zone.

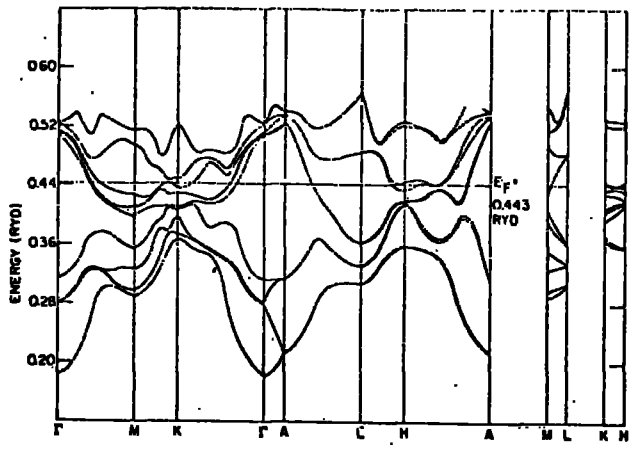

FIG. VI 2 La energy bands along high-symmetry directions. (After Fleming et al. (1968))

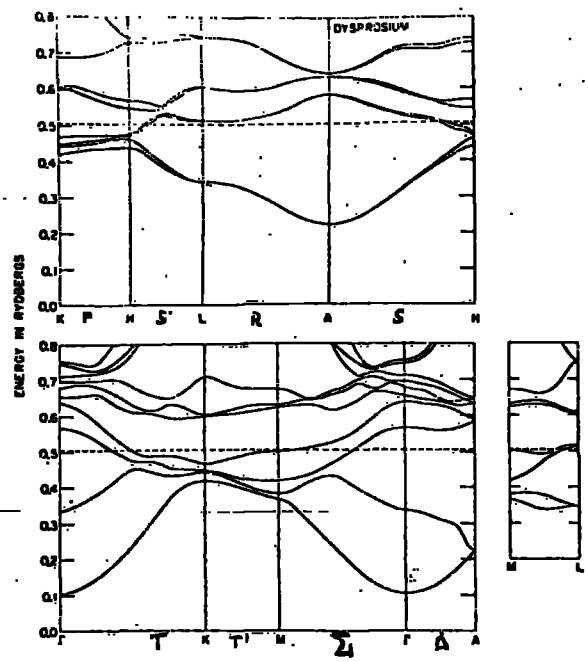

FIG. VI 4 Energy bands for Dy along the symmetry axes of the Brillouin zone. The dashed line indicates the Fermi energy.
(Keeton + Loucks (1968))

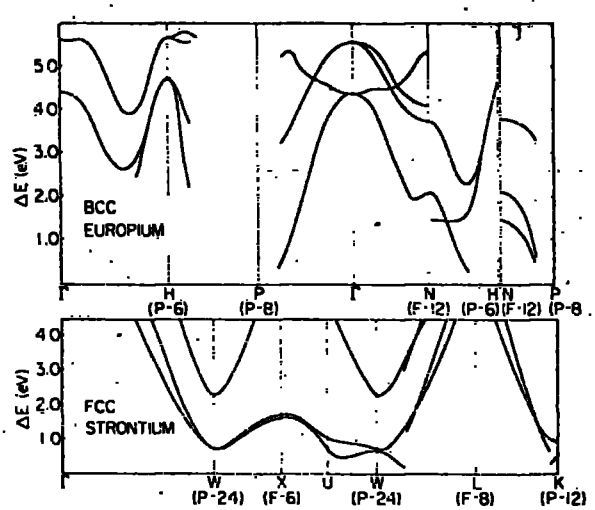

FIG. VI 5 Energy differences between filled and empty bands plotted along symmetry lines in the Brillouin zone for bcc Eu and fcc Sr. The number of equivalent points or faces in the zone are annotated in parentheses by "P" or "F," respectively.
(Endriz + Spicer (1970))

0.2 eV of the Fermi level.

The following discussion does not consider transition probabilities due to lack of the available theoretical data.

6.2 Gadolinium and Terbium

In the interpretation of the present optical effects in terms of exchange splitting of bands near the Fermi level one must ask whether use of the results of RAPW calculations for bulk material is justified for thin films. In order to further examine this point, Tb films were examined by X-ray diffraction technique. The crystal structure of the films proved to be hexagonal with c/a axial ratio c/a = 1.583 + 0.005 which is slightly in excess of the bulk value $(c/a)_{bulk} = 1.58$ used for the band structure calculations of Tb (due to Jackson (1969)). The Fermi surface of Tb is thought to be particularly sensitive to any slight change in the potential or structure which would result in shifts of the energy level near to the point L and which would result in large changes in the occupation of the levels in this area. The temperature dependence of the resistivity of Tb films near to the ordering temperatures of the bulk material did not show any clear evidence for the two transition temperatures at 229°K and 220°K; only one peak was observed at about 220°K. This does not show conclusively that the antiferromagnetic phase is (Fig. V.6a) absent, but it suggests that a reduction of the antiferromagnetic temperature range may have occurred. Tb has been examined more closely than the other metals because of this sensitivity. Summarizing, the band structure for Tb - bulk material calculated by Jackson (1969) can be used for films bearing in mind that the levels will be shifted towards those corresponding to Gd.

The fact that no antiferromagnetic structure in the optical conductivity of Tb was observed in the infra-red is not surprising, since

we cannot rule out the fact that the spin disorder scattering at these temperatures leads to a lifetime broadening of the absorption peaks making them unresolvable over the narrow temperature range (220 to 229°K) of the helical order.

Because of the slight excess in the c/a ratio of Tb films towards the value corresponding to Gd we would expect the energy level near to the point L to be slightly shifted towards or even below the Fermi level. The absorption band below 0.5 eV for Tb probably corresponds to the numerous transitions between the large exchange split portions of the conduction bands along the symmetry axis S , since such flat portions are connected with a high joint density of states, as mentioned above. The fact that the peak in $\sigma(\omega)$ at 0.5 eV is observed only at very low temperatures indicates that one of the split bands is very close to the Fermi level. The final decision however, can only be made by more detailed calculations of the energy levels for various c/a ratios and these are presently being evaluated. Because of the similarity between the band diagrams of Gd and Tb, Gd may be discussed in the same way as above, since the only difference from the Tb results would be that the energy levels at L probably lie up to 0.6 eV below the Fermi level since the webbing feature does not appear in this metal (Keeton & Loucks (1968)). According to the above analysis intense transitions related to spin split bands may also occur at symmetry points H,K,M along axes S,P,R,T and possibly at general points of the Brillouin zone near to the point K producing the peak in $\sigma(\omega)$ at 0.7 eV. The general points are considered because the transitions between the spin split bands are "parallel band transitions" (Section 3.4) in which singularities in the joint density of states occur at the general points. The decrease in $\sigma(\omega)$ for photon energies above 1 eV on cooling below the ordering temperature may be related to the peaks

in $\sigma(\omega)$ below 1 eV as may be seen from the following. At the point H four energy levels (denoted in Fig.VI.3 as $H_8 + H_9$; $H_4 + H_6 + H_8$) occur very close to each other. These four levels were produced by the splitting due to the spin orbit interaction. When the levels at H are split by the exchange interaction one of the spin-up bands may move above the Fermi level and become unoccupied permitting new optical transitions below 1 eV and at the same time reducing transitions to higher levels which occur about 1 eV. The same applies to the levels at the point K and flat bands which occur near to this point probably along all directions in the Brillouin zone.

Gd results may be discussed in the same way.

6.3 Dysprosium

A different situation occurs in Dysprosium. The level $L_{3,4}$ is probably much further above the Fermi level so that it might be possible that this level does not take part in the optical effects of the exchange splitting. At the same time the levels at points H and K probably do not contribute to the optical properties. This is the area where most of the intense transitions near 0.7eV occur in Tb and Gd producing quite a broad structure in $\sigma(\omega)$ below 1eV and above the energy corresponding to the size of the exchange energy gap. The fact that no such structures exist for Dy, Ho, and Er indicates that exchange splitting in these three metals is not large enough to shift any of the levels at H and K above the Fermi level to make these transitions allowed. We therefore conclude that the difference between the Dy-like anomalies in $\sigma(\omega)$ and Tb-like anomalies may be attributed solely to the effect of exchange splitting near to the points H and K. Some qualitative conclusions can therefore be made about the position of the first energy level at the point H and K. They probably lie within 0.2eV below the Fermi level.

6.4 Holmium and Erbium

According to the recent relativistic calculations of the energy bands of Er and Ho the energy band structure in these metals is very similar to that of Dy, the only differences being near to the point L where the level $L_{3,4}$ has probably moved even further above the Fermi level producing a more pronounced webbing feature near to point L (Keeton & Loucks (1968)).

On cooling the Ho films down to 22°K (i.e. below the ordering temperatures) the broad absorption band with a maximum at 1.8eV remains almost unchanged and presumably arises from similar transitions to those responsible for the related peak in the other metals. No absorption band is observed at 0.8eV which indicates a

similarity with the Dy results. Since no peaks connected with ordering are observable in Ho above 0.35eV the size of the energy gap of Ho may be estimated to be less than the predicted value of 0.35eV (Watson et.al.1968). The rapid rise in $\sigma(\omega)$ near to 0.35eV however is probably associated with this peak and its maximum may not be far below the observation limit of 0.35eV. As has been indicated above, the absence of structure at 0.7eV presumably occurs because the exchange splitting is insufficient to cause the spin down levels along P between H and K, and at H and K to move above the Fermi level and in this sense is identical to the behaviour of Dy.

The only significant difference between the results for Er and those discussed above for Ho is the appearance at 20°K of a relatively sharp maximum in $\sigma(\omega)$ at 0.36eV. As may be seen from Fig. V.12 this corresponds to the rapid rise in $\epsilon_1(\omega)$ at this temperature. Its seems likely that both of these features are connected with transitions involving exchange split bands. It is unclear whether the peak position gives a measure of the exchange splitting directly, as we believe to be the case for the other metals, since its value would then be greater than that of Ho which is not as predicted by Watson et.al.(1968). It is possible that the peak corresponds to transitions involving two exchange split levels at the same value of the wave-vector as might be expected for the small predicted exchange splittings when appreciable interference due to the other bands might be expected.

6.5 Neodymium

As may be seen from Fig. V.15 there is a remarkable difference between these results and those of the heavy metals. In order to understand these differences it is useful to examine the available details of the electronic structure in these metals. Figs. VI.2 and 4 show a comparison of the band structures of all the double hexagonal light rare earth metals La, Pr and Nd and those of Dy, which is taken as typical of the h.c.p. heavy rare earth elements. It is clear from this comparison that:

a) the band structure near the Fermi level is much more complicated in Nd than in the heavy rare earths and therefore there are relatively more transitions possible in the region 0.5eV to 1.0eV than in heavy rare earths where a minimum typically occurs in $\sigma(\omega)$ at 0.7eV.

b) the bands at K and H are much more widely spread than for the heavy rare earths and there is no band nesting near to point L. Further, no flat portion of the conduction band exists along the P-axis. Since it is likely that the transitions in this region are partly responsible for the $\sigma(\omega)$ peak at 1.8eV in the heavy rare earths, we should now expect at most only a slight maximum in $\sigma(\omega)$ for Nd at this photon energy.

Returning to the Nd results, the peak in $\sigma(\omega)$ at 0.85eV probably corresponds to the numerous allowed transitions near to points H and K. However nothing definite can be said in this respect without extensive work both theoretical and experimental. The low temperature values of $\sigma(\omega)$ are consistently smaller than those at room temperature, an effect which may arise from a reduction of the lifetime broadening.

6.6 Ytterbium

The results for Yb are shown in Fig. V.13. There is a peak in $\sigma(\omega)$ at 1.3 eV. This metal was chosen as a representative of the divalent rare earth metals. It is reported by Endriz and Spicer (1970) that there is a remarkable similarity between the results of optical investigations of Yb and those of the alkaline-earth metals namely Sr.

Since no band structure calculations have been performed on Yb so far we use this similarity with Sr and employ the band structure calculations for Sr in the discussion of Yb. Fig. VI.5 shows the differences between the filled and empty bands plotted along the symmetry lines in the f.c.c. Sr with the number of the equivalent symmetry points and faces. Table VI.1 shows photon energy of the peak in $\sigma(\omega)$ observed by various authors compared with the photon energies of the possible transitions as deduced from Fig. VI.5. It may be noticed from Fig. VI.5 that some transitions might occur even below 0.5 eV. Again detailed calculation of the energy bands of this metal is necessary.

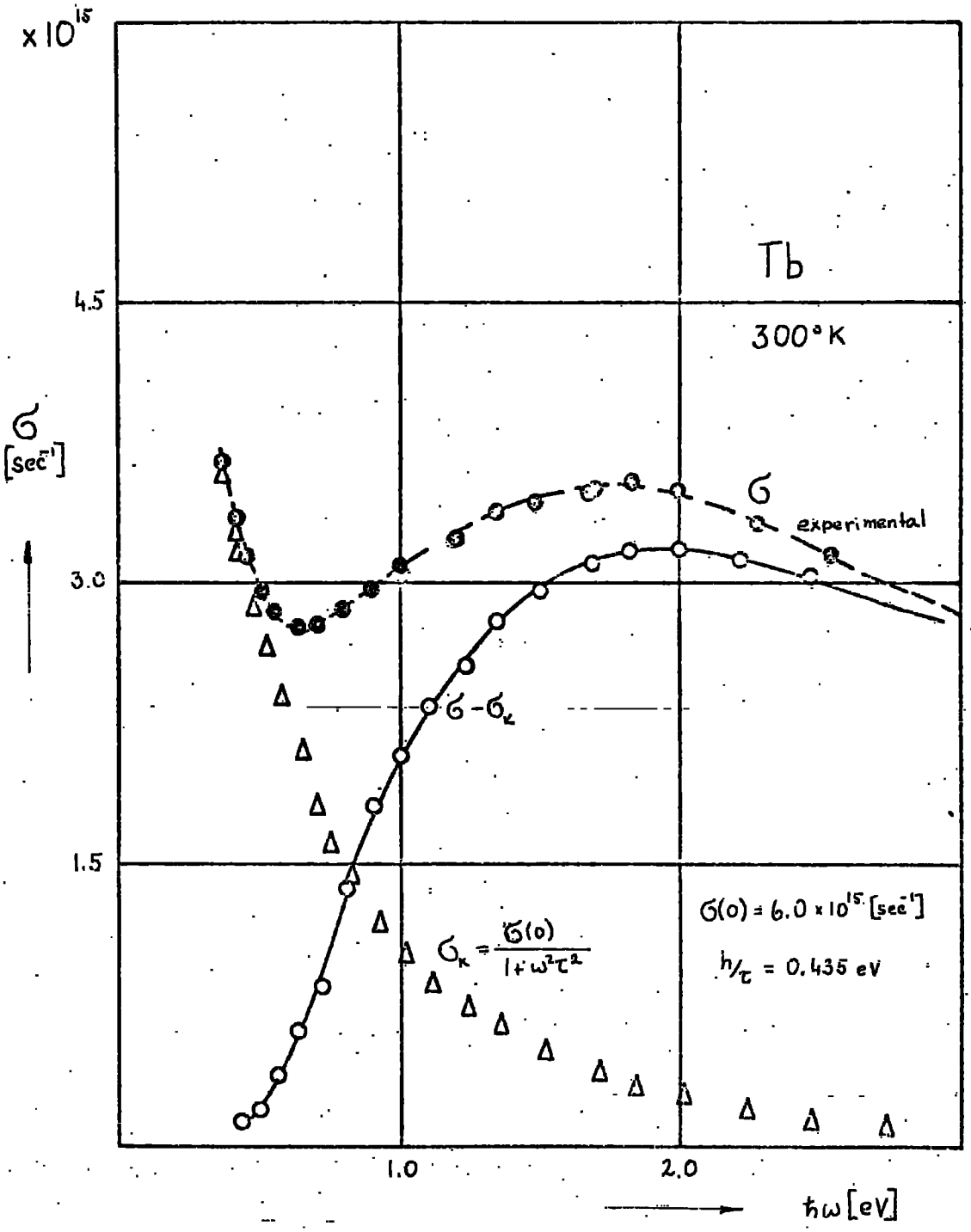

Fig.VI.6. Kramers-Kronig analysis of room temperature Tb data. Low energy extrapolation of $\sigma'(\omega)$ from Fig.V.4 was made using Eq.VI.1 and Eq.VI.2.

TABLE VI 1

Comparisons of experimentally determined peak positions in the optical conductivity of Yb from the present investigation and the work of Müller(1967) and Endriz and Spicer (1970) with the critical point energies deduced from the similarity of the band structures of Sr and Yb. (Fig VI.5)

	Experimental for Yb	PHOTON ENERGIES OF corresponding critical points in Band structure				
		W - X	U(1)	U(2)	K_1	K_2
Present	1.3 eV;					
Müller	1.8 eV	0.7 - 1.7 eV	0.7 eV	1.1 eV	0.4eV	0.9 eV
Endriz & Spicer	1.4 eV					

6.7 The results of Kramers-Krönig analysis

Information about $\sigma(\omega)$ below $\hbar\omega = 0.35$ eV can be obtained from the Kramers-Krönig relation [Landau + Lifshitz (1960)]

$$\varepsilon_1(\omega) - 1 = 8 \times \int_0^{\infty} dw' \frac{\sigma(w')}{w'^2 - \omega^2} \qquad \text{VI.1}$$

Consistent extrapolation of optical conductivity $\sigma(\omega)$ can be chosen by comparing the values of the dielectric constant $\varepsilon_1(\omega)$ calculated from this relation with the directly observed values. The low energy extrapolation was made on an assumption that the thermal broadening effects at room temperature will limit the possible structure in the $\sigma(\omega)$ curve below 0.5 eV and therefore there would be a good chance of finding a unique low energy extrapolation. This consisted of a simple free electron term which is given by the Drude equation.

$$\sigma^{K}(\omega) = \frac{\sigma(0)}{1 + w^2\tau^2} \qquad \text{VI. 2}$$

(the symbols are defined in Section 3.3)

TABLE VI.2.

Low frequency extrapolation of room temperature optical conductivity of Rare Earth Metals

Element	$\sigma(0)/c$ (μm^{-1})	$\rho_o(0)$ (Ω cm)	$\hbar/\tau$ (eV)	Corresp. DC. resistiv. (Ω cm)	Normalised $\rho_o(0)$ for d_{data} Gd	$\frac{\rho_o}{\rho_{DC}}$
Gd	19.4; 20*	152	0.435; 0.4*	130	130	1.17
Tb	20.5	146	0.435	110	125	1.17
Dy	22.	136	0.425	95	114	1.19
Ho	23.2	129	0.4	90	110	1.22
Er	21.	142.5	0.45	50	123.5	7.8
Yb	25.	120	0.4	30		

* Hodgson + Cleyet (1969)

C is light velocity.

An example of such analysis of Tb room temperature data (shown in Fig. V.4) is shown in Fig.VI.6.

The high energy extrapolation only slightly influenced the results below 2.0eV. It consisted of a broad maximum in $\sigma(\omega)$ above 6.0eV. This was performed on most of the metals presently under investigation and the results are summarised in the Table VI.2. A similar analysis was reported for Gd by Hodgson and Cleyet (1969) and these results are also presented for comparison. Values of the optical conductivity at zero frequency $\sigma(0)$ are given in the same units as for $\sigma(\omega)$ in Chapter V. The numerical values of the electron relaxation time τ are introduced in the form h/τ (eV) where h is the Plank's constant. The resistivities corresponding to the calculated $\sigma(0)$ are in remarkable agreement with the d.c. resitivities reported on the bulk materials for Gd, Tb, Dy and Ho. A somewhat low value $\sigma(0)$ for zero frequency for Er data is rather surprising since most of the physical properties, as well as the RAPW energy bands of Er are very similar to the rest of the heavy rare earths. However, the low temperature optical data for this metal show rather different features from the rest of the heavy rare earths. One could of course ask whether these discrepancies do not arise from the strain in the films "built in" during the evaporation of this metal. However, the pressure induced changes in the resistivity of Er have been found to be small as for the rest of heavy rare earths so that we found no reason why this metal should show such different features from the rest of the heavy elements. One of the reasons may of course be due to the fact that a comparatively small number of specimens of this metal were investigated and the absolute values of the optical constants may not be sufficiently precise for this analysis.

The resistivity values corresponding to the optical conductivity

at zero frequency are found to be consistently higher than those of d.c. resistivity. This could arise from the fact that the residual resistivity of the film is always higher than that of bulk material. Another source of the difference is thought to arise from the joint anisotropy of the electron velocity and relaxation time at the Fermi surface. Free electron extrapolation of Yb data at low frequencies gave rather a poor fit and resulted in comparatively small values of $\sigma(0) = 4.5 \times 10^{15}$ sec^{-1}. This may be attributed to the strong interband transitions which are likely to occur at the photon energies below 0.5 eV as may be seen from the Fig. VI.5. Free electron extrapolation of the Nd data failed probably because of the numerous transitions at 0.5 eV predicted from the above picture of the band structure of Nd.

As may be seen from results in Chapter V the free electron absorption was also significant at photon energies below 0.5 eV even at low temperatures and was responsible for some of the difficulty in obtaining accurate values for the splitting parameters of Dy for instance.

An attempt was therefore made to extract the free electron absorption from low temperature results, using the following procedure (applied only to Dy and Tb).

1) The low energy extrapolation of room temperature curves $\sigma(\omega)$ using the free electron term (Eq. VI.2) gave values of zero frequency room temperature optical conductivity $\sigma(0)$ and relaxation time τ.

2) The low temperature values for $\sigma(0)$ were estimated from the d.c. values of conductivity $\sigma_{d.c.}$ taken as being inversely proportional to the sheet resistance ρ_s obtained experimentally (Fig.V.6a for Tb; Fig.V.10 for Dy) assuming that $\frac{\sigma(0)}{\sigma_{d.c.}}$ is approximately a constant function of temperature.

3) Using Eq.III.13 the isotropic relaxation time τ is given

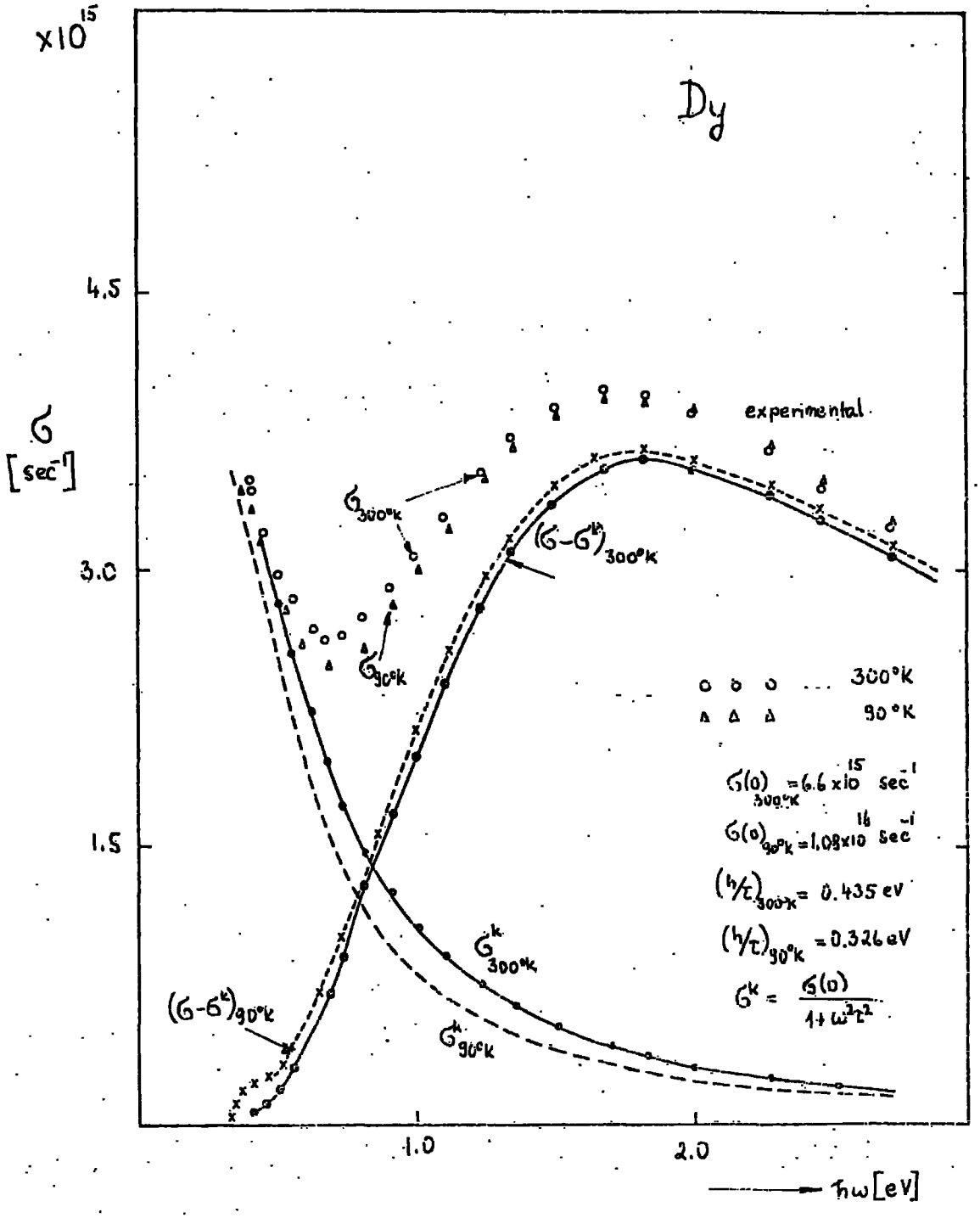

Fig.VI.7. Kramers-Kronig analysis of Dy data. The procedure was the same as for Tb data. Low temperature $\sigma(0)$ was deduced from the data on Fig.V.10 . The relaxation time τ was defined using Eq.III.13 as discussed in the text.

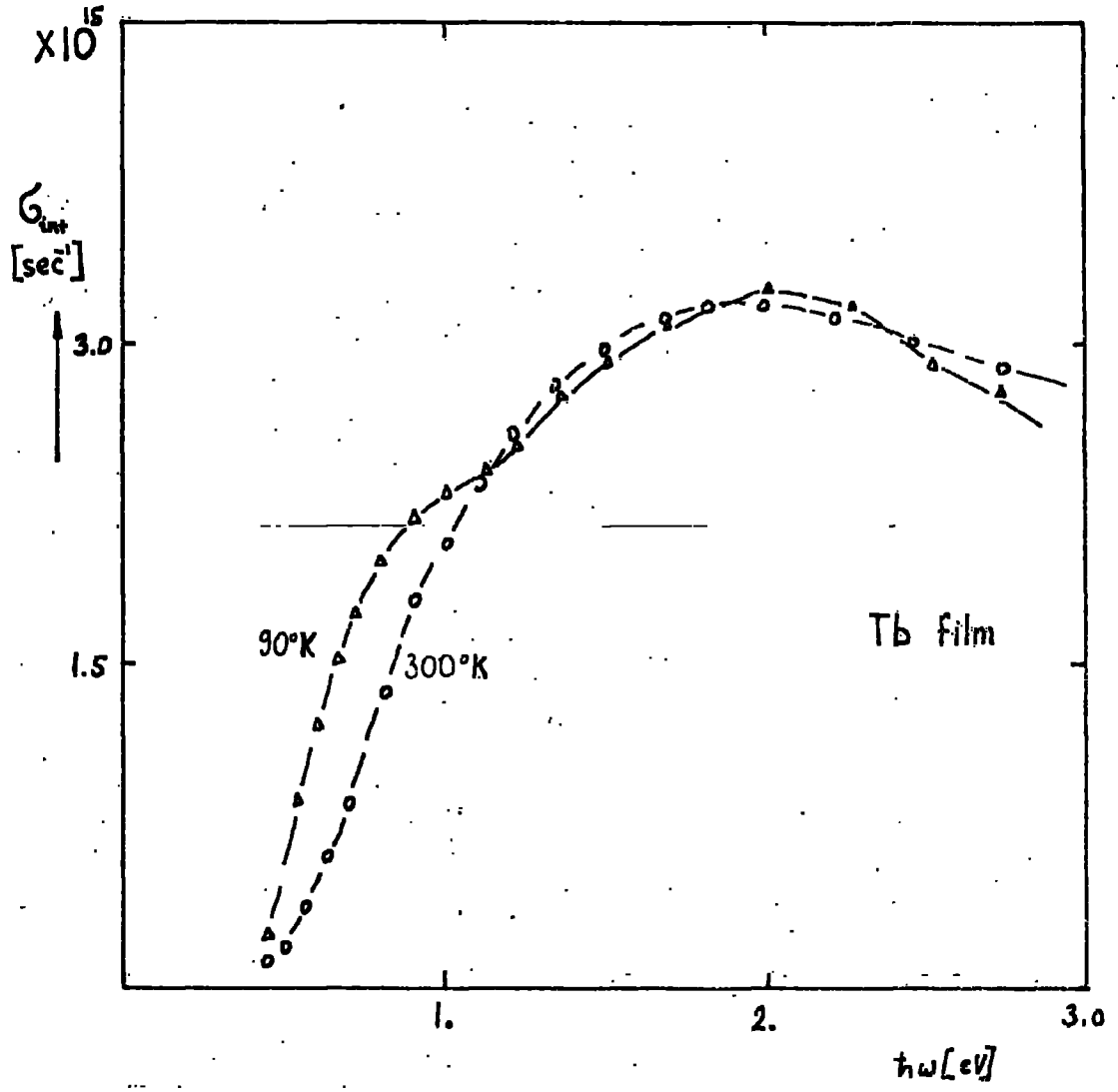

Fig.VI.7a. Estimates of the interband contribution to optical conductivity $\sigma(\omega)$ of Tb at the temperatures shown. The procedure of extraction was the same as used for Dy data shown in Fig.VI.7.

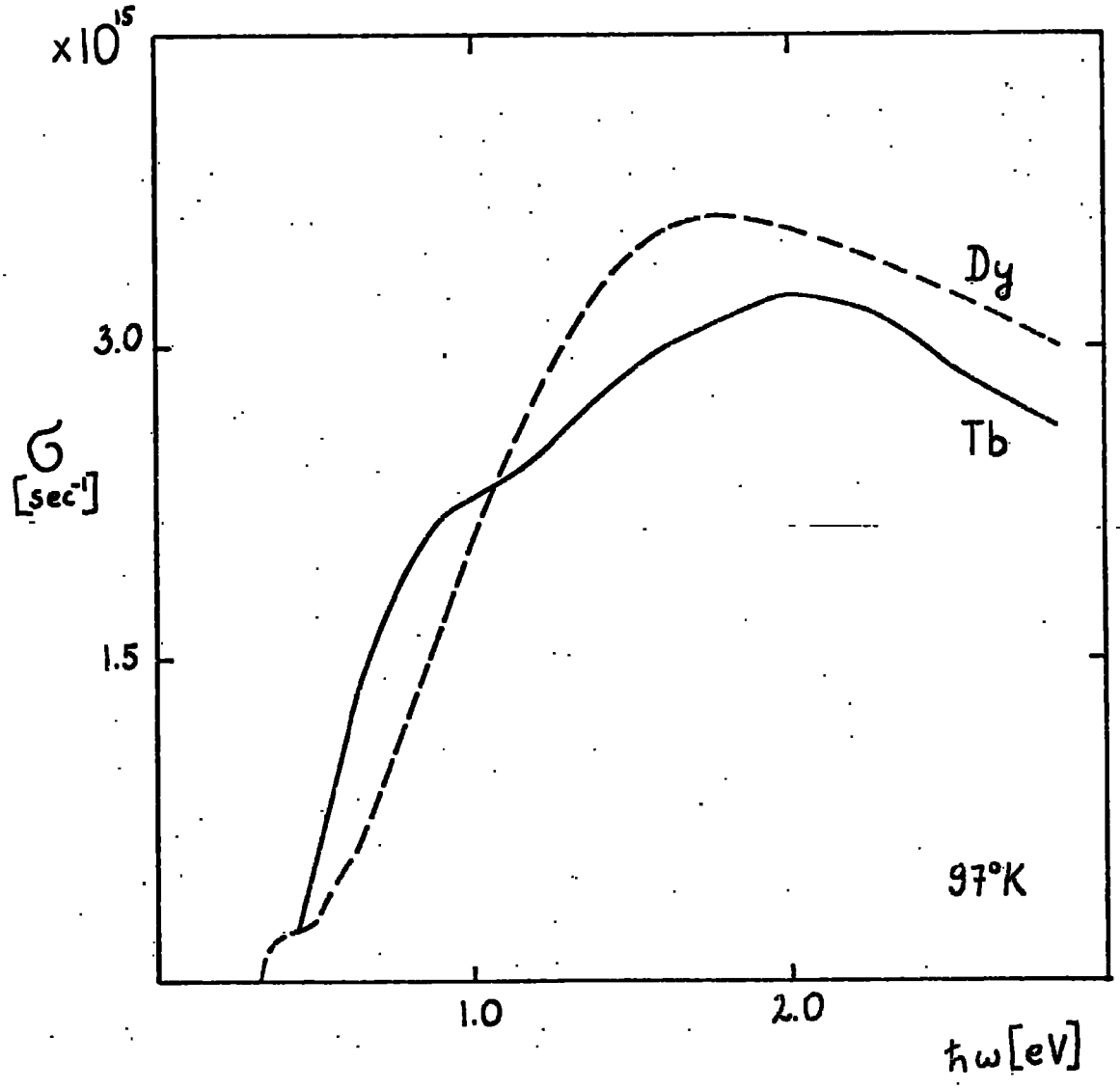

Fig.VI.8. Estimates of interband contributions to the low temperature optical conductivity of Tb and Dy (from Figs. VI.7 and VI.7a).

by

$$\tau = \frac{m^* \sigma(0)}{e^2 N}$$

(m^* is an average electron effective mass at the Fermi surface, N is the number of conduction electrons per unit volume).

Assuming that the change in m^* due to cooling from 300°K to 77°K is much smaller than the change in conductivity $\sigma(0)$ the low temperature value of relaxation time was estimated. Using the above assumptions we can write

$$\tau_{77^\circ K} = \tau_{300^\circ K} \frac{\sigma_{77^\circ K \ D.C.}}{\sigma_{300^\circ K \ D.C.}}$$

The results of the above procedure applied to Dy low temperature data from Fig.V.8 are shown in Fig.VI.7. σ^k on the graph represents a Drude tail, $\sigma(\omega) - \sigma^k$ represents the estimated interband contribution to the optical conductivity. Similar results obtained from Tb data are shown in Fig. VI.7a. Comparison of the above estimates of low temperature interband contributions of Dy and Tb is shown on Fig. VI.8. This shows the difference between low temperature interband absorption of these two metals in the photon energy region 0.5eV to 1.0eV as discussed in sections 6.2, 6.3 etc.

CHAPTER VII.

CONCLUSION

The results reported in this thesis show that in general the optical constants of the heavy rare earths change when the metal under investigation becomes magnetically ordered. The nature of the changes does not depend upon which of the magnetically ordered phases (ferro - or antiferromagnetic) is present, a result which has been taken as indicating that optical transitions at the energy gaps associated with superzone boundaries make no significant contribution to the optical behaviour. Rather, we believe that the dominant contribution to the effect of magnetic ordering on the optical properties arises from the exchange splitting of the conduction bands. Rather surprisingly, no evidence was found for changes associated with the very large magnetostriction which these metals possess.

The exchange splitting of the bands has been estimated for gadolinium, terbium, dysprosium and holmium, the results being in good agreement with theoretical predictions. Only an upper limit to the magnitude of the splitting could be found for holmium and the value for erbium was unexpectedly high.

At room temperature the overall absorption behaviour at low photon energies was dominated by the Drude contribution to the optical conductivity $\sigma(\omega)$ and the zero frequency values $\sigma(0)$, obtained by extrapolation for each of the metals at this temperature showed a similar dependence on atomic number to those obtained by the static conductivity observations. The absolute values of $\sigma(0)$ however were some 15% larger than the static values, an effect which may arise from the joint anisotropy of the velocity and relaxation time at the Fermi surface. This conduction electron scattering contribution was also significant at low temperature and was responsible for some of the difficulty in obtaining accurate values

for the exchange splitting parameters.

Attempts were made to associate the magnetic peaks in $\sigma(\omega)$ with transitions in the APW and RAPW band structures for these metals, but in the absence of wave function data no unambiguous identification was possible. This was also the case for the broad peak near to 1.5 eV, which is common to all the metals, and which did not appear to be changed by magnetic ordering.

CHAPTER VIII

SUGGESTION FOR FURTHER WORK

The present results show that, in general, optical constants of the heavy rare earths change with magnetic ordering and that in all probability the dominant contribution to the optical effect arises from the exchange splitting of the conduction band. It also appears that the band gaps at superzone boundaries may not contribute to the optical effects as is also the case for the magnetostriction. The reasons for the ineffectiveness of the magnetostriction in changing the optical constants may be understood through more detailed calculations of the energy band structure of the heavy rare earths for various lattice parameters and the evaluation of the transition probabilities for various parts of the zone. (This work is already in progress in the laboratory). More extensive studies of the single crystal magnetooptical properties are also necessary if we are to understand the behaviour of polycrystalline films such as have been described in this thesis. The use of differential techniques is capable of providing more detail in the structure of absorption bands than conventional ellipsometry even though these techniques are more complicated to analyse.

It appears that the gaps at superzone boundaries lead to only a small contribution to the optical effects of magnetization and it will be essential to employ differential techniques to discover the form they take.

In order to complete the present investigation of the optical properties at least for the first round it is necessary to continue further into the infra-red region. This work should give some interesting data for Er and Tm at helium temperatures as may prove or disprove that the free electron low frequency extrapolation of $\sigma(\omega)$

presently used below 0.5eV was justifiable.

In addition tc that shown above there is a need for further examination of light rare earths. The first element to be tackled probably should be Eu because of the simplicity of its electronic structure and its relatively high ordering temperature ($90^{\circ}K$). It would be especially interesting to compare the optical effects of magnetic ordering of Eu and the heavy rare earths.

REFERENCES

Abelés, F., (1972), Optical Properties of Solids (North Holland, Amsterdam).
(1973), Private Communication.

Andersen, O.K., Loucks, T.L., (1968), Phys.Rev., 167, 551

Ashcroft, N.W., Sturm, K., (1971), Phys.Rev., 3B, 1899

Barker, A.S., et.al., (1968), Phys.Rev.; Letters, 20, 384

Beattie, J.R., Conn, G.K.T., (1955), Phil.Mag., 55, 222

Behrendt, D.R., et.al., (1958), Phys.Rev., 109, 1544

Blodget, Jr.A.J., et.al., (1965), Optical Properties and Electronic structure of Metals and Alloys (Conference, Paris, Sept 1965) (F.Abelés, Editor, published by North Holland 1966)

Born, M., (1965), Principles of Optics, (Pergamon Press, New York)

Broden, G., (1971), Rare-Earths and Actinides Conference, (Durham, 1971) (Institute of Physics)

Bueche, F., (1948), J.Opt.Soc.Amer. 38, 806

Buijs, K., (1960), Applied Spectroscopy. Vol.14. No.3, 81

Cable, J.W., Wollan, E.O., (1968), Phys.Rev., 165, 733

Callaway, I., (1964), Energy Band Theory, (Academic Press Inc)

Callen E., Callen, H.B., (1966), J.Phys.Chem.Solids. 27, 1271

Clark, A.E. et.al., (1965), Phys.Rev., 138, A216

Cohen, M.H., (1958), Phil.Mag., 3, 762

Colvin, R.W., et.al., (1960), Phys.Rev., 120, 741

Cooper, B.R., (1965), Phys.Rev., 139, A1504
(1969), Solid state Phys. 21, 393

Cooper, B.R., Reddington, (1965), Phys.Rev. Letts. 14, 1066

Coqblin, B., (1971), Conference on Rare-Earths and Actinides, (Durham, 1971) (Institute of Physics)

Corner, W.D., Roe, W., Taylor, K.N.R., (1962), Proc.Phys.Soc. 80, 927

Cornwell, J.F., (1969), Group Theory and Electronic Energy Bands in Solids (North Holland, Editor Wohlfarth E.P.)

Curron, A.E., Chebek, H.G., (1973), J.Phys.F. 3, 1

Dimmock, J.O., et.al., (1965), Optical Properties and Electronic Structure of Metals and Alloys (Conference, Paris, Sept 1965) (F.Abelés, Editor, published by North Holland, 1966)

Dimmock, J.O., Freeman, A.J., (1964), Phys.Rev., Letts., 13, 750

Drude, P., (1890), Ann.d.Physik, 39, 504

Elliot, R.J., (1954), Phys.Rev., 96, 280

Endriz, J.G., Spicer, W.E., (1970), Phys.Rev., 2B, 1466

Enz, V., (1960), Physica, 26, 698

Evenson, W.E., Liu, S.H., (1968), Phys.Rev. Letts., 21, 432
(1969), Phys.Rev., 178, 783

Elliot, R.J., Wedgewood, (1963), Proc.Phys.Soc., 81, 846
(1964), Proc.Phys.Soc., 84, 63

Fedders, P.A., Martin, P.C., (1966), Phys.Rev., 143, 245

Fleming, G.S., et.al., (1968), Phys.Rev. Letters., 21, 1524

Freeman, A.J., Watson, R.E., (1962), Phys.Rev., 127, 2058

Freeman, A.J., Dimmock, J.O., (1966), Bull.Am.Phys.Soc., 11, 266

Freeman, A.J., Dimmock, J.O., Watson, R.E., (1966), Phys.Rev. Letts. 16, 94

Hanus, J., et.al., (1968), J.Appl.Phys., 39, 1272

Harbeke, G., (1972), Optical Properties of Solids (F.Abelés editor), (North Holland)

Hedén, P.O., et.al., (1971), Phys.Rev., Letts. 26, 432

Herring, C., (1942), J.Franklin Inst. 233, 525

Hodgson, J.N., (1970), Optical Absorption and Dispersion in Solids (Chapman and Hall)

Hodgson, J.N., (1972) Private Communication

Hodgson, J.N., Cleyet, B., (1969), J.Phys.C. 2, 97

Ingersoll, L.R., (1910), Astrophys. J., 32, 265

Jackson, C., Doniach, S., (1969), Phys.Letts. 30A, 328

Jackson, C., (1969), Phys.Rev., 178, 949

James, N.R., et.al.,(1952), Phys.Rev., 88, 1092

Kasuya, T., (1956), Progr.Theor.Phys., 16, 45

Kasuya, T., (1966), Magnetism (Ed.Rado, Suhl) Vol.IIB. p.215 (Acad.Press)

Keeton, S.C., Loucks, T.L., (1968), Phys.Rev., 168, 672
(1966), Phys.Rev., 146, 429

Kern, E., (1957), Z.Physik, 148, 38

King, E., et.al., (1970), Phys.Rev., B1, 1380

Kittel, C., (1963), Quantum Theory of Solids, (John Wiley & Sons Inc.,)

Koehler, W.C., et.al., (1961), Rare Earth Research (Ed. E.V. Kleber, MacMillan) p.149
(1962), J.Phys. Soc. Japan 17, Suppl.B.III. 32
(1963), Rare Earth Research, (ed. J.S.Vorres Gordon and Breach), p.199
(1965), Phys.Rev., 140, A1896

Kohn, W., (1965), Optical Properties and Electronic Structure of Metals and Alloys (Conference, Paris, Sept 1965) (F. Abelés, Editor, published by North Holland 1966)

Krinchick, G.S. et.al., (1969), Zh.Theor.Exp.Phys.Letters, 10, 35
(1970), ibid., 11, 105
(1971), J.Physique (Coll C1), 32, C1-1058

Landau, L.D., Lifshitz, E.M., (1960), Electrodynamics of Continuous Media, (Pergamon)

Liu, S.H., (1960), Phys. Rev., 121, 451
(1961), Phys. Rev., 123, 470

Lee, R.S., Legvold, S., (1967), Phys. Rev., 162, 431

Lindgard, P.A., et.al., (1967), J.Phys. Chem. Solids, 28, 1357

Lodge, F.M.K., (1969), Ph.D., Thesis, Durham University, England

Loucks, T.L., (1965), Augmented Plane Wave Method (Benjamin)

Loucks, T.L., (1966), Phys. Rev., 144, 504
(1968), Phys. Rev., 168, 672

Loucks, T.L., Boys, D.W., (1968), Phys. Rev., 174, 373

Loucks, T.L., Liu, S.H., (1971), Private Communication

Miwa, H., (1963), Prog. Theor. Phys., 29, 477

Møller, H.B., et.al., (1968), J.Appl.Phys., 39, 807

Müller, W.E., (1965), Phys. Letts., 17, 82
(1967), Phys. Kondens. Materie, 6, 243

Parker, M.R., (1972), Phys.Stat.Sol.(b), 49, 299

Pétrakian, J.P., (1972), J.Opt.Soc.Amer., 62, 401

Rhyne, J.J., et.al., (1967), Phys. Rev., 154, 266

Rhyne, J.J., Clark, A.E., (1967), J.Appl. Phys., 38, 1379

Rhyne, J.J., (1968), Phys. Rev., 172, 523
(1969), J.Appl. Phys., 40, 1001

Rudermann, M.A., Kittel, C ., (1954), Phys.Rev., 96, 99

Schüler, C.Chr., (1963), Z.Angew. Physik, 15, 218
(1964), Phys.Letts., 12, 84
(1965), Optical Properties and Electronic structure of Metals and Alloys. (Conference, Paris, Sept 1965) (F. Abelés, Editor, published by North Holland, 1966)

Seitz, F., (1936), Annals of Mathematics, 37, 17

Scouler, W.J., (1967), Phys. Rev., Letters, 18, 445

Spedding, F.H., Daane, A.H., (1961), The Rare Earths (New York: J.Willey)

Sprecht, F., (1967), Phys. Rev., 162, 389

Strandburg, D.L., et.al., (1962), Phys.Rev., 127, 2046

Taylor, K.N.R., Darby, M.I., (1972), Physics of Rare Earth Solids, (Chapman and Hall,)

Taylor, K.N.R., (1970), Contemp.Phys., 11, 423
(1973), Private Communication

Watson, R.E., Freeman, A.J., Dimmock, J.O., (1968), Phys. Rev., 167, 497

Williams, R.W., et.al., (1966), Phys.Rev. Letts., 16, 168

Yoshida, K., (1957), Phys.Rev., 106, 893

APPENDIX A

Symmetry of the conduction electron states

The band structure of a paramagnetic metal is derived from the one-electron Bloch equation. If the spin orbit coupling is not included the Bloch equation is in the form

$$\left[-\frac{\hbar^2\nabla^2}{2m} + V(\vec{r})\right] |n,\vec{k}\rangle = \mathcal{E}_n(\vec{k})\,|n,\vec{k}\rangle \,. \qquad \text{A1}$$

$V(\vec{r})$ is the effective one-electron potential with the translational symmetry of the crystal lattice; $|n,\vec{k}\rangle = e^{i\vec{k}\vec{r}}\, u_n(\vec{k},\vec{r})$ are one electron Bloch functions; $\vec{k}$ is the conduction electron wave-vector; function $u_n(\vec{k},r)$ has the translational symmetry of the lattice; n is the band index of the conduction band. Energy eigenvalues $\mathcal{E}_n(\vec{k})$ have the translational symmetry of the reciprocal lattice, therefore the variation of $\mathcal{E}_n(\vec{k})$ with $\vec{k}$ over the first Brillouin zone is usually presented. An example of such variation for Gd is shown in the Fig. II 8. In addition to the translational symmetry the Bloch equation is invariant to the group of transformations which follow from the crystallographic symmetry of the lattice. This group of symmetry transformations of the Hamiltonian in eq. A1 is isomorphic to the space group of the crystal. A trivalent Rare earth crystal lattice has the hexagonal close packed structure and the corresponding space group is called D^4_{6h} (For detailed description of this group see Cornwell(1969) and Elliot (1954)).

Let us denote by T the symmetry transformation of the one electron Hamiltonian. In its most general form, T is a rotation R(T) followed by a translation t(T). Transformation of the coordinates is given by

$$\vec{r}' = \left[R(T)\,|\,\vec{t}(T)\right]\ \vec{r} \equiv T\ \vec{r} \qquad \text{A2}$$

Corresponding change of the wavefunction $f(\vec{r})$ can be represented by the operator P(T) where

$$P(T)\ f(\vec{r}) = f(T^{-1}\ \vec{r}) \qquad \text{A3}$$

Applied on the Bloch waves $u_n(\vec{k},\vec{r})\, e^{i\vec{k}\cdot\vec{r}}$ this is equivalent to the transformation of the wave vector $\vec{k}' = \vec{Tk}$. Symmetry transformations T for which $\vec{k}'$ corresponds to the same $\vec{k}$ or an equivalent wave vector form a group $G^{\vec{k}}$. This group will always contain all the pure translations $[E/\vec{t}]$ of the space group D_6^4 h. E denotes the unit element of the rotation group, $\vec{t}$ is a translation.

A set of all linearly independent functions obtained from $|n,\vec{k}\rangle$ by the symmetry transformations T of group $G^{\vec{k}}$ form a basis of the irreducible representation of $G^{\vec{k}}$. A representation is called reducible if its basis functions are not linearly independent, i.e. a set of these functions can be reduced. The irreducible representations of the symmetry group are in the form of a square matrix with a minimum possible dimension. The traces of such matrices are characters of the representation. Indices of such representations corresponding to the different energy eigenvalues $E_n(\vec{k})$ for $\vec{k}$ along the symmetry points and axes of the first Brillouin zone are shown in the Fig. II.8. There is an internationally agreed standard notation of those representations (Herring 1942). Seitz showed (Seitz 1937) that any irreducible representations can be based on a set of the above Bloch electron wavefunctions each of which represents an element $\vec{t}$ of the translation group by $\exp(-i\vec{k}\vec{t})$. For many of the pure translations in the group of the crystal lattice $\exp(-i\vec{k}\vec{t})$ is unity when $\vec{k}$ is the wavevector of a symmetry point in the Brillouin zone (Cornwell 1969). The translations which have this property form an invariant subgroup $T^{\vec{k}}$, say, of G^k. Hence, all irreducible representations of $G^{\vec{k}}$ for which the character associated with every translation in $T^{\vec{k}}$ is equal to the dimension of the irreducible representations may be obtained by considering the factor group $G^{\vec{k}}/T^{\vec{k}}$. The characters of the irreducible representations of G^k/T^k can be calculated using relations between the class multi-

plication and character multiplication (Cornwell 1969). The character tables for the irreducible representations of such factor groups $G^{\vec{k}}/T^{\vec{k}}$ corresponding to the hexagonal close packed lattice are given by Herring (1942).

These tables are extremely useful in calculating the selection rules of optical transitions. It can also be shown (Cornwell 1969) that any Bloch wave corresponding to the particular energy eigenvalue $E_n(\vec{k})$ belongs to the certain irreducible representation of the factor group $G^{\vec{k}}/T^{\vec{k}}$ i.e. if we know the solution $|n,\vec{k}\rangle$ of the Bloch equation A1 we know the irreducible representation to which the solution belongs.

Symmetry of relativistic conduction electron states

Spin orbit splitting along with other relativistic effects becomes important in heavier elements where the outer electrons are relativistic. In computing the symmetry group of the Hamiltonian corresponding to the system of such electrons a Dirac Hamiltonian should be used (Loucks 1965). It can be approximated by a Pauli Hamiltonian. The wave equation is then given by (Callaway 1964)

$$H\,\psi_{n\vec{k}}(\vec{r}) = \left[\frac{-h^2\nabla^2}{2m} + V(\vec{r}) + \frac{h^2}{4m^2c^2}\left[(\vec{\nabla}V \times \vec{p})\vec{\sigma} - \vec{\nabla}V\cdot\vec{\nabla}\right]\right]\psi_{nk}(\vec{r}) = E_n(\vec{k})\,\psi_{nk}(\vec{r}) \qquad \text{A4}$$

$\psi_{n\vec{k}}(\vec{r})$ is the Bloch wave function, n is the band index, $\vec{k}$ electron wave vector, $V(\vec{r})$ is the effective one electron potential, $\vec{\sigma}$ are $\vec{\sigma}=(\sigma_x,\sigma_y,\sigma_z)$, Pauli (2x2) matrices. $E_n(\vec{k})$ is the energy eigenvalue.
The wavefunctions $\psi_{n\vec{k}}$ of interest to us are not constant spinors, but rather may be represented by (Callaway 1964)

$$\psi_{n\vec{k}}(\vec{r}) = \sum_{\mu=1}^{2} \phi_{n\vec{k}}^{(\mu)}(\vec{r})\; V_\mu \qquad \text{A5}$$

where $\mu = 1, 2$ are spin indices, v_μ is a Pauli spinor in some coordinate system and $\phi^{(\mu)}_{nk}(\vec{r})$ is an ordinary function of position. It still has a translational symmetry of the crystal lattice. We can therefore obtain the symmetry properties of $\psi_{n\vec{k}}$ by considering the space group of the crystal similarly to that shown above for the non-relativistic case.

All considerations including factor groups are therefore identical to those above the only difference is that the symmetry properties of spin functions have to be considered. Spin function responds only to the rotational part R of a symmetry transformation T. If the rotation R is specified by Euler angles (θ, ϕ, ψ) the transformation matrix of the spinor is given by (Elliott 1954)

$$D_{\frac{1}{2}}(R) = \begin{pmatrix} \alpha & -\beta^* \\ \beta & \alpha^* \end{pmatrix} \qquad \alpha = \cos\frac{\theta}{2}\, e^{i(\phi+\psi)/2}$$

$$\beta = \sin\frac{\theta}{2}\, e^{i(\phi-\psi)/2} \qquad \text{A6}'$$

The transformation matrix of the function $\psi_{n\vec{k}}$ (Eq. A5) is given by the elements of the transformation matrix $\Gamma^{(n,\vec{k})}_{ij}$ of its spatial part $\phi^{(n)}_{nk}$ and matrix elements $\left[D_{\frac{1}{2}}(R)\right]_{\lambda,\mu}$ of the spinor part. (Callaway 1964)

$$P(T)\, \psi^{(\mu,i)}_{n\vec{k}}(\vec{r}) = \sum_{j=1}^{S} \sum_{\lambda=1}^{2} \left(\Gamma^{(n,\vec{k})}_{ij}(T) \right) \left[D_{\frac{1}{2}}(R)\right]_{\lambda,\mu} \psi^{(\lambda,j)}_{n\vec{k}}(\vec{r}) \qquad \text{A6}''$$

$i = 1, 2, \cdots, S$

S is the dimension of the representation $\Gamma^{(n,\vec{k})}$. This expression can be written in the form of direct product representation Callaway (1964)

$$P(T)\, \psi^{(\mu,i)}_{n\vec{k}} = \sum_{j,\lambda} \left[\Gamma^{(n,\vec{k})}(T) \otimes D_{\frac{1}{2}}(R) \right]^{\mu,i}_{j,\lambda} \psi^{\lambda,j}_{n\vec{k}} \qquad \text{A6}'''$$

Half angles in Eq. A6' indicate the double valuedness of the matrix $D_{\frac{1}{2}}(R)$. This corresponds to the two values of the spin for each state. The symmetry group in this case is called a double group. Consequently the symmetry group for the non-spin case is a single group.

The splitting of degeneracies by spin orbit coupling

It was shown by Eqs. A6'' and A6''' that representations of the double group can be derived from those of the single group by a direct product, i.e.

$$\Gamma^e_d = \Gamma^e \otimes D_{\frac{1}{2}}$$

However, the direct product representation may not be in general, irreducible. The criterion for a representation being reducible is (Cornwell 1969)

$$\sum_T |\chi(T)|^2 = g$$

in which the sum is over all elements of the group, g is the order of the group. If the representation $\Gamma^e \otimes D_{\frac{1}{2}}$ is reducible in the double group and Γ^e is irreducible in the single group, the characters of the representation $\Gamma^e \times D_{\frac{1}{2}}$ are the sums of the characters of some of the irreducible representations, say, μ^i. We can write symbolically

$$\Gamma^e \otimes D_{\frac{1}{2}} = \sum_i C_i^{(e)} \mu^{(i)} \qquad \text{A7}$$

Physically this means that the levels with symmetry Γ^e are split by spin-orbit interaction into levels with symmetries $\mu^{(i)}$. In the Table A1 are relations between irreducible representations of the single and double symmetry groups corresponding to the hexagonal close packed crystals. The notations of the representations are internationally agreed and their properties can be found in Herring (1942) and Elliott (1954).

Table A1 (Reprinted from Dimmock et al 1965)

Connection between the single and double group representations for the symmetry points Γ, K, H and A in the Brillouin zone for the hexagonal close-packed structure (after ELLIOTT, 1954)[a].

Γ_i	$\Gamma_1^{\pm}$	$\Gamma_2^{\pm}$	$\Gamma_3^{\pm}$	$\Gamma_4^{\pm}$	$\Gamma_5^{\pm}$	$\Gamma_6^{\pm}$
$D_{\frac{1}{2}} \times \Gamma_i$	$\Gamma_7^{\pm}$	$\Gamma_7^{\pm}$	$\Gamma_8^{\pm}$	$\Gamma_8^{\pm}$	$\Gamma_8^{\pm} + \Gamma_9^{\pm}$	$\Gamma_7^{\pm} + \Gamma_9^{\pm}$

K_i	K_1	K_2	K_3	K_4	K_5	K_6
$D_{\frac{1}{2}} \times K_i$	K_7	K_8	K_7	K_8	$K_8 + K_9$	$K_7 + K_9$

H_i	H_1	H_2	H_3
$D_{\frac{1}{2}} \times H_i$	$H_8 + H_9$	$H_4 + H_6 + H_8$	$H_5 + H_7 + H_9$

H_4, H_6 and H_5, H_7 are degenerate by time reversal.

A_i	A_1	A_2	A_3	S_1	L_1	L_2
$D_{\frac{1}{2}} \times A_i, S_i$	A_6	A_6	$A_4 + A_5 + A_6$	$S_5 + S_2 + S_3 + S_4$	L_3	L_4

A_4, A_5 are degenerate by time reversal.

P_i	P_1	P_2	P_3
$D_{\frac{1}{2}} \times P_i$	P_6	P_6	$P_4 + P_5 + P_6$

The table is used similarly to tables in Appendix B.

Above each line there are representations of a single group and under it are corresponding irreducible representations of the double group. If the levels are split by spin orbit coupling (as for instance $\Gamma_5^{\pm}$, H_2, H_3, S_1) into several levels, the symmetries of the split levels are denoted by +, e.g. $\Gamma_5^{\pm}$ is split into the levels with symmetries $\Gamma_8^{\pm}$, $\Gamma_9^{\pm}$; S_1 is split into four levels S_2, S_3, S_4, S_5, etc.

APPENDIX B

Tables of the selection rules of direct interband optical transistions in non-magnetic Rare Earth metals

Apart from the trivial selection rule such as conservation of the spin and wavevector, the selection rules are derived from character tables of the factor groups described in Appendix A.

With the help of some group theoretical considerations that are easily found in the literature (see for instance Cornwell (1969)) one obtains a simple selection rule for a direct optical transition between the states $|i\rangle$ and $|j\rangle$, i.e.

$$\langle i \left| H_{rad} \right| j \rangle \sim C_{i,j} = 1/h \sum_{T} \chi_i(T) \chi_{H_{rad}}(T) \chi_j(T) \qquad B1$$

$C^i_{i,j} = 0$ for the forbidden transitions

$\neq 0$ for the allowed dipole transitions.

The sum is over all elements T of the group of symmetry transformations of the Bloch equation (see Appendix A); h is the order of the group; $\chi_i(T)$, $\chi_j(T)$, are characters of irreducible representations $\Gamma_i(T)$, $\Gamma_j(T)$ of the group corresponding to the states $|i\rangle$, $|j\rangle$ respectively, $\chi_{H_{rad}}$ is character of the irreducible representation $\Gamma_{H_{rad}}$ corresponding to the symmetry of the electromagnetic interaction Hamiltonian H_{rad}. Close examination of equation III,1 gives that H_{rad} transforms in the same way as vector coordinates x,y,z; i.e. for the polarisation vector $\vec{\alpha}$ along the x-direction H_{rad} has transformation properties of the x-axis etc. For the hexagonal close packed lattice the vector coordinates x,y,z transform according to the irreducible representations Γ_6^-, Γ_6^-, Γ_2^- respectively. The representations of the symmetry groups corresponding to the hexagonal close packed lattice are discussed in Appendix A.

The equation B1 can also be interpreted in another way. If Γ_i, Γ_j,

$\Gamma_{H_{rad}}$ are corresponding irreducible representations to the above characters, the optical transitions $|i\rangle \longrightarrow |j\rangle$ are allowed if and only if the function $H_{rad}|i\rangle$ has the same symmetry as $|j\rangle$, i.e. if Γ_j is a direct product (Cornwell (1969)) of $\Gamma_{H_{rad}}$ and Γ_i, and we write $\Gamma_j = \Gamma_i \otimes \Gamma_{H_{rad}}$.

For characters of the direct product the following relation holds [Cornwell 1969]

$$\chi(\Gamma_i \otimes \Gamma_{H_{rad}}) = \chi(\Gamma_i) \cdot \chi(\Gamma_{H_{rad}})$$

for any element of the symmetry group. This interpretation is used in the Appendix A and the tables B1 and B2 where the selection rules are tabulated.

Table B1

Selection rules for optical dipole transitions at symmetry points of the Brillouin zone for h.c.p. non-magnetic crystal in the absence of spin orbit coupling. x,y transform as Γ_6^-, z transforms as Γ_2^- (Dimmock et al (1965))

Radiation Polarization ↓

	Γ_i	$\Gamma_1^\pm$	$\Gamma_2^\pm$	$\Gamma_3^\pm$	$\Gamma_4^\pm$	$\Gamma_5^\pm$	$\Gamma_6^\pm$
z	$\Gamma_2^- \times \Gamma_i$	$\Gamma_2^\mp$	$\Gamma_1^\mp$	$\Gamma_4^\mp$	$\Gamma_3^\mp$	$\Gamma_5^\mp$	$\Gamma_6^\mp$
x,y	$\Gamma_6^- \times \Gamma_i$	$\Gamma_6^\mp$	$\Gamma_6^\mp$	$\Gamma_5^\mp$	$\Gamma_5^\mp$	$\Gamma_3^\mp + \Gamma_4^\mp + \Gamma_6^\mp$	$\Gamma_1^\mp + \Gamma_2^\mp + \Gamma_5^\mp$
	K_i	K_1	K_2	K_3	K_4	K_5	K_6
z	$\Gamma_2^- \times K_i$	K_4	K_3	K_2	K_1	K_6	K_5
x,y	$\Gamma_6^- \times K_i$	K_5	K_6	K_5	K_6	$K_1 + K_3 + K_5$	$K_2 + K_4 + K_6$
	M_i	$M_1^\pm$	$M_2^\pm$	$M_3^\pm$	$M_4^\pm$	L_i	L_1 L_2
z	$\Gamma_2^- \times M_i$	$M_4^\mp$	$M_3^\mp$	$M_2^\mp$	$M_1^\mp$	$\Gamma_2^- \times L_i$	L_1 L_2
x,y	$\Gamma_6^- \times M_i$	$M_2^\mp + M_3^\mp$	$M_1^\mp + M_4^\mp$	$M_1^\mp + M_4^\mp$	$M_2^\mp + M_3^\mp$	$\Gamma_6^- \times L_i$	$L_1 + L_2$ $L_1 + L_2$
	A_i	A_1	A_2	A_3		H_i H_1	H_2 H_3
z	$\Gamma_2^- \times A_i$	A_1	A_2	A_3		$\Gamma_2^- \times H_i$ H_1	H_3 H_2
x,y	$\Gamma_6^- \times A_i$	A_3	A_3	$A_1 + A_2 + A_3$		$\Gamma_6^- \times H_i$ $H_2 + H_3$	$H_1 + H_3$ $H_1 + H_2$

Table B1 Continued:

Radiation Polarization ↓	S_i	Σ_1	Σ_3	T_3	T_4	R_1	R_3
z	$S_i \otimes \Gamma_2^-$	Σ_3	Σ_1	T_1	T_2	R_3	R_1
x,y	$S_i \otimes \Gamma_6^-$	$\Sigma_4 + \Sigma_1$	$\Sigma_3 + \Sigma_2$	$T_2 + T_3$	$T_1 + T_4$	$R_4 + R_1$	$R + R_2$

The Table is used as follows. Above each line are irreducible representations of the initial state.

Optical transitions between the two states $|i\rangle$ and $|j\rangle$, are allowed only if the direct product $\Gamma_{H_{rad}} \times \Gamma_i$ contains Γ_j. For polarization of radiation along x,y (i.e. in the hexagonal plane) $\hat{H}_{rad}$ transforms as x,y which corresponds to the irreducible representation Γ_6^-. For polarization along the hexagonal axis (z-axis) $\hat{H}_{rad}$ corresponds to the Γ_2^-. The above table says for instance that $\Gamma_2^- \times \Gamma_6^-$ contains Γ_6^+, in other words, if polarization is along z-axis and initial state has a symmetry Γ_6^- the only allowed optical transitions occur to the states with the symmetry Γ_6^+. $\Gamma_6^- \times \Gamma_5^-$ contains Γ_3^+, Γ_4^+ and Γ_6^+, i.e. on the other hand if the initial state $|i\rangle$ has a symmetry Γ_5^- allowed optical transitions occur to the states with symmetries Γ_3^+, Γ_4^+, Γ_6^+ etc. (for polarization along x,y).

Optical transitions in a non-magnetic h.c.p. metal with spin orbit coupling included

Since H_{rad} does not depend on spin the same holds for the relativistic case: $\hat{H}_{rad}$ for the polarization along z-axis corresponds to Γ_2^-, along x,y-axes corresponds to Γ_6^-. The selection rules for dipole transitions in the presence of the spin orbit coupling are given below as reprinted from Dimmock et al.,(1965).

Irreducible representations which occur in this table are those of the double group. The relations between the representations of the single and double group may be deduced from the equation A7 and Table A1.

TABLE B2

Selection rules for optical transitions in a non-magnetic metal at the symmetry points L, Γ, K, H, A, P, S in the presence of the spin-orbit coupling. [Dimmock et.al (1965)]

Radiation Polarization ↓

	Γ_1	Γ_7^+	Γ_8^+	Γ_9^+	L_3	L_4
z	$\Gamma_2^- \times \Gamma_1$	Γ_7^+	Γ_8^+	Γ_9^+	$L_4 + L_3$	$L_4 + L_3$
x, y	$\Gamma_6^- \times \Gamma_1$	$\Gamma_7^+ + \Gamma_9^+$	$\Gamma_8^+ + \Gamma_9^+$	$\Gamma_7^+ + \Gamma_8^+$	L_3	L_4

	K_1	K_7	K_8	K_9	P_4^+	P_5^+
z	$\Gamma_2^- \times K_1$	K_8	K_7	K_9	$P_4 + P_5 + P_6$	$P_4 + P_5 + P_6$
x, y	$K_6^- \times K_1$	$K_8 + K_9$	$K_7 + K_9$	$K_7 + K_8$	P_4	P_5

	H_1	H_4	H_5	H_6	H_7	H_8	H_9
z	$\Gamma_2^- \times H_1$	H_7	H_6	H_5	H_4	H_9	H_8
x, y	$\Gamma_6^- \times H_1$	H_9	H_8	H_9	H_6	$H_5 + H_7 + H_8$	$H_4 + H_6 + H_9$

	A_1	A_4	A_5	A_6	S_1	S_2	S_3	S_4	S_5
z	$\Gamma_2^- \times A_1$	A_5	A_4	A_6		$S_3 + S_4 + S_5$	$S_2 + S_4 + S_5$	$S_2 + S_3 + S_5$	$S_2 + S_3 + S_4$
x, y	$\Gamma_6^- \times A_1$	A_6	A_6	$A_4 + A_5 + A_6$		S_2	S_3	S_4	S_5

The Table is used in a similar way as Table B1.

APPENDIX C

Computer programme for the calculation of optical constants optical conductivity and dilectric constant.

```
ORTRAN IV G COMPILER        MAIN            07-12-72        14:20.40        PAGE 0001

0001          INTEGER CH,N(20)
0002          REAL E1(500),E2(500),SIGMA(500),R(500),C(500),C1(100)
0003         DATA C1/2.9755,2.91,2.84,2.79,2.74,2.69,2.645,2.6,2.555,2.525,
            12.5,2.47,2.445,2.42,2.395,2.365,2.33,2.3 ,2.26,2.23,2.2,2.17,2.13,
            22.09,2.06,2.02,1.98,1.94,1.9 ,1.85,1.8,1.75,1.7,1.65,1.6,1.545,
            31.495,1.44,1.38,1.33,1.28,1.23,1.18,1.13,1.08,1.04,0.995,0.953,
            4 .9 5, .86,0.81, .77, .73, .69, .66, .63, .61, .59, .565, .55,
            5 .53, .513,0.5, .49, .48, .478, .472/
0004          2 FORMAT(1H ,I4,5X,F7.3,5X,E10.4,5X,E10.4,5X,E10.4,5X,E10.4,5X,
             1E10.4,2X,F5.1,2X,E9.3,2X,E9.3)
0005          3 FORMAT(1H ,'CH',T11,'EV',T21,'EPSLN1',T36,'EPSLN2',T51,'SIGMA',
             1T68,'R',T81,'RO',T96,'DELTA'/)
0006           WRITE(6,3)
0007        120  FORMAT(F5.1)
0008           READ(5,120)XXNO
0009           N(1)=1
0010           READ(5,12)THETA,N(2),N(3),N(4),N(5)
0011           THETA=THETA* 3.14159/180.
0012         12 FORMAT(F5.1,4I3)
0013           K=N(2)+N(3)+N(4)+N(5)
0014           DO 10 I=1,K
0015           READ(5,1)CH,A,B,D,LA,LB
0016         1 FORMAT(I4,3F5.1,2I4)
0017           ALA=LA
0018           ALB=LB
0019           AA= ALA/1000.+1.
0020           AB= ALB/1000 +1.
0021           A=A*AA
0022           B=B*AB
0023           L= CH/5+16
0024           C(I)= C1(L)
0025           RO=SQRT(ABS(A/B))
0026           Y=(A+B-2.*D)/(2.*SQRT(A*B))
0027           SXNO=SQRT(XXNO)
0028           IF (Y)5,4,6
0029         4 ELTA=3.14159/2.
0030           DELTA=90.
0031           GO TO 7
0032         5 ELTA=ATAN(SQRT(ABS(1.-Y**2)/(Y**2)))
0033           DELTA= 180.- ELTA*180./3.14159
0034           GO TO 7
0035         6 ELTA=ATAN(SQRT(ABS(1.-Y**2)/(Y**2)))
0036           DELTA= ELTA*180./3.14159
0037         7 CONTINUE
0038           IF(RO-1.0)77,8,8
0039         8 E2(I)=0.
0040           E1(I)=  (TAN(THETA))**2 - 2.*(SIN(THETA))**4/COS(THETA)**2/(1.+Y)
0041            XNO =E1(I)**(-.5)
0042            E1(I)=XNO
0043             GO TO 80
0044        77  P = (1.0+RO**2+2.0*RO*Y)/(1.0+RO**2-2.0*RO*Y)
0045           X = 2.0*RO*SIN(ELTA)/(1.0-RO**2)
0046           EPSLN1=P*(1.0-X**2)/(1.0+X**2)*XXNO
0047            EPSLN2=P*2.0*X/(1.0+X**2)*XXNO
0048            E1(I)=EPSLN1*(SIN(THETA))**4/(COS(THETA))**2-SIN(THETA)**2
```

```
FORTRAN IV G COMPILER        MAIN            07-12-72        14:20.40        PAGE 0002

                E2(I)=EPSLN2*(SIN(THETA)**4)/COS(THETA)**2
              8  CONTINUE
                 ALMB=1.239/C(I)
                 SIGMA(I)= E2(I)/(2.*ALMB)
                 Z= SQRT(E1(I)**2+E2(I)**2)
                 ZN=SQRT(ABS(E1(I)+Z)/2.)
                 R(I)=(Z+SXNO-2.*ZN)/(Z+SXNO+2.*ZN)
                 WRITE(6,2)CH,C(I),E1(I),E2(I),SIGMA(I),R(I),RO,DELTA,P,X
              1  CONTINUE
                 E1MIN=E1(1)
                 E1MAX=E1(1)
                 E2MIN=E2(1)
                 E2MAX=E2(1)
                 SMIN=SIGMA(1)
                 SMAX=SIGMA(1)
                  DO 9 I=2,K
                 IF(E1MIN-E1(I))101,101,102
             102 E1MIN=E1(I)
             101 IF(E1MAX-E1(I))103,104,104
             103 E1MAX=E1(I)
             104 IF(E2MIN-E2(I))106,105,106
             106 E2MIN=E2(I)
             105 IF(E2MAX-E2(I))107,108,108
             107 E2MAX=E2(I)
             108 IF(SMIN-SIGMA(I))110,110,109
             109 SMIN= SIGMA(I)
             110 IF(SMAX-SIGMA(I))111,9,9
             111 SMAX=SIGMA(I)
               9 CONTINUE
                 IF(ABS(E1MAX)-ABS(E1MIN))91,92,92
              91 E1SP= ABS(E1MIN)
                 GO TO 93
              92 E1SP= ABS(E1MAX)
              93 CONTINUE
                 NN=E1SP/20.
                 NN=NN+1
                 E1SP=NN*20
                 FCTE1= E1SP/2.
                 FCTE2= E2MAX/4.
                 FCTS = SMAX/4.
                 FCE2= 10./FCTE2
                 FCE1= 20./FCTE1
                  FCS=5./FCTS
              11 FORMAT(1H ,E9.4,10X,E10.4,10X,E10.4)
              94 WRITE (6,11) E1SP,E2MAX,SMAX
                 CALL PAXIS(1.0,.5,'E1',2,4.,90.,-E1SP,FCTE1,FCE1)
                 CALL PAXIS(1.0,.5,'SIGMA',5,4.,90.,0.,FCTS,FCS)
                 CALL  PAXIS(1.0,.5,'PHOTON ENERGY',-13,12.,0.0,0.0,0.25,2.)
                  J=1
                  CALL PLTOFS(0.0,.25,0.0,FCTE1,1.,2.5)
                  CALL PLINE(C(N(J)),E1(N(J)),N(J+1),1,-1,J,99.9)
                  CALL PLTOFS(0.0,.25,0.0,FCTS,1.,5.)
                  CALL PLINE(C(N(J)), SIGMA(N(J)),N(J+1),1,-1,J,99.9)
                 N(J+1)=N(J+1)+N(J)
                 J=J+1
```

```
FORTRAN IV G COMPILER        MAIN            07-12-72        14:20.49        PAGE 0003
0104                  CALL PLTOFS(0.0,0.25,0.0,FCTE1,1.,2.5)
0105                  CALL PLINE(C(N(J)),E1(N(J)),N(J+1),1,-1,J,99.9)
0106                  CALL PLTOFS(0.0,0.25,0.0,FCTS,1.,5.)
0107                  CALL PLINE(C(N(J)), SIGMA(N(J)),N(J+1),1,-1,J,99.9)
0108                  N(J+1)=N(J+1)+N(J)
0109                  J=J+1
0110                  CALL PLTOFS(0.0,0.25,0.0,FCTE1,1.,2.5)
0111                  CALL PLINE(C(N(J)),E1(N(J)),N(J+1),1,-1,J,99.9)
0112                  CALL PLTOFS(0.0,0.25,0.0,FCTS,1.,5.)
0113                  CALL PLINE(C(N(J)), SIGMA(N(J)),N(J+1),1,-1,J,99.9)
0114                  N(J+1)=N(J+1)+N(J)
0115                  J=J+1
0116                  CALL PLTOFS(0.0,0.25,0.0,FCTE1,1.,2.5)
0117                  CALL PLINE(C(N(J)),E1(N(J)),N(J+1),1,-1,J,99.9)
0118                  CALL PLTOFS(0.0,0.25,0.0,FCTS,1.,5.)
0119                  CALL PLINE(C(N(J)), SIGMA(N(J)),N(J+1),1,-1,J,99.9)
0120                   CALL PLTEND
0121                  STOP
0122                  END

  TOTAL MEMORY REQUIREMENTS 003988 BYTES
EXECUTION TERMINATED
```

Appendix D

Macroscopic definition of optical constants

The behaviour of the electromagnetic wave (at optical frequencies) is determined by Maxwell's equations. If $\bar{B}$, $\bar{H}$, $\bar{D}$, $\bar{E}$ are magnetic induction, magnetic field, electric induction and electric field respectively than

$$\begin{aligned} \mathrm{div}\vec{D} &= 0 \\ \mathrm{div}\vec{B} &= 0 \\ \mathrm{curl}\vec{E} &= -1/c \ (\partial \vec{B}/\partial t) \\ \mathrm{Curl}\vec{H} &= 1/c \ (\partial \vec{D}/\partial t) \qquad \text{if } \rho = J = 0 \end{aligned} \tag{D1}$$

For the optical frequencies the magnetic permeability is equal to unity and the behaviour of an electromagnetic wave in the absorbing substance in question is fully determined by its electrical component. The relation between $\bar{D}$ and $\bar{E}$ in its general form is given by [Landau & Lifshitz (1960)]

$$D_j(\bar{x},t) = E_j(\bar{x},t) + \sum_{i=1} \int_0^\infty f_{ij}(\tau)\ E_i(x,t-\tau)\ d\tau \tag{D2}$$

where i,j represent component indexes of the rectangular coordinate system. For an electromagnetic wave of a single frequency

$$\vec{E}(x,\omega,t) = \vec{E}_o \exp(i(\omega t - \vec{k}_{rad}\vec{r}) \tag{D2a}$$

where $\vec{k}_{rad}$ is the propagation wavevector, in general, complex. The above material characteristic is given by [Landau & Lifsitz (1960)]

$$D_j(\vec{x},t) = \sum_{i=1}^{3} \varepsilon_{i,j}(\omega)\ E_i(\omega,\vec{x},t) \tag{D3}$$

where $\varepsilon_{i,j}(\omega) = 1 + \int_0^\infty f_{i,j}(\tau) e^{i\omega\tau} d\tau$ is a tensor of the complex dielectric constant. Very often this tensor is related to the tensor

of the complex conductivity $\sigma_{kj}(\omega) = \sigma^{(1)}_{kj}(\omega) + i\sigma^{(2)}_{kj}(\omega)$

which is given by the relation between the $\vec{E}(\vec{x},\omega,t)$ and the current density

$$\vec{j}_i(\vec{x},t) = \sum_{j=1}^{3} \sigma_{j,i}(\omega)\ E_j(\vec{x},\omega,t) \qquad D4$$

and

$$\varepsilon_{j,k}(\omega) = 4\pi i/\omega\ \sigma_{j,k}(\omega) \qquad D5$$

The dielectric constant tensor is in general a complex number. The relation between the real and imaginary part is given by a Krammers-Krönig relation (Landau & Lifshitz 1960) i.e. if

$$\varepsilon_{jk}(\omega) = \varepsilon^{(1)}_{jk}(\omega) + i\varepsilon^{(2)}_{jk}(\omega) \qquad D6$$

then $$\varepsilon^{(1)}_{jk}(\omega) = 1 + \frac{2}{\pi}\int_0^\infty \frac{\omega'\,\varepsilon^{(2)}_{jk}(\omega')}{(\omega')^2 - \omega^2} \qquad D7$$

$$\varepsilon^{(2)}_{jk}(\omega) = \frac{2}{\pi}\int_0^\infty \frac{\varepsilon^{(1)}_{jk}(\omega')}{(\omega')^2 - \omega^2}\,d\omega' \qquad D8$$

The energy dissipation of an electromagnetic field of a single optical frequency per unit time is given by (Landau & Lifshitz 1960)

$$Q = \omega/8\pi \sum_{j,k} \varepsilon^{(2)}_{jk}(\omega)\,(E^o_j)^*\,E^o_k = \sum_{j,k} \tfrac{1}{2}\sigma^{(1)}_{jk}(\omega)\,(E^o_j)^*\,E^o_k \qquad D9$$

where E^o_k, E^o_j are components of amplitude of the single frequency electromagnetic wave and $\sigma^{(1)}_{j,k}(\omega)$ is the real part of the optical conductivity. In the following we mainly deal with polycrystalline films.

$(E_j)^*$ is a complex conjugate of E_j $\quad j,k = 1,2,3$

When discussing experimental technique and results in the

chapters IV, V and VI. we refer to the isotropic average of the complex dielectric constant.

The usual notation used in these chapters is given below:

The imaginary and real parts of the average dielectric constant $\mathcal{E}$ are referred as $\mathcal{E}_2, \mathcal{E}_1$ respectively i.e.

$$\mathcal{E}(\omega) = \mathcal{E}_1 + i\mathcal{E}_2 = n^2 - k^2 + i2nk \qquad \text{D10}$$

where n and k are averages of the optical constants in the usual notation. The results in chapter V are presented in the form of the spectral variations of the real part of the dielectric constant $\mathcal{E}_1(\omega)$ and real part of the average optical conductivity $\sigma(\omega)$

$$\frac{\sigma(\omega)}{} = \frac{\omega \cdot \mathcal{E}_2(\omega)}{4\pi} = \frac{n \cdot k}{2\pi} \cdot \omega \qquad \text{D11}$$

Reflection and Refraction of Electromagnetic Waves from metallic polycrystalline films

In the present work the optical constants of Rare Earth metals were determined by a polarimetric reflection method. This method consists of the study of elliptically polarized radiation reflected from the metallic film surface. The situation is shown in the Fig D.1. The coordinate system is chosen so that axes z and y lie in the plane of refelection. The angle of incidence is φ. Electrical components of the incident electromagnetic wave perpendicular and parallel to the plane of incidence are $E_s^{(o)}$ and $E_p^{(o)}$ respectively. Corresponding

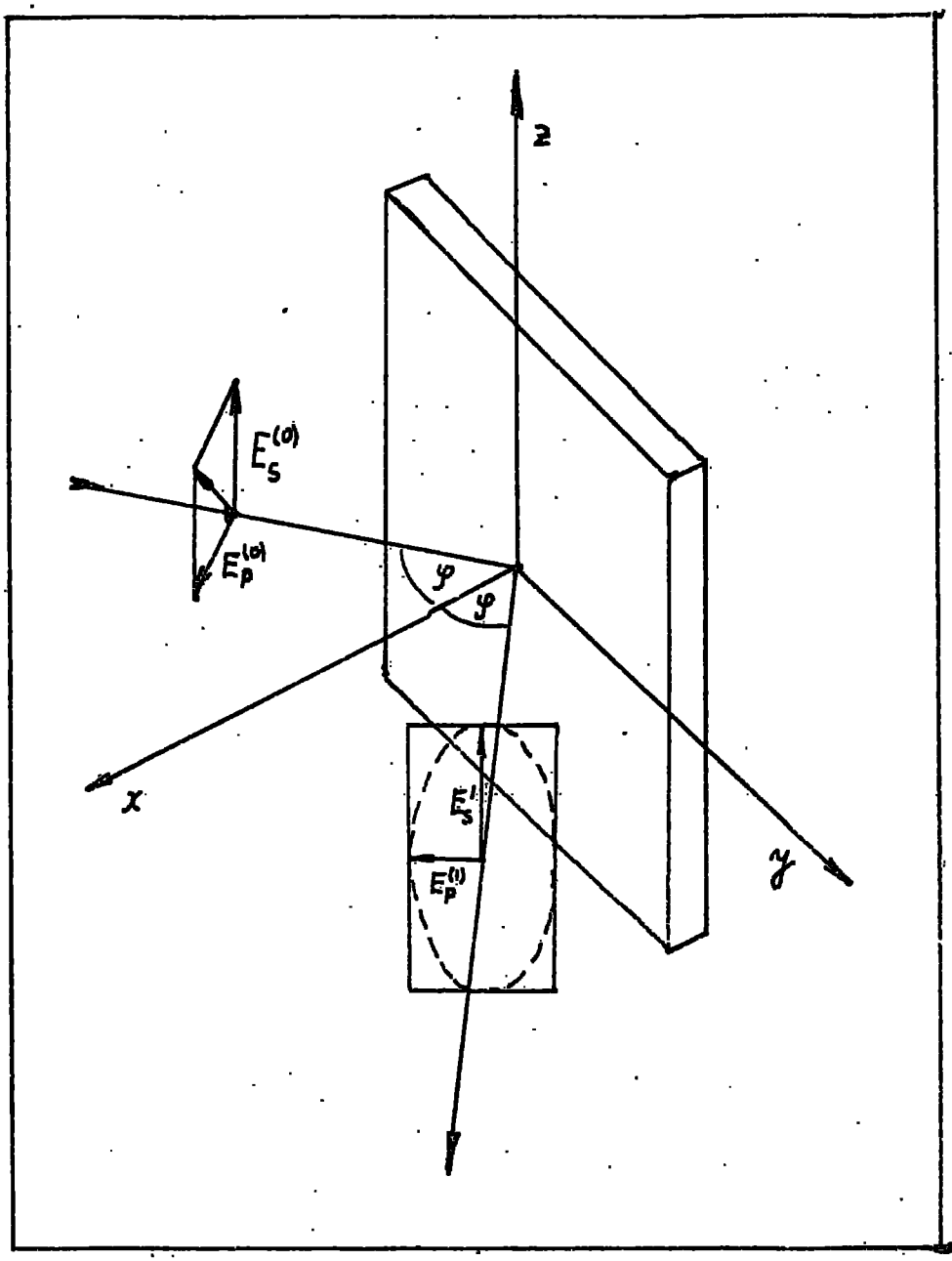

Fig.D.1

components of the reflected wave are $E_s^{(1)}$, $E_p^{(1)}$. The relations between the amplitudes of the reflected and the incident waves are given by Fresnel's formulae (since the films used in the present work are highly polycrystalline, we do not consider anisotropy of the optical constants) [Landau & Lifshitz (1960)].

$$R_s = \frac{E_s^{(1)}}{E_s^{(o)}} = \frac{\sqrt{\varepsilon_o}\cos\varphi - \sqrt{\varepsilon - \varepsilon_o \sin^2\varphi}}{\sqrt{\varepsilon_o}\cos\varphi + \sqrt{\varepsilon - \varepsilon_o \sin^2\varphi}} \qquad \text{D12}$$

$$R_p = \frac{E_p^{(1)}}{E_p^{(o)}} = \frac{\varepsilon\cos\varphi - \sqrt{\varepsilon_o}\sqrt{\varepsilon - \varepsilon_o \sin^2\varphi}}{\varepsilon\cos\varphi + \sqrt{\varepsilon_o}\sqrt{\varepsilon - \varepsilon_o \sin^2\varphi}}$$

ε is the complex dielectric constant of the metallic material under investigation. ε_o is the dielectric constant of the surrounding medium. R_s, R_p are generally complex numbers. Their ratio can be given in the form

$$\frac{R_s}{R_p} = \varrho\, e^{i\Delta} \qquad \text{D13}$$

$\frac{R_s}{R_p}$ is also a complex number. The phase Δ and the absolute value ϱ are in general dependent on the frequency of the radiation. If the incident radiation is plane polarised the radiation reflected from the surface is generally elliptically polarised and parameters of that ellipse given by ϱ and Δ are determined by the dielectric constants ε, ε_o and the angle of incidence φ . The determination of the complex dielectric constants from measured ϱ and Δ and known ε_o and φ is the principle of the polarimetric method described in

chapter IV.

The reflection coefficient R is defined as the time average ratio of the energy flux reflected from the surface to the incident flux. For normal incidence R is given by (Landau & Lifshitz 1960)

$$R = \frac{\left| \sqrt{\varepsilon_o} - \sqrt{\varepsilon} \right|^2}{\left| \sqrt{\varepsilon_o} + \sqrt{\varepsilon} \right|^2} \qquad \text{D14}$$

$\varepsilon, \varepsilon_o$ are the above defined dielectric constants.

APPENDIX E

Computer programme for the Kramers-Kronig integral.

```
#$1 krkr
>      1            DIMENSION SIGMA(200)
>      2            DIMENSION DIELEC(200)
>      3            READ(7,4)SIGMA0,TAV,JI,JN,JR,JS
>      4          4 FORMAT(2E10.4,4I3)
>      5            DO 11 J=1,200
>      6            SJ=J
>    6.1            SJ=SJ/10.-8.9954
>      7            SIGMA(J)=SIGMA0/(EXP(2.*SJ)*TAV**2+1.)
>    7.1            EV=EXP(SJ)
>    7.2            IF(EV-0.2)11,12,12
>    7.3         12 IF(EV-0.8)13,13,11
>    7.4         13 WRITE(6,14)EV,SIGMA(J)
>    7.5         14 FORMAT(1H ,F5.2,1X,E10.4)
>      8         11 DIELEC(J)=1.
>      9            DO 100 JM=9,JS
>     10            JA=JM*10-10+1
>     11            JB=JA+9
>     12            READ(5,3) (SIGMA(J),J=JA,JB)
>     13          3 FORMAT(10F6.2)
>     14          5 FORMAT(10F8.2)
>     15        100 CONTINUE
>     16          2 FORMAT(4I5//)
>     17              READ(5,6)II,IS
>     18          6 FORMAT(2I2)
>     19            DO 103 JP=II,IS
>     20            IA=JP*10-9
>     21            IB=IA+9
>     22            READ(5,3) (DIELEC(JDE),JDE=IA,IB)
>     23        103 CONTINUE
>     24          8 FORMAT(2I4/)
>     25            DO 101 JO=JI, JN
>     26            SUM=0.
>     27            DO 102 J=1,JR
>     32         10 S=J
>     33            S=S/10.
>     34            EXPES=(EXP(S)-EXP(-S))/2.
>     35            SUM=SUM+(SIGMA(JO+J)-SIGMA(JO-J))/EXPES
>     36        102 SO=JO
>     37            SO=SO/10.
>     38            SUM=((SUM*2000.)/(3.1416*EXP(SO)))+1.
>     39            EV=EXP(SO-8.9954)
>     40            DIFFER=DIELEC(JO)+SUM
>     41            PERCNT=DIFFER*100./DIELEC(JO)
>     42            WRITE(6,7)SO,DIFFER,SUM,PERCNT,DIELEC(JO),SIGMA(JO)
>     43          7 FORMAT(7F7.2)
>     44        101 CONTINUE
>     45            STOP
>     46             END
```